Diamond Based Nanostructures For Electronic Applications

Niall James Tumilty

This thesis is submitted for the degree of Doctor of Philosophy

Department of Electronic and Electrical Engineering

University College London

University of London

2010

Declaration

The work in this thesis is the result of research carried out at University College London, London Centre for Nanotechnology, Diamond Electronics Group. I declare it to be my own work unless referenced to the contrary in the text.

Acknowledgement

I would like to express my deepest gratitude to my research supervisor, Prof Richard B. Jackman for giving me the opportunity to study for a PhD. His enthusiasm, support and encouragement throughout this endeavour have been invaluable. I would also like to thank the UCL diamond group, in no particular order, Dr Haitao Ye, Dr Stephane Curat, Mose Bevilaqua, Aysha Chaudhary, Rezal Ahmad, Robert Edington and Joseph Welch are all appreciated for the many academic and non academic discussions we have held during this PhD. I would also like to thank Dr Steve Firth from Chemistry for access to the Raman facility and Kevin Lee for help with the SEM.

Gratitude to EPSRC and Rolls-Royce for providing me with a PhD studentship, the UCL Graduate School are also thanked for providing me with numerous travel awards allowing me to attend international conferences overseas.

I would also like thank my many flatmates since I've been in London, that been there to listen to my woes after many a failed experiment and for the many great times we have shared, mostly around Camden town. A big thanks to Chihyin for keeping my spirits up by just being herself....

And back home, special gratitude is due to my family, and others for their consistent and endless encouragement and support throughout this PhD.

<div align="right">

Niall James Tumilty
April 2010
London

</div>

If a man will begin with certainties, he shall end in doubts, but if he will content to begin with doubts, he shall end in certainties.

— Francis Bacon

Abstract

Research in the area of CVD diamond thin films has increased significantly during the last decades to the point where single crystal diamond is now commercially available. The remarkable properties of diamond including its extreme hardness, low coefficient of friction, chemical inertness, high thermal conductivity, transparency and semiconducting properties make it attractive for a number of applications, among which electronic devices is one of the key areas. A detailed knowledge of electrical properties of diamond films is therefore critical.

This thesis describes (1) a Hall effect study of highly boron-doped (111) diamond films (2) a Hall effect and impedance spectroscopic study of boron δ-doped diamond structures and (3) the synthesis of carbon nanotubes on single crystal diamond.

Systematic investigations have been carried out on single crystal, boron-doped (111) diamond films. The influence of ultra pure gases, doping concentration and temperature on carrier transport are discussed in detail.

A comprehensive study on boron δ-doped diamond films is also performed; Hall effect and impedance spectroscopy are used to evaluate these films, providing valuable insight into the complex carrier transport mechanisms occurring in these structures. The influence of temperature on carrier mobility and the free carrier density are discussed. This is allied with valuable information gained from impedance spectroscopy, where the presence of multiple semicircular responses (conduction pathways), modelled using a RC parallel circuit, yields data which leads to a greater understanding on the influence of the interface between the boron δ-doped layer and the surrounding intrinsic diamond layers. These semicircular responses are thus attributed to different crystalline regions in these structures, namely the boron δ-doped layer and the interfacial regions

surrounding δ-layer. The influence of this interface region on the structures overall conductivity is discussed.

Finally the synthesis of carbon nanotubes (CNTs) on single crystal diamond is reported for the first time. Scanning electron microscopy combined with Raman spectroscopy is used to understand the influence of temperature and differing growth gas mixtures on the yield and crystallinity of these as-grown CNTs.

Table of Contents

Chapter 1

Introduction

Diamond has been admired as a gemstone for centuries for its natural beauty, however, over for the last 50 years diamond has been the subject of much study by scientists worldwide due to there superlative properties. Many scientists have since shown the potential diamond holds due to its combination of physical and chemical properties, making it far superior to other semiconductor materials.

First attempts at synthesising diamond date as far back as the late 19th century and did not come without great difficulty. However it was not until the development of high-pressure high-temperature synthesis in the 1950's whereby the procedure, a direct imitation of that which occurs deep in the earth's crust, resulted in the production of small diamonds. These diamonds are heavily contaminated making them unsuitable for electronic applications. Diamond as a semiconductor material has made much more progress since the advent of Chemical Vapour Deposition (CVD) in the 1960's [1-3]. During the last 40 years much progress has been achieved in diamond growth by CVD methods, leading to the production of electronic grade material. Single crystal diamond is now commercially available with the single crystal substrate size increasing gradually year-on-year; maximum current size is 8mm x 8mm (element 6). CVD diamond can now be routinely doped with boron making it p-type with an ionisation energy of 0.37eV above the valence band edge. The development of n-type diamond has been a much sterner challenge with only one successful report of n-type, phosphorous-doped diamond (111) films in the literature to date [4]. The ionisation energy of phosphorous-doped diamond is reported to be 0.6eV from the conduction band edge making it unlikely for diamond bipolar electronic devices using phosphorous to be utilised below 400°C. For diamond to be truly considered as an electronic material an effective n-type dopant must be found.

Chapter 2 reviews the field of diamond technology, reporting on structure, growth, properties and applications. An account of the chemical vapour deposition methods for growing diamond is also presented in this chapter. Substrate materials, surface pre-treatments, nucleation enhancement, and deposition conditions are also reviewed. Chapter 3 introduces basic concepts and equations relating to carrier transport mechanisms in semiconducting materials. Chapter 4 reviews the experimental methods and techniques used in this thesis.

In chapter 5, due to the development of phosphorous-doped diamond (111) films [4], a series of boron-doped diamond (111) films have been grown and characterised using Hall effect analysis and scanning tunnelling microscopy for the first time. Here it is shown that ultra pure process gases and refined growth parameters used for the synthesis of diamond can yield high quality diamond films with extremely low compensation ratios. This has resulted in valence band conduction at very high carrier densities relative to boron-doped diamond (100) films, where at similar carrier density levels the onset of hopping conductivity would be apparent. The significance of this result is discussed therein.

In chapters 6 and 7, impedance spectroscopic and Hall effect studies are presented of boron δ-doped diamond films, respectively. The development of diamond based high frequency transistors has been hindered by the deep acceptor (boron) level in diamond. One method in which this problem can be circumnavigated is by growing very thin (less than the de Broglie wavelength) heavily boron-doped diamond layers (<5nm), as the activation energy of boron-doped diamond is concentration dependent [5]. In this way the carriers resulting from the acceptors in the heavily doped region experience a spatial separation from their parent atoms when excited into the valence band (intrinsic region), this reduces carrier scattering and higher mobilities are observed. This approach is well established within the III-V semiconductor industry [6]. In this chapter the difficulties in growing such

layers are discussed alongside the measured electrical characteristics of these structures.

In Chapter 8, the deposition of carbon nanotubes on diamond substrate is explicitly studied for the first time. Scanning electron microscopy and Raman spectroscopy are applied to characterize the influence of temperature and differing gas ratios on the yield and crystallinity of this system.

Chapter 9 summaries this thesis and present conclusions based on the work achieved at UCL, and also points to future work. The impact of these results on the potential use of these materials for electronic device applications is discussed.

References

1.   W. G. Eversole, U.S. Patent 3,030,188, April 17, 1962.

2.   J. C. Angus *et al. J. Appl. Phys.* 39: 2915 (1968).

3.   B.V. Deryagin and D. V. Fedoseev, *Rus. Chem. Rev. 39* 39: 783 (1970).

4.   S. Koizumi, M. Kamo, Y. Sato, H. Ozaki, and T. Inuzuka, Appl. Phys. Lett. 71, 1065 (1997).

5.   TH Borst and O Weis, Phys. Stat. Sol., (a) 154 423 (1996).

6.   "Delta-doping of Semiconductors" E.F. Schubert (Ed.), (Cambridge University Press, 1996).

Chapter 2: Carbon and the structure and synthesis of diamond

2.1   Introduction to carbon

Carbon is the 4th most abundant element in the universe by mass, after hydrogen, helium and oxygen. Its symbol is C and its atomic number 6. It is a non-metallic, tetravalent element that takes several allotropes, illustrated in figure 2.1. The physical properties of carbon are known to vary widely with each allotropic form.
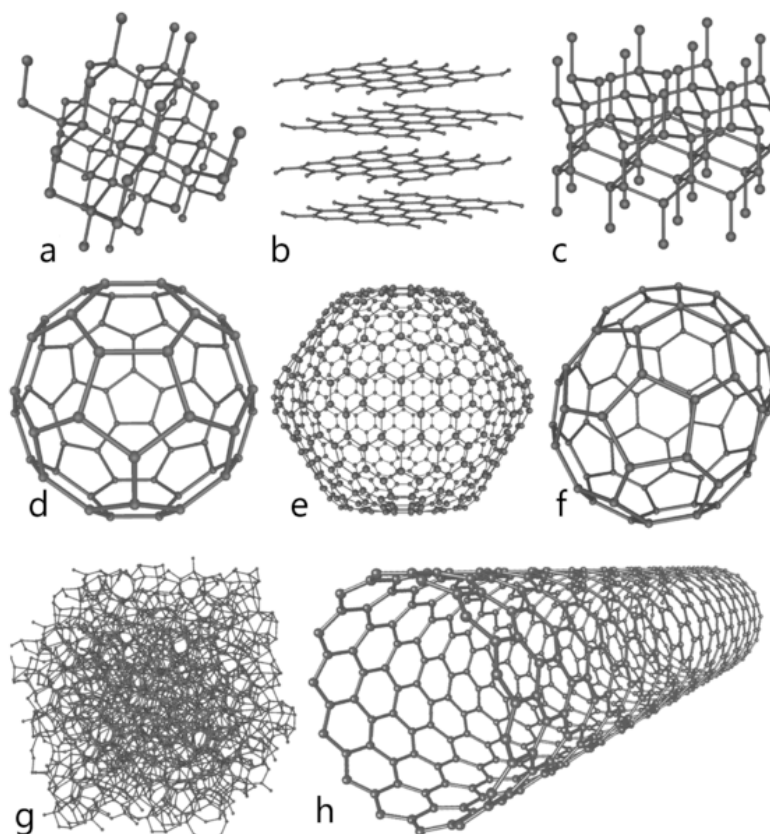
Figure 2.1: Some allotropes of carbon: (a) diamond, (b) graphite, (c) lonsdaleite, (d,e,f) buckyballs (C_{60}, C_{540}, C_{70}), (g) amorphous carbon and (h) a carbon nanotube (from [1]).

2.1.1 Basic concepts
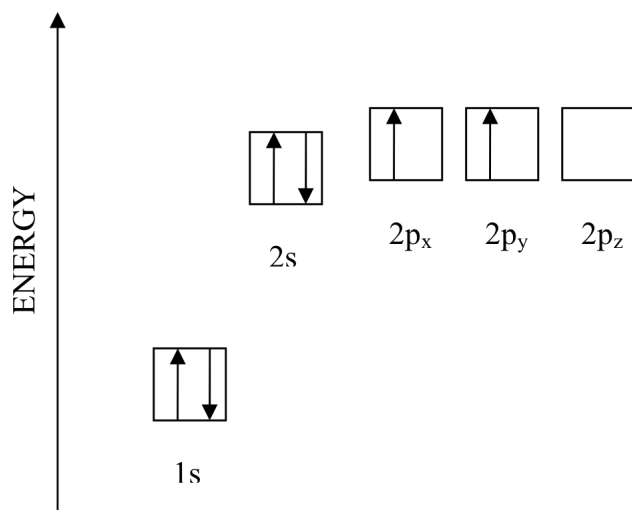
Figure 2.2: Energy levels of carbon in its ground state

The energy level graph shows six electrons represented by arrows (the direction of the arrow represents the electron spin). Two electrons are found in the 1s orbital close to the nucleus. The next two will go into the 2s orbital. The remaining ones will be in two separate 2p orbitals. This is because the p orbitals have the same energy and the electrons would rather be in separate orbitals. However, in bonded carbon, such as diamond and graphite, the electronic configuration is modified. As a result sp^n hybridisation of orbitals occur with n= 1,2,3 [2]. The three possible hybridizations of orbitals occurring in carbon are: sp^3 (tetragonal), sp^2 (trigonal) and sp (digonal), this is due to mixing of electronic wave functions of the 2s and 2p orbitals.

2.1.1.1   sp^3 hybridization

Once the carbon atom is in its excited state (C*) with four unpaired electrons, the four atomic orbitals (A.O.s) can be mixed together to form four equivalent

hybrid orbitals (H.O.s). This process is called hybridization.

C^*: $1s^2$, $2s^1$, $2p_x^1$, $2p_y^1$, $2p_z^1$
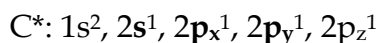
The A.O.s written in bold are those used in the hybridization process.

As the mixing in diamond involves one 2s and three 2p-orbitals, it is referred to as being sp³ hybridized. As there are four atomic orbitals used in the hybridization process, four energetically equivalent sp³ hybrid orbitals are formed. These sp³ hybrid orbitals adopt tetrahedral geometry:

2s   2p sp^3 tetrahedral orientation of sp^3 hybrid orbitals
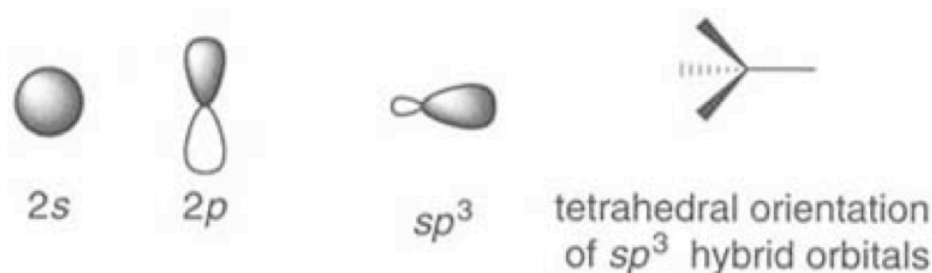
Figure 2.3.1: Hybridization of carbon - four *sp³* orbitals (from [3]).

Diamond is a *sp³* bonded form of carbon where each carbon atom shares it four *sp³* valence electrons with one *sp³* valence electron of any four other carbon atoms in a tetrahedral geometry. The energy required to accomplish the sp³ hybridization and raise the carbon atom from the ground state to the corresponding valence state V, is 230 kJ mol^{-1} [2]. Diamond has two different atomic geometries, one with a cubic symmetry (the more common and stable) and one with a hexagonal symmetry found in nature as the mineral lonsdaleite. The crystal structure of cubic diamond (figure 2.3.2) is equivalent to a face-centered cubic (FCC) lattice, with additional carbon atoms located at a_0(1/4, 1/4, 1/4), a_0(3/4, 3/4, 1/4), a_0(1/4, 3/4, 3/4) and a_0(3/4, 1/4, 3/4), where a_0 is the lattice constant, illustrated in figure 2.3.2. Diamond has the highest atomic density of all known materials, which explains why diamond is

the stiffest, hardest and least compressible of all substances [2].

The diamond unit cell is cubic (figure 2.3.2), with a side length a_0 approximately equal to 3.567 Å at room temperature.

The C–C bond length d is equal to 1/4 of the cubic body diagonal, so that $d = (\sqrt{3})a_0/4 \approx 1.54$ Å [2] which energy is 711KJ/mol [2]. The conventional cell contains the equivalent of 8 whole C atoms. The atomic density is therefore $8/(a_0^3) \approx 8/((3.567 \times 10^{10}$ m$)^3) \approx 1.76 \times 10^{29}$ atoms/m^3 (1.76×10^{23} atoms/cm^3).
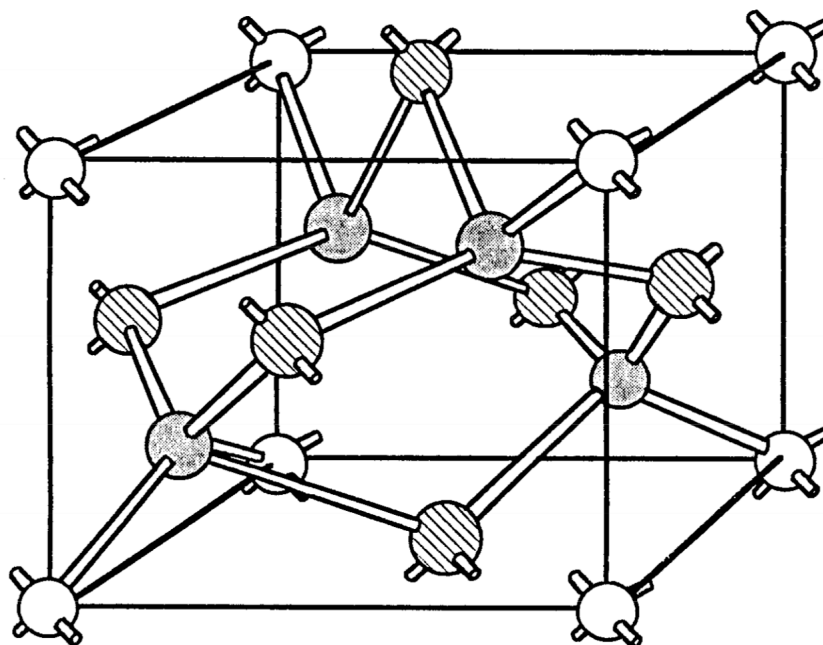
Figure 2.3.2: Face-centered cubic structure of the diamond crystal (from [5]).

2.1.1.2   sp^2 hybridization

Graphite and the recently discovered carbon nanotubes [5] are sp^2 bonded carbon structures. Graphite is a layered compound. In each layer, the carbon atoms are arranged in a hexagonal lattice with separation of 0.142 nm [5], and the distance between planes is 0.335 nm [6].

trigonal orientation
of *sp²* hybrid orbitals

Figure 2.3.3: Hybridization of carbon - three *sp²* orbitals (from [3]).

The sp² hybrid orbitals are formed in similar manner to the sp³ orbitals. The only difference is that the four electrons in the 2s and 2p orbitals rearrange into two distinct energy levels. Three of these four electrons occupy three sp² orbitals whilst the remaining one stays in its original 2p configuration. The sp² hybrid orbitals are identical and are coplanar forming a 120º angle between them, as illustrated in figure 2.3.3. The remaining 2p orbital is pointing perpendicular to the plane formed by the sp² orbitals. The 2p orbitals, perpendicular to the σ bonding plane overlap to form a pi (π) bond between the parallel sp² –hybridised carbon planes. The electrons in the π bond region are delocalized and are only held together by Van der Waals forces. These forces can be easily overcome to allow the planes to slide over each other, explaining the low shear modulus of graphite. Further, the fact that the electrons are delocalized also allows them to move under an electric field, explaining the low resistivity of graphite (in-plane). Graphite does not conduct electricity out-of-plane.

6.71 Å

6.71 Å

● Carbon atom
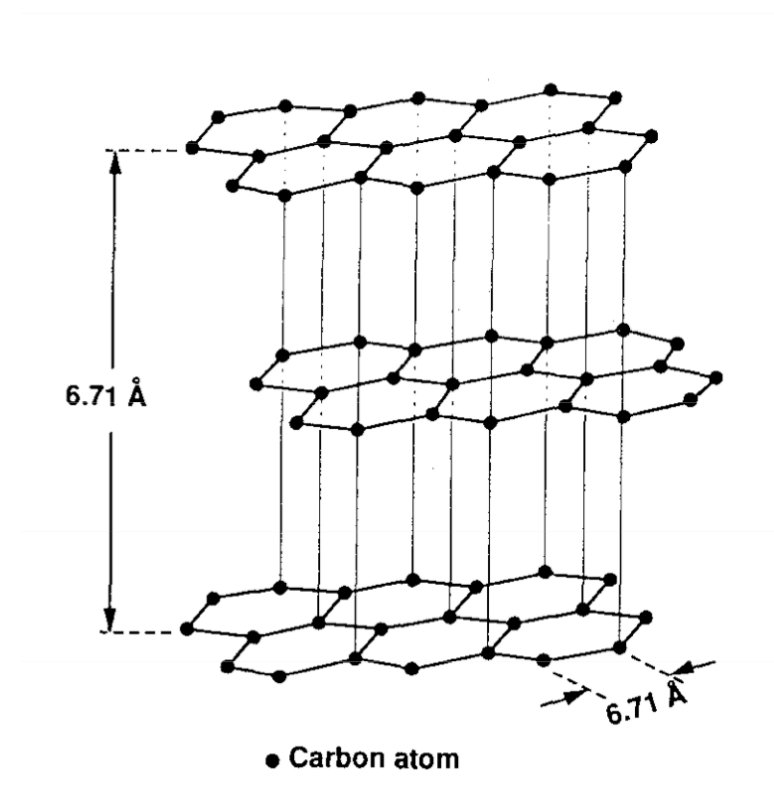
Figure 2.4: Atomic structure of graphite (from [7]).

The chemical bonding of carbon nanotubes is composed entirely of sp^2 bonds, similar to those of graphite. This bonding structure, which is stronger than the sp^3 bonds found in diamonds, provides carbon nanotubes (CNT's) with their unique strength [5,6]. Usually we distinguish carbon nanotubes according to the number of concentric tubes in single-, double-, multi-wall. Single walled carbon nanotubes (SWCNTs) consist of a single sheet of graphene rolled up to form a cylinder with diameter of the order of few nanometers and length up to centimeters. Double-wall carbon nanotubes (DWCNTs), formed by two concentric single-wall behave similarly to single-wall carbon nanotubes but they have unique properties suitable for specific applications. Multi walled nanotubes (MWCNTs) consist of an array of such cylinders formed concentrically and separated by ~0.35 nm, a value similar to the basal plane separation in graphite [7]. MWCNTs can have diameters from 2-100 nm and lengths up to millimeters. Further information on CNTs can be found in chapter 8.

2.2 Diamond

2.2.1 Classification of diamond

No two natural diamonds have exactly the same composition and properties, and any number of classification schemes can be devised. However, only one classification is universally accepted. It is based on the nature and amount of impurities contained within the structure and consists of four types. These types, their origin, and their effect on optical and other properties are summarized in table 2.1 (some diamonds may consist of more than one type).

Type	Ia	Ib	IIa	IIb
Abundance (%)	98	1-2	very rare	Extremely rare
Nitrogen Content (%)	Up to 0.1 (platelets) or up to 5000 ppm	Up to 0.2 (paramagnetic) or synthetic up to 500 ppm	<5ppm or practically zero	Essentially zero
Nitrogen Content (cm^{-3})	10^{19}-10^{21}	-	10^{18}	-
Optical Transparency (nm)	>320	>320	>225	Bluish to blue (boron)
Thermal Conductivity (W/cm K)	9	9	26-32	26
Electrical Resistivity (Ω cm)	>10^{16}	>10^{16}	>10^{16}	10-1000 (p-type) or up to 10 ppm boron
Dislocation Content	Low High mobility	-	High, >10^{5} low mobility	-
Hardness	Possibly not as hard as IIa	-	Possibly harder than Ia	-

Table 2.1: Classification of diamond (from [8]).

2.3 Diamond synthesis

2.3.1 High pressure high temperature

In 1814, the English chemist H. Davy [9] proved conclusively that diamond was a crystalline form of carbon. He showed that only CO was produced when burning diamond without the formation of aqueous vapor, indicating that it was free of hydrogen and water. Since that time, many attempts have been made to synthesize diamond by trying to duplicate nature. These attempts, spread over a century, were unsuccessful. It was not until 1955 that the first unquestioned synthesis was achieved both in the U.S. (General Electric), in Sweden (AESA), and in the Soviet Union (institute for High-Pressure Physics) [10-14]. Conditions for such growth are shown in figure 2.6(a).
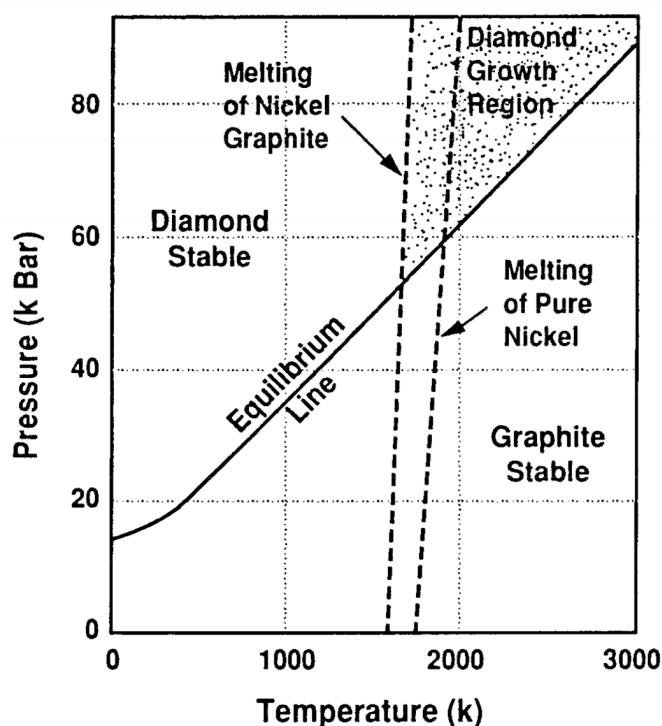
Figure 2.6(a): Pressure-temperature diagram of diamond-graphite (from [13]).
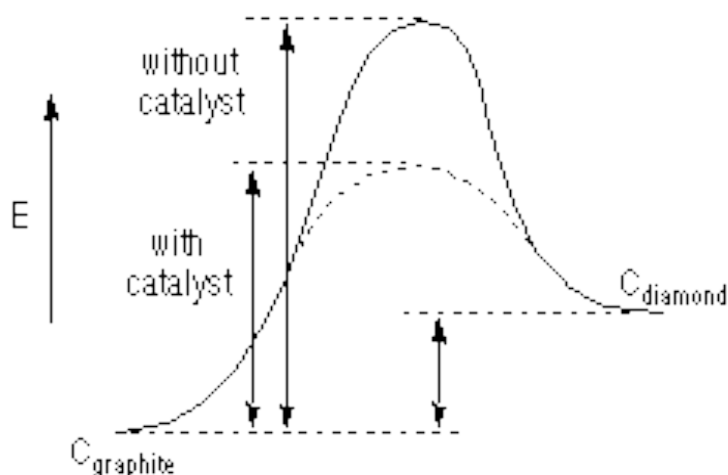
Figure 2.6(b): Catalyst energy diagram (from [13]).

Graphite-diamond transformation although thermodynamically feasible at relatively low pressure and temperature faces a considerable kinetic barrier since the rate of transformation apparently decreases with increasing pressure. This kinetic consideration supersedes the favorable thermodynamic conditions and it was found experimentally that very high pressure and temperature (>130 kb and ~3300 K) were necessary in order for the direct graphite-diamond transformation to proceed at any observable rate [13][14]. These conditions are very difficult and costly to achieve. Fortunately, it is possible to bypass this kinetic barrier by the solvent-catalyst reaction. General Electric and others first demonstrated the solvent-catalyst reaction for graphite-diamond transformation; it establishes a reaction path with lower activation energy than that of direct transformation. This permits a faster transformation under more benign conditions. As a result, solvent-catalyst synthesis is readily accomplished and is now a viable and successful industrial process. The solvent-catalysts are transition metals such as iron, cobalt, chromium, nickel, platinum, and palladium. These metal-solvents dissolve carbon extensively, break the bonds between groups of carbon atoms and between individual atoms, and transport the carbon to the growing diamond surface. The announcement of General Electric's successful synthesis was followed by a

period of considerable activity. It is now possible to produce large crystals of good quality and world production is now at least three times the production of diamond from the earth [15].

2.3.2 Chemical vapour deposition

Diamond chemical vapour deposition (CVD) has been researched since the early 1950's. Eversole first reported the growth of diamond by thermal CVD (using CH_4) in 1954, patented in 1962 [16]. Angus and co-workers repeated Evershole's work and confirmed the mass increase in diamond grit (commercial micron diamond grit, average diameter size 0.1µm) was due to diamond growth [17]. However, this technique at this time in the US was generally believed to not be practical and early work at Union Carbide and Case Western University were not actively followed [16,17]. In the former Soviet Union, a less skeptical attitude prevailed and a research program was aggressively pursued, particularly in the investigation of hydrocarbon-hydrogen pyrolysis and nucleation and the growth mechanisms of diamond. A breakthrough occurred when Soviet researchers discovered the role of atomic hydrogen in removing unwanted graphite whilst leaving diamond untouched [18]. The need to increase the availability of atomic hydrogen soon became apparent and the Soviets developed various methods to achieve that end, such as electric discharge and heated filaments [18]-[20]. The success of the Soviets triggered studies into this technology by the Japanese at the National Institute for Research in Inorganic Materials (NIRIM). Diamond growth using CVD soon became an international research topic where it remains to this day.

The basic reaction in the CVD of diamond is seemingly simple. It involves the decomposition of a hydrocarbon such as methane as follows:

$$CH_4 \text{ (g)} \xrightarrow{\text{activation}} C \text{ (diamond)} + 2H_2 \text{ (g)}$$
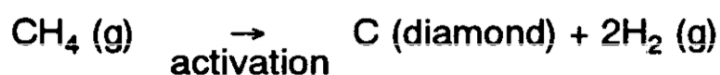
Atomic hydrogen plays an essential role in the surface and plasma chemistry of diamond deposition as it contributes to the stabilization of the sp^3 dangling bonds found on the diamond surface plane [20]. Without this stabilizing effect, these bonds would not be maintained and the diamond plane would collapse (flatten out) to the graphite structure. The other function of atomic hydrogen is to suppress the formation of graphite. In contrast with molecular hydrogen, atomic hydrogen is extremely reactive. It etches graphite 50 times faster than diamond [21]. This etching ability is important since, when graphite and diamond are deposited simultaneously, graphite is preferentially removed while most of the diamond remains [22].

2.3.2.1 Deposition mechanism and model
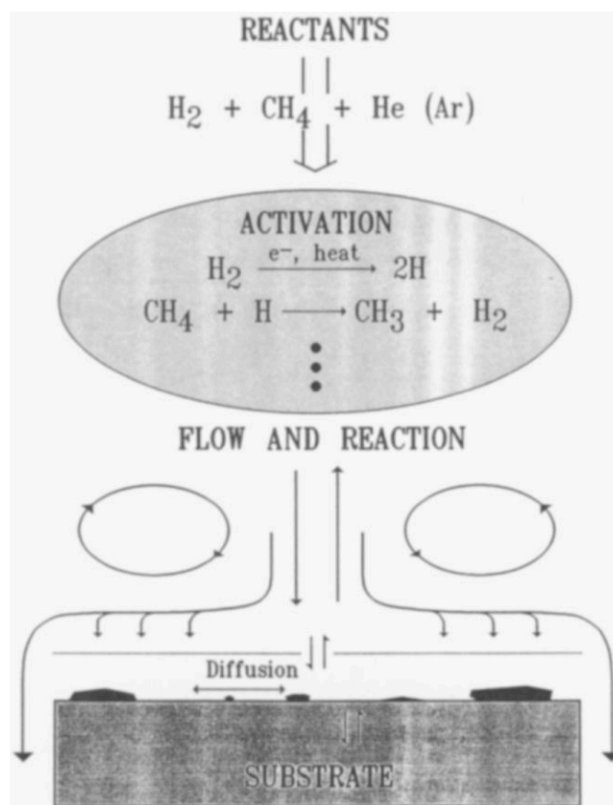
Figure 2.7: Schematic showing the principle elements in the complex diamond CVD process (from [23]).

Diamond has been deposited from a large variety of precursors that include, besides methane, aliphatic and aromatic hydrocarbons, alcohols, ketones, and solid polymers such as polyethylene, polypropylene and polystyrene. These substances generally decompose into two stable primary species: the methyl radical (CH_3) and acetylene (C_2H_2) [24]. A number of studies have been performed to try to identify the growth species [23], and the general consensus is now that the bulk of the evidence supports CH_3 as being the important radical. The basic picture that emerges for CVD diamond growth is believed to be as follows. During growth, the diamond surface is nearly fully saturated with hydrogen. This coverage limits the number of sites where hydrocarbon species (probably CH_3) may adsorb, and also block migration sites once they are adsorbed.

2.4 CVD growth techniques

During the past decades, a large number of new methods were developed to deposit diamond films. In general, diamond thin films can be formed using CVD reaction arising from two basic activation methods shown overleaf:

(1)   Activation by high temperatures (TACVD = Thermally Activated Chemical Vapor Deposition), including hot-filament/hot surfaces, laser heating, arc discharge and arc plasma jet as well as chemically induced hot gas flames.

(2)   Activation by electric or electromagnetic gas discharge (PACVD = Plasma Activated Chemical Vapor Deposition), including microwave and radio-frequency gas discharge, DC and AC glow discharges, as well as plasma jet induced by RF, microwave, DC, etc.

A combination of the above methods, for example, hot-filament + microwave, hot-filament + DC discharge and hot filament + Bias electric potential, etc. has also been developed [25].

Microwave plasma for diamond deposition was first reported in 1983. This technique along with the "hot-filament' method brought diamond thin films much closer to an industrially applicable technology. Magnetized and electron cyclotron resonance (ECR) microwave plasmas were also used for diamond growth [26].

The present status of diamond CVD is summarized in table 2.2. It illustrates that a variety of different methods are capable of depositing high quality coatings on to various non-diamond substrates. Some of these methods like microwave plasma CVD or DC jet CVD are already well established. However, which method to choose will depend primarily on the specific application. If a contamination-free, uniform coating on medium size substrate is required at fairly low equipment costs, then the microwave plasma CVD is probably a good choice. Such units also have the advantage of stability over extended periods of usage and the deposition process can be automated.

Methods	Details	Year of publication
Thermal CVD	Thermal decomposition	1956, 1962
	Chemical transport reaction	1981,1991
	Hot filament technique	1982, 1985
	Oxy-acetylene torch	1988,1991
	Halogen assisted CVD	1956,1991
DC plasma CVD	Low pressure DC plasma	1987,1989
	Medium pressure DC plasma	1987,1990
	Hollow cathode discharge	1988
	DC arc plasmas and plasma jets	1989,1988
RF plasma CVD	Low pressure RF glow discharge	1985,1989
	Thermal RF plasma CVD	1987,1991
Microwave plasma CVD	915 MHz plasma	1988
	2.45 GHz low pressure plasma	1983,1986
	2.45 GHz thermal plasma	1989
	2.45 GHz magnetized plasma	1987,1989
	8.2 GHz plasma	1989

Table 2.2 Methods for synthesizing diamond at low pressures and low temperatures [from 27].

Method	Rate (μm h^{-1})	Area (cm^2)	Quality[*] (Raman)	Substrate material	Advantage	Disadvantage
Hot-filament	0.3-40	100-400	+++	Si, Mo. silica, Al_2O_3, etc.	Simple, large area	Contamination, stability
DC discharge (low P)	<0.1	70	+	Si, Mo. silica, Al_2O_3, etc	Simple, area	Quality, rate
DC discharge (medium P)	20-250	<2	+++	Si, Mo, Al_2O_3	Rate, quality	Area
DC plasma jet	10-930	2-100	+++	Mo, Si, W, Ta, Cu, Ni, Ti, stainless steel	Highest rate, quality	Stability, homogeneity
RF (low P)	<0.1	1-10	-/+	Si, Mo, silica, BN, Ni	Scale-up	Quality, rate, contamination,
RF (thermal,1 atm)	30-500	3-78	+++	Mo	Rate	Stability, homogeneity
Microwave (0.9 - 2.45 GHz)	1(low p), 30 (high P)	40	+++	Si. Mo, silica, WC, etc.	Quality, area, stability	Rate
Microwave (ECR 2.45 GHz)	0.1	<40	-/+	Si	Area, low P	Quality, rate, cost, contamination
Flame. (combustion)	30-200	1-100	+++	Si, Mo, $A1_2O_3$, TiN	Simple, rate	Stability, uniformity

[*] - = poor quality, +++ = excellent quality

Table 2.3: A comparison of CVD techniques (from [28]).

2.5 Diamond nucleation mechanisms

It has become increasingly evident that further technological development in CVD of diamond films, particularly in such challenging areas as single-crystal growth for electronic applications and low-temperature deposition for coating on optic and plastic materials, requires a detailed understanding and control of the fundamental phenomena associated with diamond nucleation and growth. These phenomena, especially the nucleation and early growth stages, critically determine film properties, morphology, homogeneity, defect formation, adhesion, and the type of substrates that can be successfully coated. For example, an increase in surface nucleation density is known to reduce morphological instabilities [29] and surface roughness of diamond films [30]. Here, diamond nucleation mechanisms are reviewed on the basis of available literature.

2.5.1 Surface nucleation

Diamond can grow homoepitaxially on a diamond surface without nucleation problems in HFCVD [31][32-34], MWPACVD [35,36] and ECR MW PACVD [37] from a variety of carbon sources. Diamond also nucleates easily on c-BN [38-40] due to the identical crystal structure and the nearly identical lattice constant (mismatch 1.4%) and thermal expansion. However, in most CVD processes, diamond nucleation on non-diamond surfaces without pretreatment is usually very slow. A conventional growth process in CVD of polycrystalline diamond films typically shows several distinguishable stages [41]: (i) incubation period (formation of stable surface carbide layer), (ii) 3-D nucleation of individual crystallites on substrate surface, (iii) termination of surface nucleation, and 3-D growth of individual crystallites, (iv) faceting and coalescence of individual crystallites, and formation of continuous film, and (v) growth of continuous film. Before nucleation starts, an incubation period

may take from a few minutes up to hours [42-44] depending on substrate materials, surface pretreatment and deposition parameters. The isolated nuclei/micro-crystals formed during nucleation exhibit sphere-like geometry. With increasing time, the nucleation density increases to a certain value, then the surface nucleation terminates. The isolated crystals grow homogeneously in size and faceting develops due to abundant C surface diffusion from the relatively large diamond-free area surrounding them. When the isolated crystals coalesce together, a continuous film forms.

Spitzyn *et al* [31] considered the surface nucleation process to be the primary process responsible for diamond nucleation. In their experiments, diamond was nucleated on non-diamond substrates (poly- or single crystalline Au, Cu, Si, Mo, W). The substrates were polished with abrading grits (diamond, zirconia or others), or etched, or seeded with diamond crystals prior to deposition. Crystals a few tens of micrometers were grown with octahedral and cube-octahedral habits under the same conditions as used for growth on diamond substrates. Nucleation rates of 10^5 - 10^8 cm^{-2} h^{-1} were obtained. A continuous film of 2µm in thickness was grown, corresponding to a minimum nucleation density of 2.5×10^7 cm^{-2}. A 100nm thick, polycrystalline SiC interfacial layer was identified by Auger spectroscopy on Si substrates. From their studies, some general features associated with surface nucleation processes of diamond may be summarized as follows:

1. Diamond nucleation rates on non-diamond substrates vary from 10^3 - 10^8 cm^{-2} h^{-1}, depending on synthesis conditions, substrate materials and surface pretreatment methods (polishing, etching, seeding, or annealing).

2. Nucleation of diamond crystals is observed mostly on defects such as scratches, grain boundaries, dislocation outcrops, etc., suggesting that nucleation occurs on the substrate surface, and not in the gas phase.

3. Diamond nucleation rates are several times lower on single-crystal substrates than on polycrystalline substrates of the same material after identical surface pretreatment.

4. Diamond nucleation rates on carbide-forming substrates (Si, MO) are one to two orders of magnitude higher than on substrates that do not form carbides (Cu, Au).

5. Diamond nucleation rates on foreign substrates decrease as the substrate coverage with diamond and the crystal size increase.

A number of experimental observations on diamond nucleation processes [45-50] reveal that in most cases, diamond does not nucleate directly on a non-diamond substrate surface, but instead, on an intermediate layer that develops at the interface between diamond and the non-diamond substrate during the incubation period before diamond nucleation begins. The intermediate layer, formed due to the chemical interactions of activated gas species with the substrate surface, may consist of *diamond-like amorphous carbon* (DLC, a-C, or a-C:H), *metal carbides*, or *graphite*, depending on substrate materials, pre-treatment methods and deposition parameters. It is generally proposed that the intermediate layer provides nucleation sites for diamond crystallite growth, hence enhances diamond nucleation densities on non-diamond substrates, and offers an opportunity for controlling the morphology, orientation, and texture of diamond films during nucleation and growth.

(a)   (b)

(c)
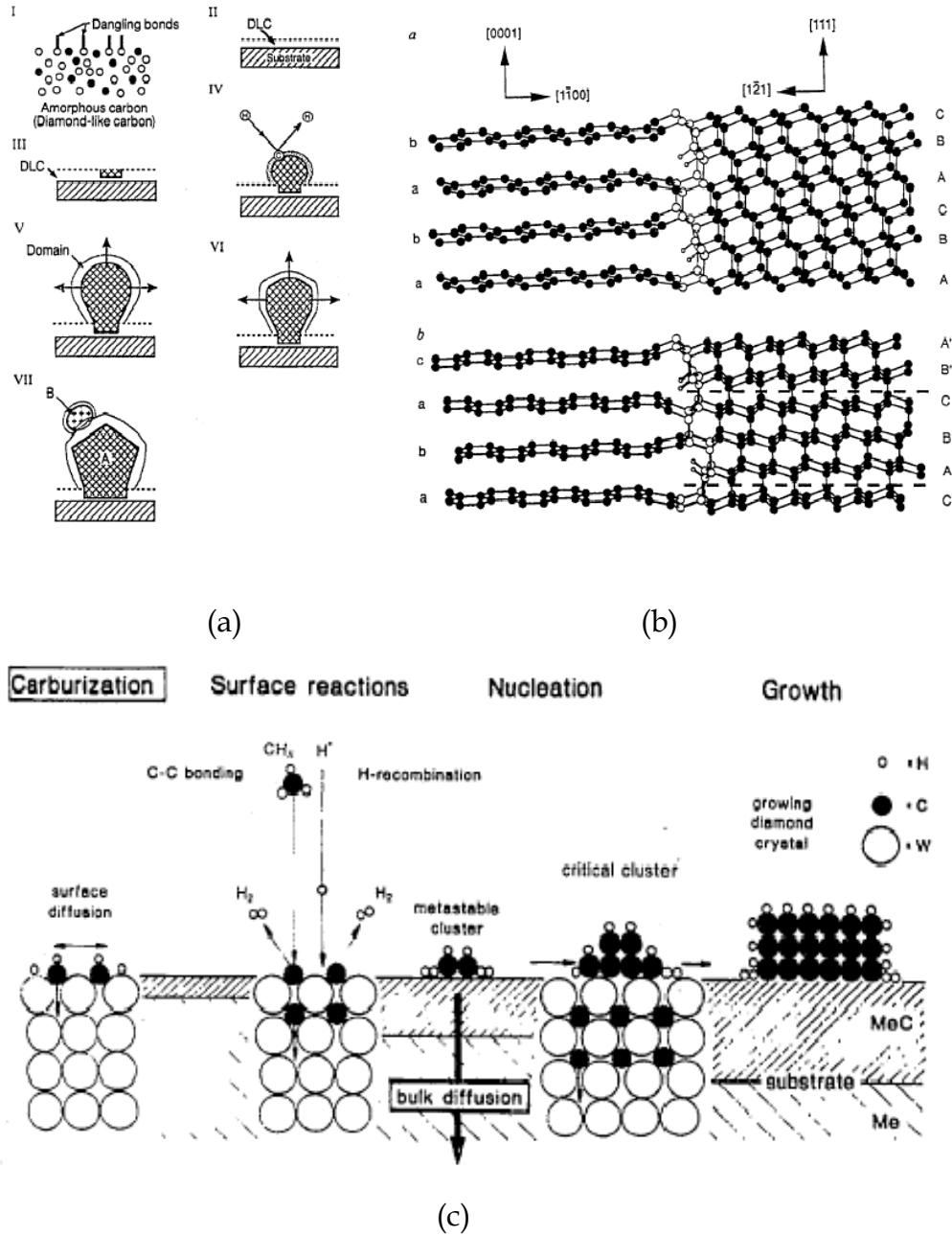
Figure 2.9: Summary of nucleation mechanisms thought to   account for nucleation of diamond on most substrates: (a) On a DLC interlayer: (I) formation of carbide clusters, bonding change from sp^1 to sp^2; (II) sp^2 converts to sp^3, (III) amorphouse phase crystallises; (IV-VI) growth and faceting of diamond crystals; (VII) secondary nucleation and growth. (b) On a graphite interlayer: Condensation of graphite followed by hydrogenation of the $\{1\bar{1}00\}$ prism planes along edges of graphite particles; diamond nucleation at emerging stacking fault - almost perfect interface. Upper: cubic diamond on

perfect hexagonal graphite, lower: twinned diamond nucleus adjoining a graphite stacking fault. Twin boundaries: dash lines, H-atoms: open circles, C-atoms: solid circles. (c) On a carbide interlayer: Carburisation consumes available C to form carbide surface; C surface concentration below diamond nucleation minimum; carbide layer thickness increases; C transport rate decreases, C surface concentration increases; diamond nucleus forms when either surface C concentration reaches critical level or C cluster attains critical size (from [29]).

Diamond can nucleate on foreign surfaces, notably elements that form refractory carbides (Si, Mo, Ta, W), without pretreatment. Thermodynamic calculations reveal that, in the absence of a plasma, SiC (as opposed to diamond or graphite) is the only stable phase expected on a heated Si substrate under conditions of 0.3 vol.% CH_4 in H_2, 30 Torr pressure, and 1000°C substrate surface temperature [51].

Badzian [52] suggested that diamond nucleation on Si is preceded by the formation of a β-SiC buffer layer, and diamond nucleation occurs on the surface of the carbide. This is supported by many growth experiments [53-57] of diamond particles or films on Si substrates in HFCVD, which shows that the Si surface is indeed transformed to SiC under conditions leading to diamond growth, and diamond nucleation occurs on the SiC intermediate layer.

Lindlbauer [58] conducted systematic studies of diamond growth on carbide-forming refractory metals and observed that diamond nucleation occurred only after the formation of a thin carbide layer.

As shown in figure 2.9, carbon dissolves into the substrate material initially, resulting in the formation of a stable carbide. Diamond nucleation occurs on the carbide layer when the carbon concentration on the surface reaches its saturation value. Thus, C diffusion rate influences both the carbide growth and

diamond nucleation. Lux and Haubner [59] compared the time evolution of diamond nucleation densities on Ti, Hf, Nb, Ta, Mo, and W, and found that the difference in the nucleation densities and rates is related to the diffusivity of carbon in the respective substrates. The incubation period for nucleation is the shortest on metal that can most rapidly achieve a super-saturation of carbon on the surface.

2.6 Diamond growth by CVD methods

2.6.1 Substrate materials for diamond growth

The nature of the substrate and its pre-deposition treatment play a major role in determining the surface nucleation rate but not necessarily the rate of subsequent growth (after the immediate surface layer is deposited) [60,61]. Diamond surfaces or particles provide the best nucleation potential [62]. The most widely used non-diamond substrate is still silicon, other materials can also be used for diamond growth such as the refractory metals (W, Ta, Mo), carbides (WC, SiC), and other metals such as Cu, Au and Ni and their alloys [63]. Cubic boron nitride (c-BN) is also a suitable substrate with good lattice matching but is only available as small single crystals. Metals where there is significant carbon solubility or reaction with C include Pt, Pd, Rh; these materials cannot be coated with a diamond film.

Materials that form carbides can be used as potential substrates for diamond growth, such as Ti, Zr, Hf, V, Nb, Ta, Cr, Mo, W, Co, Ni, Fe, Y, Al, and certain other rare-earth metals. Non-metals, such as B or Si, and Si-containing compounds such as SiO_2, quartz and Si_3N_4, also form carbide layers. Nucleation rates on stable carbide-forming substrates are one to two orders of magnitude higher than on non-carbide-forming substrates (Cu and Au).

To combat the prohibitively long period (hours even days) before diamond growth occurs on non-diamond substrates, various treatments have been developed to ensure rapid diamond nucleation and growth. These procedures are discussed in the following sections.

2.6.2 Nucleation enhancement techniques

The most often used method for enhancing diamond nucleation is scratching, abrading or blasting non-diamond surfaces with diamond particles or paste, although the method is acceptable only for limited applications (not for optical, for instance). Diamond nucleation densities after scratching pretreatments range typically from 10^6 to 10^{10} cm^{-2} [64,65], as compared to <10^5 cm^{-2} on untreated surfaces. Surface scratching may also be accomplished in an ultrasonic vibrator using abrasive paste suspended in methanol or acetone [66]. An ultrasonically damaged surface has more uniformly distributed defects and leads to more reproducible effects. Nucleation densities following this pretreatment are normally between 10^7 to 10^{11} cm^{-2}. Scratching substrates with diamond powder or other abrasive materials significantly enhances surface nucleation density and rate compared to untreated substrates [67,68]. Different suggestions have been made to account for the mechanisms of the nucleation enhancement by scratching. The first of these is the seeding effect [69,70] where diamond, DLC or other carbonaceous residues from polishing or abrading powders left adherent to or embedded in the polished surface provide nucleation sites for diamond growth [71]. The second possible mechanism is that the highly disordered surface materials or microscopic crater edge sites on the polished surface create high-energy sites for nucleation [72,73]. Also, it is thought [50] scratching produces non-volatile graphitic particles through local pyrolysis of absorbed hydrocarbons. These graphitic clusters would be subsequently hydrogenated in the atomic hydrogen environment under the typical CVD conditions to form the precursor molecules. Regarding the effect of various abrasives on diamond nucleation, it

is found that polishing with diamond has the most pronounced effect, and the effect decreases in the order diamond > c-BN > SiC [74].

Scratching and seeding cause surface damage and contamination, and cannot be easily applied to substrates of complex geometry and shape. Therefore, these pretreatment methods are incompatible with many applications that require extremely smooth, clean surfaces, such as diamond films for electronic devices, optical window materials and smooth wear-resistant coatings. Alternative pretreatment methods that can yield high diamond nucleation densities without damaging substrate surfaces are therefore of particular importance. Biasing pretreatment of substrates has been increasingly employed to enhance surface nucleation of diamond [75-79]. Yugo *et al* [78] employed a negative bias (-70V) and high CH_4 (5%) concentrations during pretreatment to generate diamond nuclei on a Si mirror surface in PACVD. The several-minute pretreatment resulted in an enormous nucleation enhancement. Diamond nucleation densities as high as 10^{10} cm^{-2} were achieved.

In an in-depth study of diamond nucleation on Si in MWPACVD [80], substrates were pretreated by negative biasing in 2% CH_4 - H_2 plasma. The biasing enhanced diamond nucleation density on unscratched Si wafers, up to 10^{11} cm^{-2} as compared to 10^7 cm^{-2} on scratched Si wafers and 10^3 - 10^5 cm^{-2} [80] on untreated Si wafers.

2.6.3 Effect of hydrogen, nitrogen, oxygen and noble gases

The reaction gas used in low-pressure diamond synthesis methods contains relatively low concentrations of volatile carbon compounds with a high excess of hydrogen. Activation of such a gas mixture is carried out to obtain the highest possible concentration of atomic hydrogen. Atomic hydrogen plays a major role in mediating rates and in maintaining a proper surface for growth.

Low molecular weight hydrocarbon species (e.g., CH_3 and C_2H_x) are believed to be responsible for the extension of diamond lattice. A complete understanding of the attachment mechanism, however, has not yet been achieved. A number of hydrogen-carbon compounds have already been used successfully as carbon source.

The essential features of the synthesis, as characterized by the following two reactions, proceed simultaneously: (1) The decomposition reaction; it consists of a normal pyrolitic hydrocarbon chemical vapor deposition reaction; (2) The etching reaction by the atomic hydrogen; this prevents the formation of all other weakly bonded solid carbon compounds except diamond. The presence of a small amount of nitrogen in the CH_4/H_2 gas mixture is not harmful. But the presence of both nitrogen and oxygen seems to be detrimental. In this case, due to the gas activation, NO_x compounds can react with the atomic hydrogen and reduce its concentration. Nitrogen as an impurity leads to a complete change in the texture and surface morphology [80]. However, oxygen additions to the gas mixture without nitrogen are probably not harmful at all and can even have positive effects [81]. The addition of small amounts of oxygen leads to the formation of transparent diamond crystals due to the reduction of crystal defects [78].

Argon or other heavier noble gases can effectively increase the electron density of the plasma that promotes the equilibrium of hydrogen atoms and ions and improves the properties of the deposited films [82]. Similar to nitrogen and oxygen, these noble gases have significant effects on surface morphology and crystalline structure of diamond films. By adjusting the noble gas/hydrogen ratio in the gas mixture, a continuous transition from micro to nanocrystallinity is achieved [83].

2.7 Doping diamond

Owing to its metastability, diamond cannot be heated to temperatures at which vacancies and interstitial atoms form by thermal excitation. Thus, any diffusion process that relies on these defects as carriers is not possible. For this reason, it is difficult to introduce dopant atoms by in-diffusion as in the case of silicon. Even if they can diffuse in by some interstitial atom mechanism, there will not be vacant lattice sites available for them to occupy and hence to become electrically active. The possible methods are limited to dopant uptake during growth or dopant injection by means of ion implantation.

2.7.1 During growth (p-type)

P-type boron containing diamonds exist in nature (type llb natural diamond), and their optical and electrical properties have been extensively studied and documented [84]. Boron doped HPHT diamond was first reported by Wentorf *et al* [85] by adding boron to the metal catalyst during synthesis. Under HPHT conditions, the solvent catalyst often contains materials that getter the nitrogen in order to stop its incorporation and to prevent these atoms from compensating the boron. In general, these boron-doped diamonds tend to be over-doped and of insufficient quality for electronic applications due to the inevitable contamination of the diamond by the catalyst and nitrogen. The quality of boron-doped diamond layers grown by PACVD has improved steadily over the last ten years, and single crystalline layers grown homoepitaxially on diamond with hole mobilities in excess of 1000 cm^2/Vs can now be produced [86]. Boron is an electrically active dopant for p-type diamond with an activation energy of 0.37eV above the valence band edge [87]. This large ionization energy results in the activation of less than 1% of the dopants at room temperature [88]. Diborane (B_2H_6), boric acid, and boron oxides [89-91] have been used as impurity sources, which are mixed into the source gases for epitaxial growth. The activation energy required to excite a

hole into the valence band has been demonstrated to be concentration dependent, reducing to a few meV at boron concentrations $>1\times10^{20}$cm^{-3} [87]. This has been attributed to the formation of an impurity band [92,93].
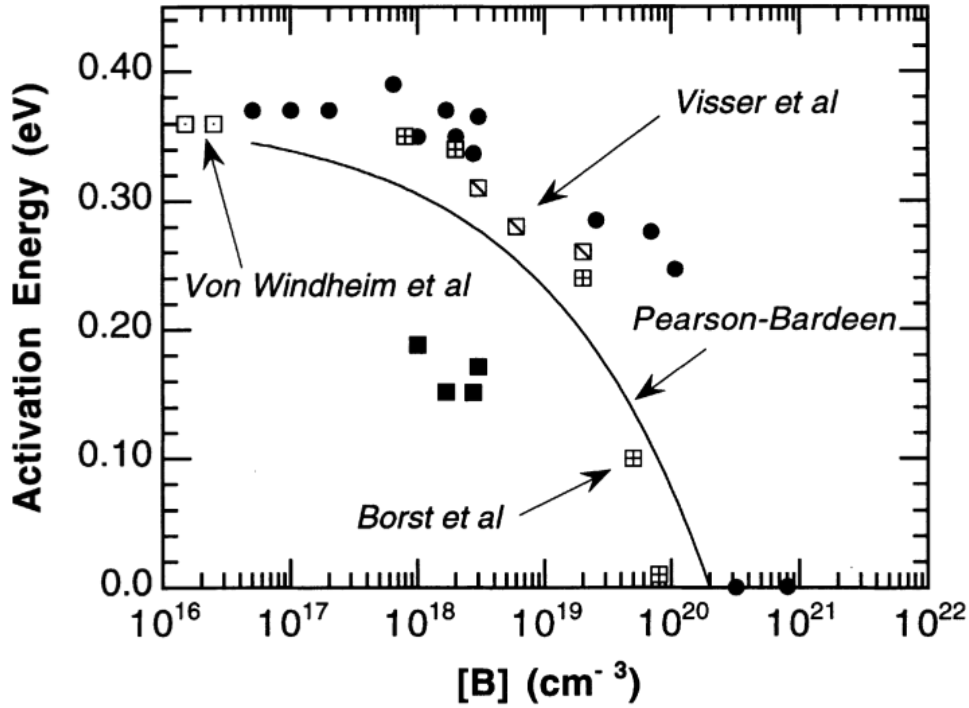

Figure 2.10: Conductivity activation energies at 300 K as a function of boron content. At about [B] > 3 x 10^{18} cm^{-3} the activation energy starts to decrease and finally vanishes for [B] > 2 x 10^{20} cm^{-3}. The theoretical dependence according to the model of Pearson and Bardeen (solid curve) is given for comparison (solid line) [94]. (From [95]).

2.7.2 During growth (n-type)

Among the group V elements, which are potential substitutional donors in group IV semiconductors, only N and P seem to enter the diamond crystal and contribute to its electrical properties. Nitrogen is abundant in natural diamonds, and can be synthesized under HPHT laboratory conditions with an activation energy of 1.7eV [96]. Due to these very high ionization energies, N containing diamonds are electrically insulating at room temperature. P and N

can be introduced into the diamond also during CVD growth. Phosphorus on a substitutional site in diamond was predicted to act as a shallow donor (0.1 eV) [96]. Good-quality n-type diamond still poses a significant problem due to diamonds extremely dense atomic arrangement. It has not yet been possible to grow such diamonds by HPHT methods, although a limited amount of doping with phosphorus atoms can be observed optically [97]. Many attempts have been made to incorporate phosphorus atoms into diamond during PACVD growth. Unequivocal proof of P-donor activation has been demonstrated for homoepitaxial diamond (111) layers [98]; however, the Hall mobility is very low ~5 cm²/Vs at room temperature and 23 cm²/Vs at 500K. Phosphorus-doped diamond films tend to have a nondiamond structure and considerable hydrogen incorporation [99]. It has also been reported that phosphorus-doped (111) diamond films contain more defects and more hydrogen than undoped (111) diamond films [100]. It has been suggested that the markedly low value of the mobility can be attributed to scattering by a large amount of un-ionized phosphorus atoms and crystal defects in phosphorus-doped diamond films. Furthermore, the activation energy for electron excitation into the conduction band lies at $E_a > 0.5\text{eV}$, ruling out bipolar electronic device operation at room temperatures.

2.7.3 Ion implantation

Ion implantation is widely used to dope silicon and other semiconductor materials. The dopant atoms are ionized and driven to high velocities by electric fields in an accelerator (ion implanter) where they impinge on to the surface of the semiconductor substrate, and are injected into the underlying bulk to a depth that depends on the mass and energy of the ions. In this way, it is possible to control accurately the number and location of the dopant atoms. However, the process also introduces a large number of defects per ion, primarily vacancies, and interstitial atoms, which have to be removed by subsequent annealing. In diamond, commensurately high temperatures cannot

be used, and the presence of these defects can even lower the temperature at which graphitization is initiated. In fact, if the ion dose is too high, graphitization is inevitable. The greatest success has been reported when using the cold implantation-rapid annealing (CIRA) routine [101]. The ions are implanted at a range of energies to create as large a depth-width ω (spatial distribution of dopant beneath the surface) as possible, and to doses well below the graphitization threshold. The implantation is carried out at 77K at energies up to 120KeV with a total B dose of $4 \times 10^{15} cm^{-2}$. At this temperature all the point defects become "frozen" into the positions at which they are created, allowing for suitable post-annealing (up to 1750°C) to activate the boron atoms. The dopant atoms exhibited an electrical activation energy of 0.37eV. Very high p-type doping ($n_a = 2 \times 10^{19}$ cm^{-3}) suitable for contacting p-type diamond was achieved by Kalish *et al* [102,103] by B implanting polycrystalline CVD diamond layers by two different methods: (I) high dose B implantations (above the critical dose for graphitization upon annealing), followed by annealing (1300 K) and chemical removal of the graphitized surface layer to expose a thin, highly conductive over-doped layer [102]; (II) high dose high current (current densities up to 500 A/cm^2) B implantations into poorly heat-sunk samples [103], thus heating the sample during implantation to temperatures of the order of 1100°C. This hot implantation approach does not require any further need for annealing, leaving a highly doped relatively undamaged layer which exhibits high conductivity.

Ion implantation, as a technique, offers precise control of dopant concentration as ion bean current can be measured. Good uniformity over the surface, uniform depth profile obtained by multiple implantations at different energy levels and selective doping at preferential sites are other advantages of this technique. However, the drawback is the inevitable lattice damage caused by ion bombardment.

2.7.4 Surface conductivity

The diamond surface can be terminated by a variety of elements or molecules, giving rise to new phenomena and applications. Hydrogen terminated diamond gives rise to a negative electron affinity due to the formation of carbon-hydrogen dipoles [104]. In vacuum such surfaces are insulating, however, if hydrogen terminated diamond films are exposed to air, surface conductivity can be detected [105, 106]. Hall effect experiments revealed the p-type nature of surface conductivity [107,108], with typical hole sheet-densities between (10^{10} – 10^{13}) cm^{-2} [108, 109], and Hall mobilities between 1 and 100 cm^2/Vs [109, 110]. It is now well established that for surface conductivity to occur hydrogen termination in combination with adsorbate coverage is required, this led to the "transfer doping model" [105, 106, 111]. For electron tunneling to occur the Fermi level of the adsorbate coverage must be lower than the valence band maximum (VBM) of diamond (figure 2.11).
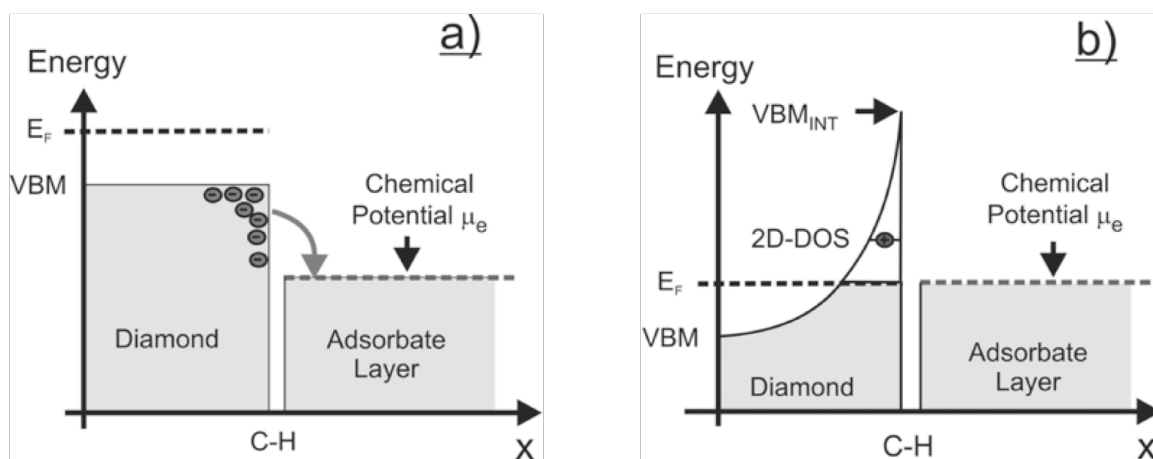

Figure 2.11: Schematic showing the diamond/adsorbate junction in (a) non-equilibrium (b) equilibrated. Electrons shall tunnel into the empty electronic states in the adsorbate layer as long as its chemical potential μ_e is lower than the Fermi energy E_F (from [112]).

The origin of surface conductivity is due to holes created in the diamond near surface as a result of electrons tunneling into available states in the adsorbed electrolyte layer. There exists good agreement in the literature for this model. The major drawback with diamond surface conductivity as a future technology is that it is highly sensitive to atmospheric conditions and temperature making it less attractive for device applications.

2.8 Properties of diamond

Diamond's extreme properties derive from its strong, covalent carbon-carbon bonds (sp^3 bonds). Within the crystal, each carbon atom is symmetrically bonded to four neighboring carbon atoms situated at the corners of a surrounding tetrahedron. Diamonds structure is also responsible for a number of its other physical properties. For example, diamond is more radiation-hard than any other solid, also the ease at which phonons can travel through the lattice gives rise to its very high thermal conductivity. Selected properties of diamond are presented in table 2.4.

	CVD Diamond	Single–crystal Diamond
Density (g cm^{-3})	2.8-3.51[4]	3.515
Thermal capacity at 27′C (J/ mol·K^{-1})	6.12	6.195
Standard entropy at 27% (J/ mol·K^{-1})		2.428
Standard enthalpy of formation at 27′C (J/mol)		1.884
Effective Debye temperature at 0-827°C (K)		1860 +/- 10
Thermal conductivity at 25°C (W/m·K^{-1})	2100	2200
Thermal expansion coefficient at 25-200°C (x10^6 °C^{-1})	2.0	0.8-1.2
Band gap (eV)	5.45	5.45
Electrical resistivity (Ω cm)	10^{12}-10^{16}	10^{16}
Dielectric constant at 45 MHZ to 20 GHz	5.6	5.7
Dielectric strength (V/cm)	10^6	10^6
Loss tangent at 45 MHZ to 20 GHz	<0.0001	
Saturated electron velocity (x 10^7 cm/s)	2.7	2.7
Carrier mobility (cm^2/Vs) **Electron (n)** **Hole (p)**	4500 3800	2200 1600
Young's modulus (GPa)	820-900	910-1250
Compression strength (GPa)		8.68-16.53
Poisson's ratio		0.10-0.16
Vickers hardness (GPa) [varies with crystal orientation]	50-100	57-104
Index of refraction at 10 μm	2.32-2.42	2.40

Table 2.4: Properties of Diamonds (from [29]).

Diamond has many superior properties among them being electron and hole mobilities, which are amongst the highest of all semiconducting materials, high electric breakdown field, chemical inertness and its intrinsic resistivity. A summary of CVD diamond and other semiconductor material properties are displayed in table 2.5.

Property	Si	GaAs	βSiC	CVD Diamond
Dielectric constant at 198Hz	11.8	10.9	9.7	5.5
Dielectric strength (V/cm)	0.3-0.5	0.6	4	4-10
Bandgap (eV)	1.12	1.43	2.3-3.0	5.47
Saturated electron velocity (x 10^7 cm/s)	1.0	2.0	2.5	2.7
Carrier mobility (cm^2/Vs) Electron (n) Hole (p)	 1350-1500 480	 8500 400	 400-1000 50	 4500 3800
Semiconductor temperature limit (ºC)	150	250	>1000	500
Thermal conductivity (W/cm ·K^{-1})	1.5	0.5	5	21

Table 2.5: Electronic properties of diamond and other semiconductor materials (from [113]).

2.9 Applications of diamond

Applications for natural diamonds are limited by their size, cost and physical characteristics as each naturally occurring gemstone is slightly different,

nonetheless this material has a very large market, particularly in gemstones. CVD diamond, on the other hand, offers a broader potential since size, and eventually cost, are less of a limitation. It also opens the door to applications that would take full advantage of the intrinsic properties of diamond in such areas as semiconductors, optics, optoelectronics, wear and corrosion coatings, and others. Table 2.6 displays some established and potential applications of CVD diamond.

Grinding, cutting	Inserts, Twist drills, Whetstones, Oil drilling tools, Slitter blades, Surgical scalpels, Saws
Wear parts	Bearings, Jet-nozzle coatings, Slurry valves, Extrusion dies, Abrasive pump seals, Computer disk coatings, Engine parts, Medical implants, Ball bearings, Drawing dies, Textile machinery
Acoustical	Speaker diaphragms
Diffusion, corrosion	Crucibles, Ion barriers (sodium), Fiber coatings, Reaction vessels
Optical coatings	Laser protection, Fiber optics, X-ray windows, Antireflection, UV to IR windows, Radomes
Photonic devices	Radiation detectors, Switches
Thermal management	Heat-sink diodes, Heat-sink PC boards, Thermal printers, Target heat-sinks
Semiconductor	High-power transistors, High-power microwave, Photovoltaic elements, Field-effect transistors UV sensors, high temperature electronic devices
Electrochemical	electrodes, electro-chemical detectors, bio-chemical sensors

Table 2.6: Some actual and potential applications of CVD diamond (from [2]).

2.9.1 Grinding and cutting

Diamond is the hardest of all natural materials. As steel is to butter, so is diamond to steel. CVD-diamond coatings provide excellent protection against chemical and physical abrasion and wear due to their great hardness and wear resistance, good lubricating properties, and their general chemical inertness. As such, they have found a niche in cutting and grinding applications.

2.9.2 Thermal management

The design of integrated circuits (ICs) has reached the point where one million or more components can be put on a single chip (known as very large scale integration or VLSI) and higher densities will soon be needed as circuit designers are constantly demanding higher performance, expanded memory, faster access time, and shrinking geometry which now reaches the nanometer scale. To remove this heat, it is often necessary to use hybrid circuits and bulky heat-dissipation devices or complicated and expensive refrigeration since present heat-sink materials are no longer adequate. Diamond, an electrical insulator with the highest thermal conductivity at room temperature, provides a solution. It compares favorably with conventional heat-sink materials such as aluminum, copper, or ceramics such as beryllia and aluminum nitride [114-116]. A diamond heat-sink should allow clock speeds greater than 100 GHz compared to the current speeds of less than 40 GHz, although improvements to interconnects shall need to be met for this to be achieved.

2.9.3 Optical applications

Diamond is extremely hard, chemically inert, has an excellent thermal conductivity, and has a wide range of transparency and a low coefficient of thermal expansion. These properties make diamond superior to any other existing window material used for transmitting infrared and microwave

Therefore, synthetic diamond has the potential to replace zinc selenide as the output window of high-power CO_2 lasers and gyrotrons. Those synthetic diamond windows are shaped as disks of large diameters (about 10 cm for gyrotrons) and small thicknesses (to reduce absorption) and can only be produced with the CVD technique [117,118]. Recent advances in the HPHT and CVD synthesis techniques has led to greater purity and crystallinity of single-crystalline diamond, enough to replace silicon as a diffraction grating and window material in high-power radiation sources, such as synchrotrons [119]. Both the CVD and HPHT processes are also used to create designer optically transparent diamond anvils as a tool for measuring electric and magnetic properties of materials at ultra high pressures using a diamond anvil cell [120].

2.9.4 Electronic and semiconducting applications

With its excellent semiconductor properties, good radiation and temperature resistance, and high thermal conductivity, diamond is the ideal material for many semiconductor applications such as high-power and high frequency transistors and cold cathodes, or in the harsh environment found in internal-combustion and jet engines. CVD diamond is now commercially available, making it possible to take advantage of these properties. Great strides have been made in doping diamond with boron during the CVD process, this is now an established technology with many laboratories worldwide routinely performing this. There exist many examples in the literature of semiconductor devices based on CVD diamond such as field-effect transistors (FETs) that are proving superior to silicon devices and are characterized by high-power handling capacity, low saturation resistance, and excellent high-frequency performance [121]. However, for CVD diamond to be seriously considered as an electronic material, reproducible high quality n-type diamond is a necessity; proof of P-donor activation has been demonstrated for homoepitaxial diamond (111) layers [98], however, the Hall mobility reported here was very low (5-

$28 cm^2/Vs$) and few studies on phosphorous doped diamond have been reported since this breakthrough. Hence, to date, most devices made from diamond are unipolar utilizing the p-type hole conduction. These include Schottky diodes on boron doped diamond operating up to 1000^oC [122], boron/nitrogen *pn*-junction diodes [123,124], bipolar transistors based on this *pn*-junction [124] and field effect transistors (FETs) with boron delta-doped channels [125] and hydrogen-related surface conductive layers [126,127]. CVD diamond has also been studied extensively as a solid-state detector of in particular UV and X-ray wavelengths [128,129] and particle detection [130,131]. Studies on these diamond-based detectors demonstrate their inherent advantages; however further improvements to the diamond growth process and surface polishing techniques are required for this technology to become feasible.

2.9.5 Electrochemical applications

The unique bulk and surface properties of diamond make it extremely attractive for applications in electroanalysis and electrochemical synthesis. Conducting diamond electrodes, made by boron-doping CVD diamond films, have been found to have a very large potential window in water [132]. This is a great advantage over other electrode materials, such as Pt, which dissociate water at higher electrode potentials resulting in the unwanted evolution of hydrogen and oxygen. Diamond is extremely resistant to oxidation and attack by acids, even at elevated temperatures. Unlike nearly all other electrode materials, diamond is also resistant to attack by hydrofluoric acid. Platinum electrodes have been used for generating oxidising species in HF solutions for the etching of silicon in the absence of nitric acid. However, the solution eventually becomes contaminated with trace amounts of platinum, which in turn can contaminate the silicon surface. Replacing the platinum electrode with a diamond electrode has removed this contamination problem and in some cases the diamond electrode has been used to measure the extent of any contamination in the HF solution [133]. Some organic chemicals such as

phenol have the ability to react with metal electrodes, resulting in the electrode surface becoming inactive. This is termed as 'fouling'. Diamond is thought to be much less prone to fouling [134], although other authors note that de-activation due to fouling of the diamond does occur, unless the diamond anode is periodically run at a high potential (E > 2.3 V versus the standard hydrogen electrode (SHE)). Changing the polarity of the electrodes periodically can also prevent build up of foreign material on the diamond surface [135]. Furthermore, should the diamond surface become fouled in an industrial application, an acid flush can be used to re-activate the surface without degrading the diamond electrodes.

2.10 References

1. http://www.chemicool.com/elements/carbon.html

2. H.O. Pierson, Handbook of Carbon, Graphite, Diamond and Fullerenes, Noyes, Park Ridge, NJ (1993).3a. C. Y. Fong, B. M. Klein, in Diamond: electronic properties and applications, edited by Lawrence S. Pan, Don R. Kania Boston: Kluwer Academic , c1995.

3. Carey, Francis A.; Sundberg, Richard J. Advanced Organic Chemistry - Part A: Structure and Mechanisms (5th Edition).. Springer - Verlag.

4. R.F Davis, Diamond Films and Coatings.. William Andrew Publishing/Noyes (1993).

5. M.S Dresselhaus and M.Endo, in Carbon nanotubes: synthesis, structure, properties, and applications edited by MS Dresselhaus, G Dresselhaus, P Avouris (Springer-Verlag, Berlin Heilberg, 2001), p.11.

6. P. Delhaes, *Graphite and Precursors*. CRC Press (2001).

7. M.S. Dresselhausand and R. Kalish, Ion Implantation in Diamond, Graphite and Related Materials, Springer-Verlag, Berlin (1992).

8. M. Yu, O. Lourie, M. J. Dyer, T. F. Kelly, R. S. Ruoff, *Science*, 287, 637 (2000).

9. S. Xie, W. Li, Z. Pan, B. Chang, L. Sun, *J Phys Chem Solids*, 61, 1153 (2000).

10. H. Davy, Philosophical Transactions of the Royal Society of London, 104, 557-570, (1814).

11. *I. Herbert, The Diamond Diggers*, Tom Stacey Pub., London (1972).

12. G. Davies, *Diamond*, Adams Hilger Ltd., Bristol, UK (1984).

13. Y. L. Orlov, *The Mineralogy of Diamond*, John Wiley & Sons, New York (1977) .

14. F. P. Bundy, H. M. Strong, and R. H. Wentorf, Jr., *Chemistry and Physics of carbon*, Vol. 10 (P. L., Walker, Jr. and P. A. Thrower, eds.), Marcel Dekker Inc. (1973).

15. D. M. Adams, *Inorganic Solids*, John Wiley & Sons, NewYork (1981).

16. E.Wilks and J. Wilks, Properties and Applications of Diamond (Butterworth Heinemann Ltd., Oxford, 1991).

17. W. G. Eversole, U.S. Patent No. 3,030,188 (1962).

18. J. C. Angus, H. A. Will, W. S. Andstanko, *J. Appl. Phys.,* 39:2915- 2922 (1968).

19. B. V. Spitzyn, L. L. Bouilov, and B. V. Derjaguin, *J. of Crystal Growth,* 52:219-226 (1981).

20. B. V. Derjaguin, and D. V Fedoseev, *Scientific American,*   233(5):   102-109 (1975).

21. B. V. Derjaguin and D. V Fedoseev, *Jzd. Nauka* (in Russian), Ch. 4, Moscow (1977).

22. P.K. Bachmann, in Physics World; Vol.32 (1991).

23. W.L Hsu, *J.Vac.Sci.Technol.*, A(6)3:1803-1811 (1988).

24. J. E. Butler, R. L. Woodin, L. M. Brown and P. Fallon, *Phil. Trans. R. Soc. Lond. A,* 342, 209-224 (1993).

25. K. Spear, *J. Amer. Ceram. Sot.* 7(2):171-91 (1989).

26. DE. Patterson, BJ. Bai, CJ. Chu, RH. Hauge, and JL. Margrave, in New Diamond Science and Technology, eds. Messier RF, Glass JT, Butler JE & Roy R, Materials Research Society, Pittsburgh (1991).

27. M. Yuasa, H. Kawarada, J. Wei, J. Ma, J. Suzuki, S. Okada and A. Hiraki, Surf. Coat. Technol. 49, 374 (1991).

28. H. Liu, DS. Dandy, Diamond Rel. Mater. 4 (1995) 1173.

29. H. Liu, DS. Dandy, Diamond Chemical Vapor Deposition, William Andrew Publishing/Noyes (c)1995.

30. K. V. Ravi, J. *Mater. Res, 7(2):384-393* (1992).

31. B. V. Spitzyn, L. L. Bouilov, and B. V. Derjaguin, .J *Crystal Growth,* 52:219-226 (1981); B. V. Spitzyn, and B. V. Derjaguin, in: *Problems of Physics and Technology of Wide-Gap Semiconductors,* Akad. Nauk SSSR, Leningrad, pp. 22-34 (1979).

32. E. Kondoh, K. Tanaka, and T. Ohta, J. *Appl. Phys., 74(3):2030-2035* (1993)

33. M. P. D'Evelyn, C. J. Chu, R. H. Hange, and J. L. Margrave, J. *Appl.* Phys., 71(3):1528-1530 (1992).

34. C. J. Chu, M. P. D'Evelyn, R. H. Hauge, and J. L. Margrave, J. *Appl. Phys., 70(3):1695-1705* (1991).

35. Z.M.Zhang, H.M.Cheng, S.H.Li,Q.Y.Cai,D.L.Ling, S.J.Wang, Z.W.Hu, S. S. Jiang, C. Z. Ge, and N. B. Ming, J. *Cryst. Growth, 132(1-2):200-204* (1993)

36. S.Katsumata, *Jpn. J. Appl. Phys., 31(11):3594-3597* (1992).

37. M. Komori, T. Maki, T. Kim, G. Hou, Y. Sakaguchi, K. Sakuta, and T. Kobayashi, Appl. Phys. *Lett., 62(6):582-584* (1993).

38. W. A. Yarbrough, J. *Vacuum Sci. Technol. A, 9:1145* (1991).

39. W. P. Chai, Y. S. Gu, M. Li, Z. H. Mai, Q. Z. Li, L. Yuan, and S. J. Pang, J. *Cyst. Growth,* 135(3- 4):639-642 (1994).

40. S. Koizumi, T. Murakami, T. Inuzuka, and K. Suzuki, *Appl. Phys. Lett., 57(6):563-565* (1990).

41. M. Yoshikawa, *Diamond Films and Technol.,* 1:1 (1991).

42. R. A. Bauer, N. M. Sbrockey, and W. E. Brower, Jr, J. *Mater. Res., 8(11):2858-2869* (1993).

43. P. K. Bachmann, W. Drawe, D. Knight, R. Weimer, and R. Messier, in *Diamond and Diamond-like Materials Synthesis, Spring MRS Meeting Extended Abstracts, Symposium D, (M.* W. Geis, G. H. Johnson, and A. R. Badzian, eds.), MRS, Pittsburgh, PA, pp. 99-102 (1988).

44. S. J. Harris, A. M. Weiner, and T. A. Perry, J. *Appl. Phys., 70:1385* (1991).

45. X. Peng, and H. Li, *Mater. Lett., 17(5):223-226* (1993).

46. G. A. Hirata, L. Cota-Araiza, M. Avalos-Borja, M. H. Farias, O. Contreras, and Y. Matsumoto, J. *Phys., 5(33A):A305-306* (1993).

47. J. Singh, J. *Mater. Sci.,* 29(10):2761-2766 (1994).

48. J. Singh, and M. Vellaikal, *Surf. Coat. Technol., 64:131* (1994).

49. D. N. Belton, and S. J. Schmieg, *Thin Solid Films, 212(1-2):68-80* (1992).

50. W. R. L. Lambrecht, C. H. Lee, B. Segall, J. C. Angus, Z. Li, and M. Sunkara, *Nature, 364 (6438):607-610* (1993).

51. A. Baglio, B. C. Farnsworth, S. Hankin, C. Sung, J. Hefter, and M. Tabasky, in *Diamond and Diamond-like Films and Coatings, (R. E. Clausing, L. L. Horton, J. C. Angus, and P. Koidl, eds.), Plenum Press, New York, pp. 635642 (1991).

52. A. R. Badzian, and T. Badzian, *Surf Coat. Technol., 36:283-293* (1988).

53. B. E. Williams, and J. T. Glass, J. *Mater. Res., 4:373* (1989).

54. S. Yugo, T. Kimura, and T. Muto, *Vacuum, 41:1364* (1990).

55. B. E. Williams, J. T. Glass, R. F. Davis, and K. Kobashi, J. *Crystal Growth,* 99:1168 (1990).

56. Y. H. Shing, F. S. Pool, and D. H. Rich, Thin *Solid* Films, 212(1-2):150-155 (1992).

57. S. D. Wolter, J. T. Glass, and B. R. Stoner, J. *Appl. Phys., 77(10):5119 (1995).*

58. A. Lindlbauer, Ph.D. Thesis, TU-Vienna, Austria (1991).

59. B. Lux and R. Haubner, in Diamond and Diamond-like Films and Coatings, eds. RE Clausing, LL Horton, JC Augus and P Koidl, Plenum Press, New York (1991).

60. G. Cowan, B. Dunnington, and A. Holtzman, U.S. Patent 3,401,019 (1968)

61. W. A. Yarbrough, and R. Roy, in *Diamond and Diamond-like Materials Synthesis, Spring MRS Meeting Extended Abstracts, Symposium D, (M. W. Geis, G. H. Johnson, and A. R. Badzian, eds.), MRS, Pittsburgh, PA, 33 (1988).

62. M. Komori, T. Maki, T. Kim, G. Hou, Y. Sakaguchi, K. Sakuta, and T. Kobayashi, Appl. Phys. Lett. 62 582 (1993).

63. K. Kitahama, K. Hirata, H. Nakamatsu, S. Kawai, N. Fujimori, T. Imai, H. Yoshino, and A. Doi, *Appl. Phys. Lett., 49:634* (1986).

64. Y. Shu-Cheng, C. Hon-Sho, and G. Fon-Shu, J. *Cyst. Growth*, 99:1196 (1990).

65. P. Ascarelli, and S. Fontana, *Appl. Surf. Sci., 64(4):307- 311* (1993).

66. P. C. Yang, W. Zhu, and J. T. Glass, J. *Mater. Res, 8(8):1773-1776* (1993).

67. C. M. Niu, G. Tsagaropoulos, J. Baglio, K. Dwight, and A. Wold, J. *Solid State Chemistry*, 91(1):47- 56 (1991).

68. W. A. Yarbrough, and R. Messier, *Science, 247(4943):688-696* (1990).

69. W. A. Yarbrough, in *Applications of Diamond Films and Related Materials, (Y.* Tzeng, M. Yoshikawa, M. Murakawa, and A. Feldman, eds.), Elsevier Science Publishers, Amsterdam, *25-33* (1991).

70. S. Iijima, Y. Aikawa, and K. Baba, J. *Mater. Res., 6(7):1491-1497* (1991).

71. P. A. Dennig, H. Shiomi, D. A. Stevenson, and N. M. Johnson, *Thin Solid* Films, 212(1-2):63-67 (1992).

72. P. A. Dennig, and D. A. Stevenson, *Appl. Phys. Lett, 59(13):1562-1564* (1991).

73. B. R. Stoner, S. R. Sahaida, J. P. Bade, P. Southworth, and P. J. Ellis, J. *Mater. Res., 8(6):1334-1340* (1993).

74. S. D. Wolter, B. R. Stoner, G. H. M. Ma, and J. T. Glass, *(C.* L. Renschler, J. J. Pouch, and D. M. Cox, eds.), Pittsburgh, PA, MRS, 347-352 (1992).

75. B. R. Stoner, B. E. Williams, S. D. Wolter, K. Nishimura, and J. T. Glass, J. *Mater. Res., 7(2):257-260* (1992).

76. R. Csencsits, J. Rankin, R. E. Boekenhauer, M. K. Kundmann, and B. W. Sheldon, *(H.* A. Atwater, E. Chason, M. H. Grabow, and M. G. Lagally, eds.), Pittsburgh, PA, MRS, 695-700 (1993).

77. M. Katoh, M. Aoki, and H. Kawarada, *Jpn. J. Appl. Phys.,* 33(2A):L194-L196 (1994)

78. *S.* Yugo, T. Kanai, T. Kimura, and T. Muto, *Appl.* Phys. Lett., 58(10): 1036-1038 (1991).

79. T. Hartnett, R. Miller, D. Montanari, C. Willingham, and R. Tustison, J. *Vac. Sci. Technol. A,* 8:2129 (1990).

80. R Locher, C Wild, W Muller-Serbert, R Kohl and P Koidl, Diamond Rel. Mater. 2, 1248 (1993).

81. CF Chen, 1st Int. Conf. Diamond Sci. and Technol, Oct. 24-26, Tokyo, 118 (1988).

82. HC Shih, CP Sung and WL Wan, Surf. Coat. Technol. 54-55 380(1992).

83. DM Gruen, Annu. Rev. Mater. Sci. 29 211 (1999).

84. A.T. Collins, in *Properties and Growth of Diamond* Ed. G. Davies (INSPEC, IEE, London, UK, 1994) ch.9 p.261-88.

85. R.H. Wentorf and H.P. Bovenkerk, J. Chem. Phys. 36, 1987 (1959).

86. H. Okushi, Diamond and Related Materials, Volume 10, Issues 3-7, Pages 281-288 (2001).

87. T H Borst and O Weiss, *Physica Status Solidi*, A 154, 423 (1996).

88. M.W.Geis and J.C. Angus, Scientific American, 64 (1992).

89. R.E. Harper, C. Johnston, N.G. Blamires, P.R. Chalker, LM. Buckley-Golder, *Surf. Coat. Technol.* vol.47, p.344 (1991).

90. X.K. Zhang, J.G. Guo, Y.F. Yao, R. Wang, G.M. Chen, W.K. Zhou, S. Yu, Appl. Phys. A56, 425-428 (1993).

91. X.K. Zhang et al, *Appl. Phys. A (Germany)* vol.56 p.425 (1993).

92. N.Fujimori, Jpn. J. Appl. Phys. 29, 824 (1990).

93. K.Nishimura, K.Das and J.T. Glass, Appl. Phys. Lett. 69, 3142 (1991).

94. G.L. Pearson, J. Bardeen, *Phys. Rev. (USA)* vol.75 p.865 (1949).

95. J.-P. Lagrange, A. Deneuville, E. Gheeraert, Diamond and Related Materials 7 1390–1393 (1998).

96. S. A. Kajihara, A. Antonelli, J. Bernholc and R. Car: Phys. Rev. Lett. 66 2010 (1991).

97. H Sternschulte, K Thonke, R Sauer, S Koizumi, *Phys. Rec.   B. 59*, 12924-7 (1999).

98. S Koizumi, M Kamo, Y Sato, H Ozaki, T Inuzuka, *Appl. Phys. Lett.* 71**,**1065-7 (1997).

99. S Bohr, R Haubner, B Lux. *Diamond Relat. Mater.* 4, 13344 (1995).

100. T Saito, M Kameta, K Kusakabe, S Morooka, H Maeda, Y Hayashi, T Asano. *Jpn. J. Appl. Phys., Part 2: Lett. 31***,** L543-6 (1998).

101. J.F Prins., Physica B, 185 132 (1993).

102. R. Kalish, C Uzan-Saguy, A. Samoiloff, R. Locher, P. Koidl., *Appl. Phys. Lett.* vol.64 p.2532-4 (1994).

103. R. Kalish, C Uzan-Saguy, B. Ran, H. Ferber, H. Guettler, R. Zachai., *Diam. Relat. Mater.* 7, 877-81 (1999).

104. F. Maier, J. Ristein, and L. Ley, Phys. Rev. B 64, 165411 (2001).

105. F. Maier, M. Riedel, B. Mantel, J. Ristein, and L. Ley, Phys. Rev. Lett. 85, 3472 (2000).

106. R. I. S. Gi, T. Mizumasa, Y. Akiba, H. Hirose, T. Kurosu, and M. Iida, Jpn. J. Appl. Phys. 34, 5550 (1995).

107. T. Maki, S. Shikama, M. Komori, Y. Sakaguchi, K. Sakuta, and T. Kobayashi, Jpn. J. Appl. Phys. 31, 1446 (1992).

108. K. Hayashi, S. Yamanaka, H. Okushi, and K. Kajimura, Appl. Phys. Lett. 68, 376 (1996).

109. H. J. Looi, R. B. Jackman, and J. S. Foord, Appl. Phys. Lett. 72, 353 (1998).

110. R. I. S. Gi, K. Tashiro, S. Tanaka, T. Fujisawa, H. Kimura, T. Kurosu, and M. Iida, Jpn. J. Appl. Phys. 38, 3492 (1999).

111. J. Shirafuji and T. Sugino, Diam. Relat. Mater. 5, 706 (1996).

112. C. E. Nebel, B. Rezek, D. Shin, and H. Watanabe, phys. stat. sol. (a) 203, 13, 3273 – 3298 (2006).

113. H.O Pierson., Handbook of Chemical Vapor Deposition (CVD) -Principles, Technology and Applications (2nd Edition) (1999) William Andrew Publishing/Noyes.

114. M. Seal, *Applications of Diamond Films and Related Materials, (Y.* Tzeng, et al., eds.), 3-7, Elsevier Science Publishers (1991)

115. R. C, Eden., *Applications of Diamond Films and Related Materials, (Y.* Tzeng, et al., eds.), 259-266, Elsevier Science Publishers (1991).

116. D. S Hoover, S.- Y Lynn, and D Garg, *Solid State Technology,* 89-91 (1991).

117. D. C. Harris, SPIE Press. 303–334 (1999).

118. G. S. Nusinovich. *Introduction to the physics of gyrotrons.* JHU Press. 229 (2004).

119. E. Woerner, C. Wild, W. Mueller-Sebert, P. Koidl, Diamond and Related Materials, 10, 3-7, 557-560 (2001).

120. D. D. Jackson., *Rev. Sci. Instrum.* 74: 2467 (2003).

121. N. Fujimori, New *Diamond, 2(2):10-15* (1988).

122. A. Vescan, I. Daumiller, P. Gluche and W. Ebert, *Diamond Relat. Mater.* 7, 581 (1998).

123. A. Aleksov, A. Denisenko, M. Kunze, A. Vescan, A. Bergmaier, G. Dollinger, W. Ebert and E. Kohn, *Semicond. Sci. Technol.* 18, S59-S66 (2003).

124. A. Aleksov, A. Denisenko and E. Kohn, *Solid-State Electron* 44, 369–375 (2000).

125. A. Aleksov, A. Vescan, M. Kunze, P. Gluche, W. Ebert, E. Kohn, A. Bergmaier and G. Dollinger , *Diam. Relat. Mater.* 8, 942 (1999).

126. K.Tsugawa, H.Umezawa, and H Kawarada, Jpn. J. Appl. Phys. Part 1 – Regul. Pap. Short Notes Rev. Pap. 40, 3101 (2001).

127. H.Umezawa, T. Arima, N. Fujihara, H. Taniuchi, H. Ishizaka, C. Wild, P. Koidl and H. Kawarada, Jpn. J. Appl. Phys. Part 1 – Regul. Pap. Short Notes Rev. Pap. 41, 2611 (2002).

128. R.B. Jackman, in Low-Pressure Synthetic Diamond Manufacturing and Applications, eds. Dischler B and Wild C, Springer-Verlag, Berlin (1998).

129. M Bevilacqua and R. B. Jackman, Appl. Phys. Lett. 95, 243501 (2009).

130. J. Kaneko and M.Katagiri, Nuclear Instruments and Methods in Physics Research Section A: Accelerators, Spectrometers, Detectors and Associated Equipment 383, 547 (1996).

131. C. Manfredotti, F.Fizzotti, E.Vittone, S. Bistolfi, M. Boero, and P. Polesello, Nuclear Instruments and Methods in Physics Research B 93, 516 (1994).

132. H. B. Martin, A. Argoitia, J. C. Angus, A. B. Anderson and U. Landau *Applications of Diamond Films and Related Materials: Third International Conference*, NIST Special Publication 885, Eds Feldman A *et al.* U.S. Dept of Commerce 91-4 (1995).

133. T. Ponnuswamy, J. Chen, X. Fei, and O Chyan, *Analyst,* 126 877-80 (2001).

134. P. L. Hagans, P. M. Natishan, B. R. Stoner and W. E. O'Grady, *J. Electrochem. Soc.* 148 E298 (2001).

135. W. Haenni, P. Rychen, M. Frydaand, C. Comninellis, *Thin-Film Diamond II* eds C E Nebel and J Ristein (Amsterdam: Elsevier) pp 149-196 (2004).

Chapter 3: Conduction theory

3.1: Carrier mobility in semiconductors

3.2: High field effects

3.3: Quantum tunneling

3.1 Carrier mobility in semiconductors

Consider a n-type semiconductor sample with a uniform donor concentration in thermal equilibrium. The conduction electrons in the semiconductor conduction band are essentially free particles, since they are not associated with any particular lattice or donor site. The influence of the crystal lattice is incorporated in the effective mass of conduction electrons, which differs somewhat from the mass of free electrons. Under thermal equilibrium, the average thermal energy of a conduction electron can be obtained from the theorem for equipartition of energy: 1/2 kT units of energy per degree of freedom, where k is Boltzmann's constant and T is the absolute temperature (3.1). Electrons in a semiconductor have three degrees of freedom; they can move about in a three-dimensional space. Therefore the kinetic energy of the electrons is given by

$$\frac{1}{2} m_n v_{th}{}^2 = \frac{3}{2} kT$$

(3.1)

where m_n is the effective mass of electrons and v_{th} is the average thermal velocity.

The electrons in a semiconductor are therefore moving rapidly in all directions. The thermal motion of an individual electron may be visualised as a succession of random scattering collisions with lattice atoms, impurity atoms and other scattering mechanisms (image). The random motion of

electrons leads to a zero displacement of an electron over a sufficiently large period of time. The average distance between collisions is called the *mean free path*, and the average time between collisions is called the *mean free time* τ_c. For a typical value of 10^{-5} cm for the mean free path, τ_c is about 1ps (i.e., $10^{-5}/v_{th} \sim 10^{-12}$ s).

When a small electric field E is applied to a semiconductor sample, each electron will experience a force –qE from the field and will be accelerated along the field (in the opposite direction to the field) during the time between collisions. Therefore, an additional velocity component will be superimposed upon the thermal motion of electrons. This additional component is called the *drift velocity*. The combined displacement of an electron due to the random thermal motion and the drift component is illustrated in figure 3.1. Note that there is a net displacement of the electron in the direction opposite to the applied field.

E=0   E

(a)   (b)
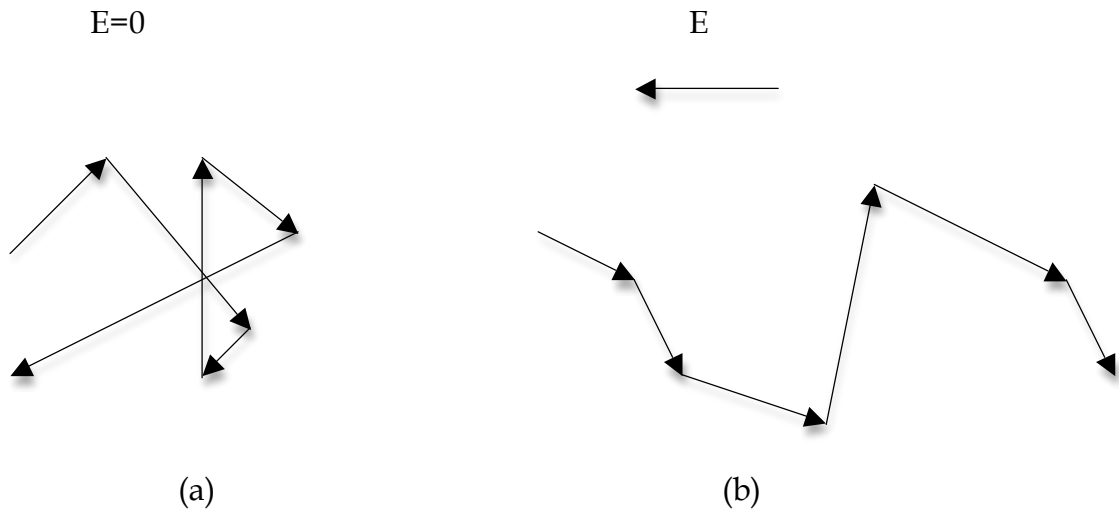
Figure 3.1: Schematic path of an electron in a semiconductor. (a) Random thermal motion. (b) Combined motion due to random thermal motion and an applied electric field (from [1]).

We can obtain the drift velocity v_n by equating the momentum (force x time) applied to an electron during the free flight between collisions to the momentum gained by the electron in the same period. The equality is valid because in a steady state all momentum gained between collisions is lost to the lattice in the collision. The momentum applied to the electron is given by $-qE\tau_c$, and the momentum is $m_v v_n$. We have

$$-qE\tau_c = m_n v_n \tag{3.2}$$

or

$$v_n = [{}^{q\tau_c}\!/\!_{m_n}]E \tag{3.3}$$

Equation 3.3 states that the electron drift velocity is proportional to the applied electric field. The proportionality factor depends on the mean free time and the effective mass. The proportionality factor is called the *electron mobility* u_n (or *hole mobility* u_p) in the units of cm^2/Vs, or

$$\mu_{n,p} \equiv \frac{q\tau_c}{m_{n,p}} \tag{3.4}$$

Thus,

$$V_{n,p} = (-)\mu_{(n),p}E \tag{3.5}$$

Mobility is an important parameter for carrier transport because it describes how strongly the motion of an electron or hole is influenced by an applied electric field. In chapters 5,6 and 7 in this thesis carrier mobility is an important topic of discussion.

3.1.1 Scattering mechanisms

In equation 3.4 the mobility is related directly to the mean free time between collisions, which in turn is determined by the various scattering mechanisms. The two most important mechanisms are lattice scattering and impurity scattering. Lattice scattering results from thermal vibrations of the lattice at any temperature above absolute zero. The agitation of the atoms produces variations in the periodic potential of the lattice resulting in the emission of phonons that transfer energy between the lattice and the free carriers. Lattice scattering becomes dominant at higher temperatures because lattice vibrations increase with increasing temperature. Mobility due to lattice scattering varies as $T^{-3/2}$. Impurity scattering results when a charge carrier travels past an ionized dopant impurity (donor or acceptor). The charge carrier path will be deflected due to Coulomb force interaction. The probability of impurity scattering depends on the total concentration of ionized impurities, that is, the sum of the concentration of negatively and positively charged ions. However, unlike lattice scattering, impurity scattering becomes less significant at higher temperatures. At higher temperatures, the carriers move faster; they remain near the impurity atom for a shorter time and are therefore less effectively scattered. The impurity scattering μ_I can be theoretically shown to vary as $T^{3/2}/N_T$, where N_T is the total impurity concentration.
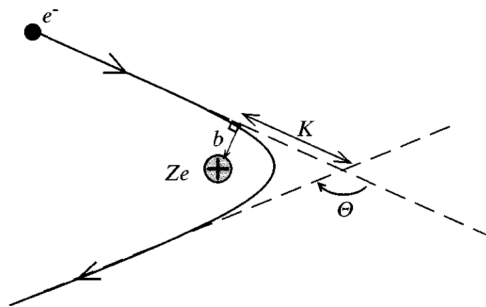
Figure 3.2: Coloumb scattering of an electron by a positively charged ion (from [2]).

In this approach an electron is assumed to be scattered classically via Coulomb interaction by an impurity ion with charge +*Ze.* The corresponding scattering cross section is calculated in exactly the same way as for the Rutherford scattering of α particles [3]. The scattering geometry of this problem is shown schematically in figure 3.2. The *scattering cross section* σ as a function of the scattering angle Θ is given by

$$\sigma(\Theta)d\Omega = 2\pi b d|b| \tag{3.6}$$

Where $d\Omega$ is an element of solid angle, b is known as the impact parameter, and $d|b|$ is the change in $|b|$ required to cover the solid angle $d\Omega$. The impact parameter and the solid angle $d\Omega$ are related to the scattering angle by

$$b = K\cos(\Theta/2); \quad d\Omega = 2\pi\Theta d\Theta \tag{3.7}$$

where K is a characteristic distance defined by

$$K = \frac{Z_e^{\,2}}{mv_k^{\,2}} \tag{3.8}$$

and V_k is the velocity of an electron with energy $E_k = mv_k^2$. If $d\Omega$ and $d|b|$ are expressed in terms of $d\Theta$, (3.6) can be simplified to

$$\sigma(\Theta) = \left[K/2\sin^2(\Theta/2)\right]^2 \tag{3.9}$$

Equations 3.6-3.9 are found in [4].
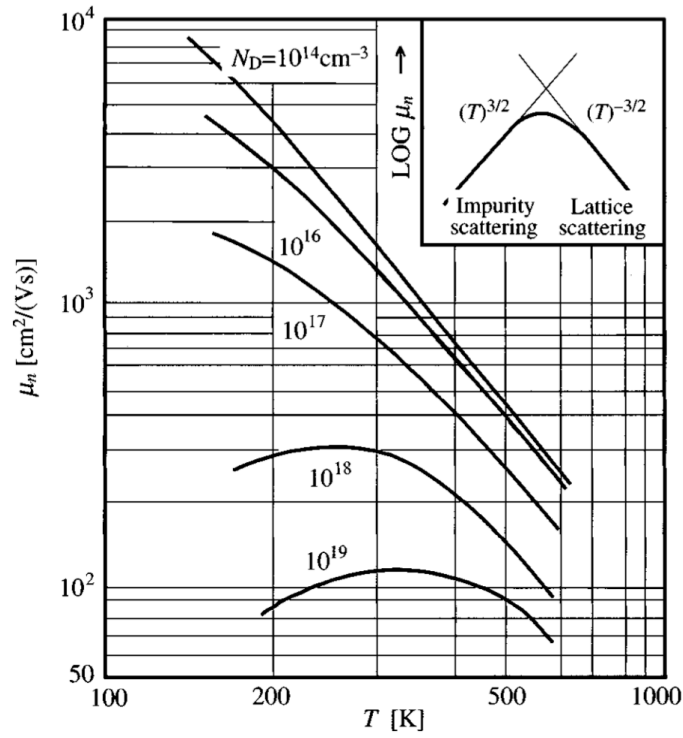
Figure 3.3: Temperature dependence of mobilities in n-type Si for a series of samples with different electron concentrations. The inset sketches the classical temperature dependence due to lattice and impurity scattering (from [1]).

The combined mobility which includes the two mechanisms above, is

$$\mu = \left(1/\mu_l + 1/\mu_i\right)^{-1}$$

(3.10)

where μ_l is the mobility from phonon interaction, and μ_i is the mobility from ionized impurity interaction [1].

3.2 High field Effects

At low electric fields, the drift velocity is linearly proportional to the applied field. We assume that the time interval between collision, τ_c , is independent of the applied field. This is a reasonable assumption as long as the drift velocity is small compared to the thermal velocity of carriers. As the drift velocity approaches the thermal velocity, its field dependence on the electric field will begin to depart from the linear relationship, and in some cases saturation of the *drift velocity* is observed. At still larger fields impact ionization occurs. First we consider the nonlinear mobility. At thermal equilibrium the carriers emit both and absorb phonons, and the net rate of exchange of energy is zero. The energy distribution at thermal equilibrium is Maxwellian. In the presence of an electric field the carriers acquire energy from the electric field and lose it to phonons by emitting more phonons that are absorbed.

In the case of diamond and other semiconductors at fields less than 10^3 V/cm [1] the current density J_x is proportional to the electric field (eqn 3.11).

$$J_x = \sigma E_x, \quad \text{where} \quad \sigma \equiv \frac{nq^2\tau_c}{m_n} \tag{3.11}$$

where n is the number of electrons, and m_n is the mass of an electron.

At reasonably high fields the most frequent scattering event is the emission of optical phonons. The carriers thus, on average acquire more energy than they have at thermal equilibrium. As the field further increases, the average energy of the carriers also increases, and they acquire an effective temperature T_e that is higher that the lattice temperature T. Equation 3.11 is no longer valid under these conditions.

When the electric field in a semiconductor is increased above a certain value, the carriers can gain enough energy so that they can excite electron-hole pairs by impact ionization. The electron-hole generation rate G is given by

$$G = \alpha_n n v_n + \alpha_p p v_p \tag{3.12}$$

where α_n is the ionization rate defined as the number of electron-hole pairs generated by an electron per unit distance travelled. Similarly, α_p is the analogously defined ionization rate for holes. Both α_n and α_p are strongly dependent on the electric field.

A physical expression for the ionization rate is given by

$$\alpha(E) = (qE/E_I)\exp\{-E_I/[E(1+E/E_p)+E_{kt}]\}$$

$$\tag{3.13}$$

where E_I is the high field, effective ionization threshold energy, and E_{kt}, E_p, and E_I are thresholds fields for carriers to overcome the decelerating effects of thermal, optical-phonon and ionization scattering, respectively. Equations 3.11-3.13 are found in [1].

3.3 Quantum tunneling

Quantum tunneling refers to the quantum mechanical phenomenon where a particle "passes through" some sort of barrier that has a higher energy than the particle. It is well known that for one-dimensional barrier height U_0 and thickness W, the quantum-mechanical transmission probability is given T_t.

When $E < U_0$

$$T_t = \left[1 + \frac{E_0{}^2 \sinh^2 kW}{4E(U_0 - E)} \right]^{-1} \tag{3.14}$$

where $\quad k \equiv \sqrt{\dfrac{2m(U_0 - E)}{\hbar^2}} \tag{3.15}$

where $\hbar$ is Planck's constant divided by 2π, m is the particle mass, W is the thickness of the barrier measured in the direction of motion of the particle (classically forbidden region, fig. 3.4), U_0 is the barrier height, E is the energy of the carrier .

The probability decreases monotonically with decreasing E. When kW>>1, the probability becomes

$$T_t \approx \frac{16E(U_0 - E)}{E_0{}^2} \exp(-2kW) \tag{3.16}$$

Tunneling is important only over very small dimensions but it can be of great importance in the conduction of electrons and holes in solids, for example hopping conductivity relies on the quantum mechanical tunneling of carriers. In chapters 5,6 and 7 of this thesis hopping conductivity is an important topic of discussion. Equations 3.14-3.16 can be found in [1].
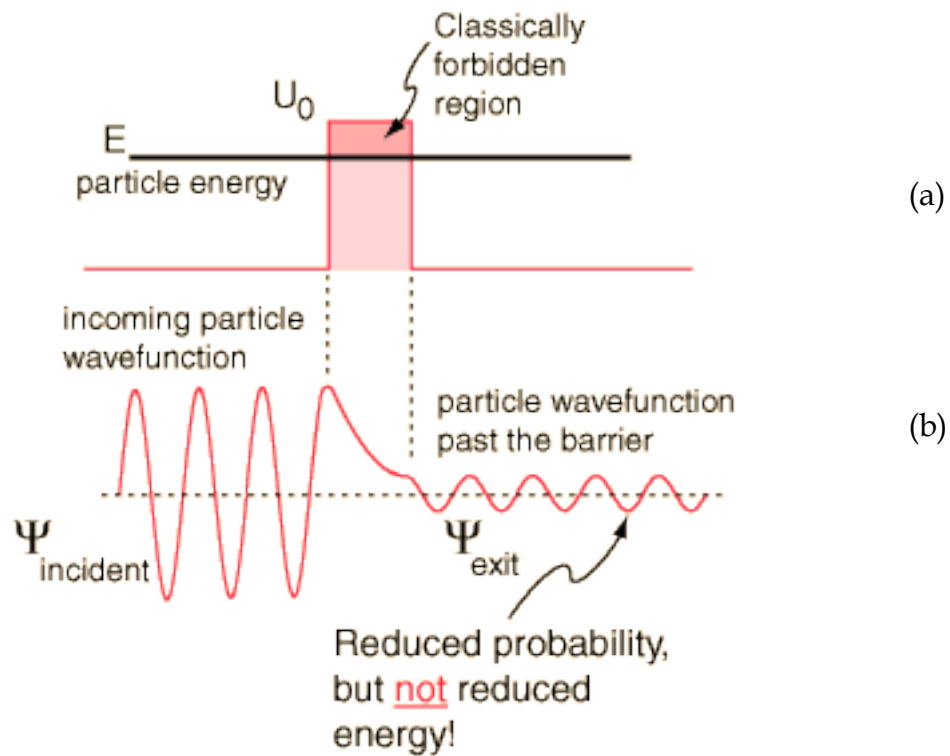
Figure 3.4: Quantum mechanical tunneling: (a) potential barrier of height U_0 (b) probability density for an electron with energy $E<U_0$, indicating a nonzero value of the wave function beyond the barrier (from [5]).

3.4 References

1. S. M. Sze, Physics of Semiconductor devices (2nd Edition). Wiley-New York publication (1985).

2. B. K. Ridley: *Quantum Processes in Semiconductors*, 2nd edn. (Clarendon, Oxford 1988)

3. R. L. Liboff: *Quantum Mechanics* (Addison-Wesley, Reading, MA 1980) p. 625.

4. Yu, Peter Y.; Cardona, Manuel Fundamentals of Semiconductors - Physics and Materials Properties (3rd Edition).. Springer – Verlag (2001).

5. B. G. Streetman and S.Banerjee, Solid State Electronic Devices (5th Edition). Prentice Hall (2000).

Chapter 4: Experimental Methods

4.1: Surface cleaning and preparation

4.2: Resistive deposition of metal contacts

4.3: Hall effect technique

4.4: Van der Pauw method

4.5: Impedance spectroscopy

4.6: Scanning electron microscopy

4.7: Scanning tunneling microscopy

4.8: Raman spectroscopy

4.9: Energy-dispersive X-ray spectroscopy

4.10: Glow-discharge technique

4.11: References

4.1 Surface cleaning and preparation

The surface cleaning process used for the cleaning of samples throughout this thesis was developed at UCL in 1994 [1]. The initial purpose of the process is to remove any other non-diamond carbon (such as DLC and graphite) from the surface of the diamond that would act as a barrier to device fabrication. This treatment consists of two processes: (1) a degrease and (2) an acid bath. The material is subjected to a degrease, then an acid bath and another degrease. Both processes are to be carried out in a fume cupboard.

Degrease solvents: 1,1,1-trichloroethane

                Acetone

                2-propanol (isopropanol, IPA)

                De-ionized water (DI)

Degrease procedures:

1)   Heat sample in 1,1,1-trichloroethane at 60°C for 5 minutes – do not allow to boil.

2) Transfer sample to acetone at room temperature.

3) Transfer sample to 2-propanol at room temperature.

4) Transfer sample to de-ionized water at room temperature.

5) Blow-dry with nitrogen.

When transferring samples between solvents it is important to prevent the solvent on the sample from drying out as residue on the sample surface, which is insoluble in the following solvent.

Acid bath solvents: Concentrated sulphuric acid (c-H_2SO_4)

Ammonium persulphate ((NH_4)$_2S_2O_8$)

Hydrogen peroxide (H_2O_2)

Ammonium hydroxide (NH_4OH)

De-ionized Water (DI)

Acid bath procedure:

1) Place 30 grams of ammonium persulphate in a beaker. Carefully add 30 ml of concentrated sulphuric acid. This will give the ETCH solution.

2) Prepare the RINSE solution consisting of a 1:1 mixture of hydrogen peroxide (10ml) and ammonium hydroxide (10ml).

3) Heat the ETCH solution and add the diamond samples when the temperature is about 85°C. It may fizz slightly.

4) Continue heating. Above 140°C fumes of SO_3 will be released.

5) Maintain the temperature of the solution at about 200°C for 20 minutes.

6) Allow the solution to cool to about 50°C before carefully transferring the sample from the ETCH solution to the RINSE solution. Pay attention, as there will be some heavy fizzing as the acid is neutralized.

7)   Heat the RINSE solution and sample to about 50°C for 10 minutes.

8)   Dispose of the ETCH solution by infinite dilution in running water.

9)   Transfer sample from the RINSE solution to de-ionized water.

10) Dispose of the RINSE solution by infinite dilution in running water.

11) Remove sample from DI water and blow dry with nitrogen.

This cleaning recipe developed at UCL included an Auger electron spectroscopic study of various reported treatments [1], based on a selection of literature [2-6]. It was concluded that exposing CVD polycrystalline diamond to hydrogen plasma at the termination of the growth run or the use of strongly oxidizing solutions are both capable of removing non-diamond carbon from the surface. Both the oxidizing solutions considered gave rise to low concentrations of sulphur within the surface region and produced some form of oxide phase, but the sulphuric acid-ammonium persulphate etchant solution gave a carbon KVV Auger electron spectrum which more closely resembled single crystalline diamond. Hence this solution is used here.

4.2 Resistive deposition of metal contacts

Metal contacts can be deposited using a variety of techniques such as resistive evaporation, flash evaporation, sputtering and electron evaporation. Resistive evaporation will be described in detail in this section as it is the main method for depositing thin metal films for most of the experimental work in this thesis. Evaporation is conducted by passing a current through a highly resistive wire, filament or boat. The heat generated by the resistive element is used to melt and vaporize the metal required. The highly resistive element is normally made from refractory metals such as tungsten and molybdenum that have very high melting points of 3380°C and 2610°C at atmospheric pressure. It is preferable that the metal sublimes, as this avoids interaction of the metal liquid phase with the filament or heating elements. Some metals (for example titanium) form alloys with tungsten at high

temperatures and this normally leads to the destruction of the filament during evaporation. A high vacuum ($<10^{-6}$ mbar) is necessary to minimize the contamination, prevent the rapid oxidation of the metallic vapour and lower the vaporization temperature. Aluminium, gold, silver, tin, nickel and chromium can be easily deposited by this method. The key advantage of vacuum evaporation is the very high deposition rate achievable so that thick metal films (500nm) can be formed. This method, however, requires line of sight from the source to the target, as a result complex and irregular shape samples may not be uniformly coated.

The resistive evaporation system used for the deposition of Au films in this thesis is an Edwards 306. The base pressure during the evaporation is kept below 10^{-6}mbar. This pressure is achieved by a diffusion pump backed by a rotary pump. A liquid nitrogen cold trap is used in addition to removed unwanted contamination from the diffusion pump and to maintain low pressure during resistive heating itself. Au evaporation is performed using a molybdenum boat.

4.3 Hall effect technique

The Hall effect was discovered in 1874, by E. H. Hall and can be used to measure the mobility, carrier density and the sign of the charge carriers.
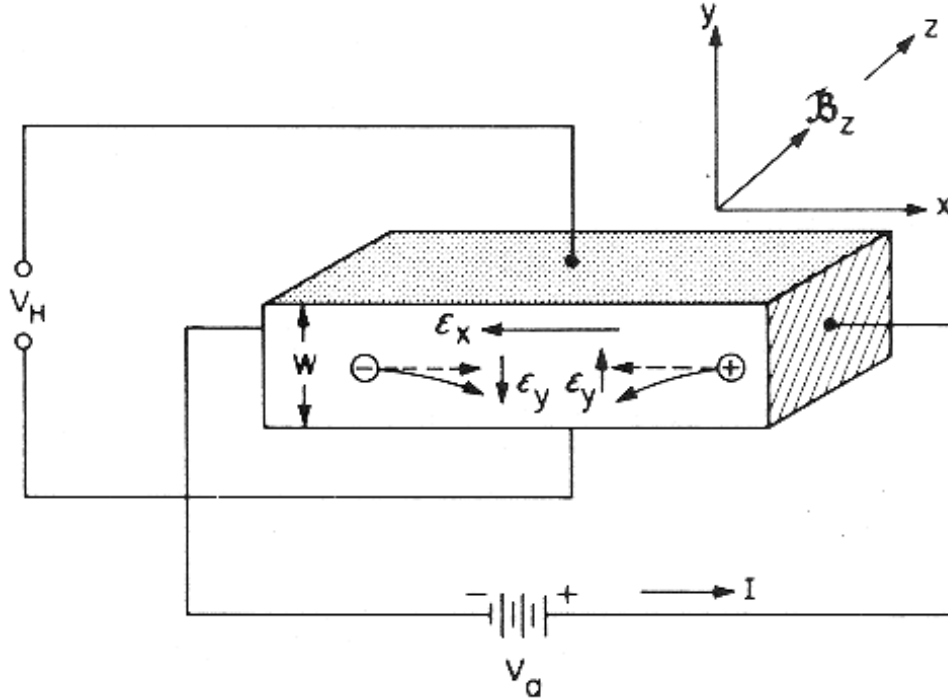
Figure 4.1: Hall effect with p-type sample (from [7]).

An electric field E_x is applied along the x-axis, and a magnetic field B_z is applied along the z-axis. Holes in the sample are subject to a Lorentz force ev_x x B_z along the y-axis. This force will cause holes to gather at the bottom of the sample, which in turn will create an electric field E_y along the y-axis. Under steady state conditions, there is no net current in the y direction. Therefore, the Lorentz force on the y-axis and the created electric field on the y-axis must balance each other. This electric field E_y is called the Hall field or Hall voltage. Provided that one type of carrier dominates, the carrier concentration can be calculated based on the measured electric field, the applied magnetic field, and current density along the x-axis [7].

For a simple metal or semiconductor where there is only one type of charge carrier the Hall voltage (V_H) is given by:

$$V_H = IB/dne \qquad (4.1)$$

where I is the current across the plate length, B is the magnetic flux density, d is the depth of the plate, e is the electron charge, and n is the charge carrier density of the carrier electrons.

From the above expression the density n of free carriers can be determined and from the sign of the Hall voltage, also the type of carrier can be identified.

The Hall mobility μ_H of the carriers can be determined from equation (4.2) provided the resistivity ρ is known.

$$\mu_H = 1/(ne\rho) \qquad (4.3)$$

Equation 4.3 holds only under the assumption of energy independent scattering mechanisms otherwise the Hall mobility has to be modified by a factor A, the Hall scattering factor. This factor depends on the scattering mechanisms in the semiconductor and generally lies between 1 and 2. It is also a function of the magnetic field and temperature. Hence taking into account the scattering factor A, the Hall mobility becomes:

$$\mu_H = A\,\mu_p \qquad (4.4)$$

where μ_H is the Hall mobility and μ_p is the conductivity mobility for holes. Conductivity mobilities can therefore differ significantly from measured Hall mobilities. However the factor A in this work was taken as unity as the scattering mechanisms in diamond are not clearly identified.

4.4 Van der Pauw method

For the determination of sheet resistivity or ρ of a sample the four probe Van der pauw method is commonly used due to its simplicity.
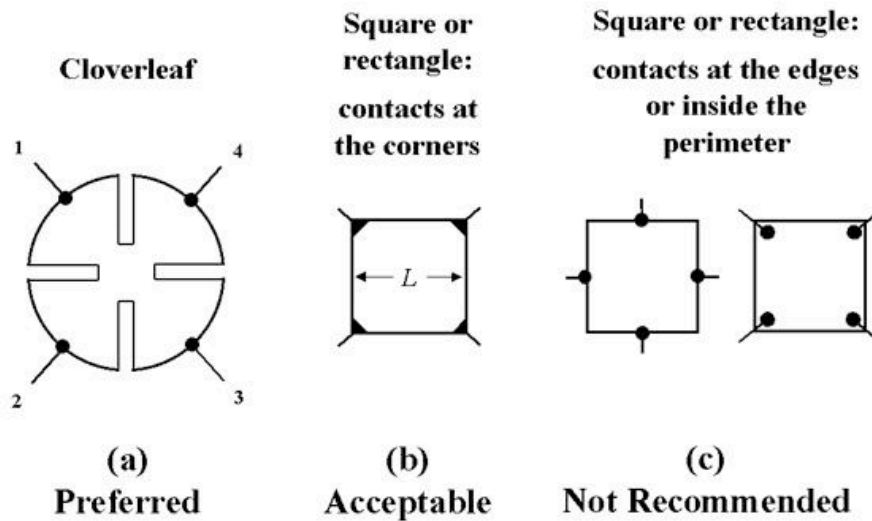
Figure 4.2: Electrical contact configurations for possible Van der Pauw measurements.

In order to use the Van der Pauw method, the sample thickness must be much less than the width and length of the sample. In order to reduce errors in the calculations, it is preferable that the sample is symmetrical.

The measurement requires that four ohmic contacts be placed on the sample. Certain conditions for their placement need to be met:

- They must be on the boundary of the sample.
- They must be infinitely small. Practically, they must be as small as possible; any errors given by their non-zero size will be of the order D / L, where D is the average diameter of the contact and L is the distance between the contacts.

Measurement definitions:

- The contacts are numbered from 1 to 4 in a counter-clockwise order, beginning at the top-left contact.
- The current I_{12} is a positive DC current injected into contact 1 and taken out of contact 2, and is measured in amperes (A).
- The voltage V_{34} is a DC voltage measured between contacts 3 and 4 with no externally applied magnetic field, measured in volts (V).
- The sheet resistance R_S is measured in ohms (Ω/sq).

Measuring

To make a measurement, a current is caused to flow along one edge of the sample (for instance, I_{12}) and the voltage across the opposite edge (in this case, V_{34}) is measured [8]. From these two values, a resistance (for this example, $R_{12,34}$) can be found using Ohm's law:

$$R_{12,34} = \frac{V_{34}}{I_{12}}$$

(4.5)

Further improvements in the accuracy of this measurement can be implemented by measuring $R_{23,41}$, $R_{34,12}$ and $R_{41,23}$.

$$R_{vertical} = \frac{R_{21,34} + R_{34,12} + R_{21,43} + R_{43,21}}{4}$$

(4.6)

and

$$R_{horizontal} = \frac{R_{23,41} + R_{41,23} + R_{32,14} + R_{14,32}}{4}$$

(4.7)

Sheet resistivity (Ohm/sq) or ρ is given by (assuming R $_{vertical}$ = R $_{Horizontal}$)

$$R_s = \frac{\pi R}{\ln 2}$$

(4.8)

4.5 Impedance spectroscopy

Impedance spectroscopy is a powerful technique used to characterize the electrical properties of materials and their interfaces with electrically conducting electrodes. The technique may be used to investigate the dynamics of bound or mobile charges in bulk or interface regions of any kind of ionic solids, or liquid materials, semiconductors, mixed ionic-electronic materials and insulators (dielectrics). The technique measures the impedance as a function of frequency automatically in the range of 0.1 Hz to 10 MHz and is easily interfaced to the computer. The technique has been comprehensively reviewed in reference [9].

This technique allows for the separation of the complex impedance measurements from contributions such as bulk, grain boundary and electrode, to total conductivity. Hence this technique is able to extract the data that allow these phenomena to be isolated. This chapter provides detailed background information based on both theoretical and empirical knowledge of this technique.

Impedance spectroscopy is usually performed by applying an AC potential of *V (t)= A sin (ωt)*, for a single frequency *ω/2π*, and measuring the current *I= A sin (ωt+φ)* through the sample of where *φ* is the phase difference between the voltage and current; it is zero for purely resistive behaviour.

A= maximum amplitude, *ω=*Frequency in radians/sec, *f=* frequency in Hz and *φ=* Phase shift in radians.

Electrochemical impedance is the frequency-dependent complex valued proportionality factor, which is a ratio between the applied potential and current signal. The objective of impedance experiments is to determine the values of the various elements in the equivalent circuit or simply to confirm that a given electrochemical system fits a particular equivalent circuit model. In this thesis the basic modelling unit is comprised of a single resistance-capacitance (R-C) parallel circuit. The reason for choosing this circuit is because many of the electrochemical systems encountered in practise are actually modelled using this configuration [9].

(a)

(b)
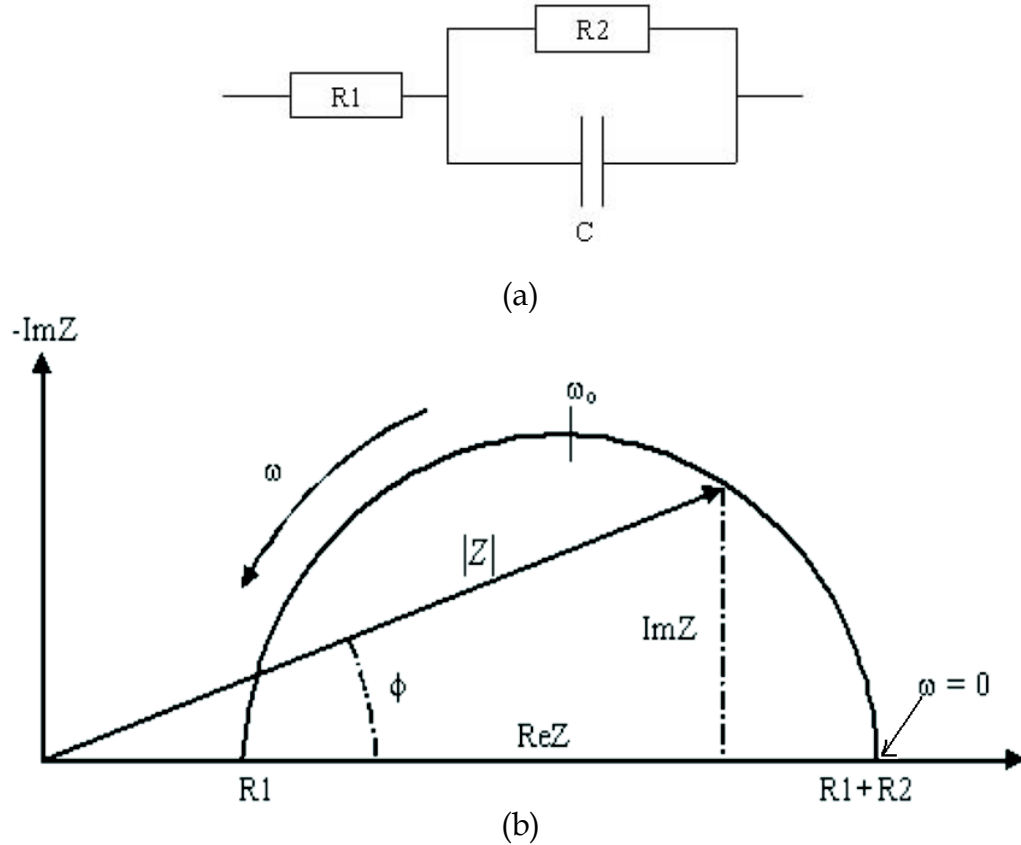
High frequency: $Z'' \Rightarrow 0$, $Z' \Rightarrow R_1$
$\omega = 0$: $Z'' \Rightarrow 0$, $Z' \Rightarrow R_1 + R_2$

Figure 4.3: Equivalent circuit and AC impedance plots of an electrochemical cell with one time constant: (a) Equivalent circuit, (b) Cole-Cole plot in the complex plane, $\omega_0 = 1/(R_2 C)$.

The impedance $Z(\omega)$ is a complex number which can be represented either in polar co-ordinates or in Cartesian co-ordinates:

$$Z(\omega) = |Z|e^{j\phi} \tag{4.9}$$

$$Z(\omega) = ReZ + j\ ImZ \tag{4.10}$$

where ReZ and ImZ are the real part and the imaginary part of the impedance, respectively. The relationships between theses quantities are:

$$|Z|^2 = (\mathrm{Re}\,Z)^2 + (\mathrm{Im}\,Z)^2 \tag{4.11}$$

$$\phi = Arc\ tan\ \frac{\mathrm{Im}\,Z}{\mathrm{Re}\,Z} \tag{4.12}$$

$$\mathrm{Re}\,Z = |Z|\cos\phi \tag{4.13}$$

$$\mathrm{Im}\,Z = |Z|\sin\phi \tag{4.14}$$

In figure 4.3 (a) the equivalent circuit of an electrochemical interface is depicted, its impedance is:

$$Z(\omega) = \frac{E}{I} = R_1 + \frac{1}{\dfrac{1}{R_2} + jC\omega} = R_1 + \frac{R_2}{1 + \omega^2 C^2 R_2^2} - \frac{j\omega C R_2^2}{1 + \omega^2 C^2 R_2^2} \tag{4.15}$$

E is the voltage

I is the current

R_1 and R_2 are the resistance values of the equivalent circuit

C is the capacitance value of the equivalent circuit

Furthermore,

$$|Z(\omega)| = \sqrt{(R_1 + \frac{R_2}{1 + \omega^2 C^2 R_2^2})^2 + (\frac{\omega C R_2^2}{1 + \omega^2 C^2 R_2^2})^2} \qquad (4.16)$$

when ω tends to zero, $|Z(\omega)|$ equals $R_1 + R_2$

when ω tends to infinite, $|Z(\omega)|$ equals R_1

This gives rise to semicircular shaped Cole-Cole plots, which correspond to the equation as follows:

$$\left[Z' - (R_1 + \frac{R_2}{2})\right]^2 + Z''^2 = (\frac{R_2}{2})^2 \qquad (4.17)$$

It has been shown that equation (4.17) is analogous to the equation of a circle, with a radius of $\frac{R_2}{2}$ and a centre at $(R_1 + \frac{R_2}{2}, 0)$. In all the materials studied, ω, R_1 and R_2 are greater than zero, thus resulting in semicircles on the axis when plotted as function of frequency.

At the peak of the semicircle, the following condition is obtained:

$$\omega_{max} R_2 C = 1 \qquad (4.18)$$

and hence

$$C = \frac{1}{2\pi f_{max} R_2} \qquad (4.19)$$

Knowing the value of R_2 and the frequency f_{max}, the value of the capacitance can be determined. It is possible to obtain all the three parameters (R_1, R_2 and

C) from the Cole-Cole plot as shown in figure 4.3 (b), provided a sufficient frequency range is investigated.

4.5.1 Understanding modelled capacitance values

For high purity diamond, the dielectric constant is reported around 5.7 [10]. Thus the formula (4.20) indicates that the grain interior capacitance from diamond is estimated around 0.5 pF.

$$C_{gi} = \frac{A \varepsilon_o \varepsilon_{gi}}{L} \qquad (4.20)$$

where C_{gi} is the capacitance of the grain interiors, L is the sample length, A is the cross sectional area, ε_o is the permittivity of free space (8.854×10^{-12} F/m), and ε_{gi} is the electrical relative dielectric constant of the grain interior. L is the sample length within the order of millimeters (mm). A is the cross sectional area within the order of 10 mm^2.

The same A and L values can be applied to the grain boundary capacitance (C_{gb}) in equation 4.21. In addition, the grain boundary induced dipole polarization may cause the dielectric constant (ε_{gb}) to be slightly higher than that of grain bulk (ε_{gi}), but probably on the same magnitude order as grain bulk [11]. Furthermore, the grain size of a typical polycrystalline material is usually on the order of micrometers (μm), where the effective grain boundary width is expected to be on the order of nanometres (nm) [12]. Thus the estimated grain boundary capacitance for a polycrystalline diamond is around 0.5 nF.

$$C_{gb} = \frac{A \varepsilon_o \varepsilon_{gb}}{L} \frac{d}{\delta} \qquad (4.21)$$

where d is the grain size, δ is the grain boundary width, and ε_{gb} is the relative dielectric constant of the grain boundary.

Finally, the AC potential input signal used for impedance spectroscopy measurements in this thesis was 5 V_{rms}.

4.6 Scanning electron microscopy

The scanning electron microscope (SEM) is a type of electron microscope that images the sample surface by scanning it with a high-energy beam of electrons in a raster scan pattern. The electrons interact with the atoms that make up the sample producing signals that contain information about the sample's surface topography, composition and other properties such as electrical conductivity. The types of signals produced by an SEM include secondary electrons, back-scattered electrons (BSE), characteristic X-rays, light (cathodoluminescence), specimen current and transmitted electrons. Secondary electron detectors are common in all SEMs, but it is rare that a single machine would have detectors for all possible signals. The signals result from interactions of the electron beam with atoms at or near the surface of the sample. In the most common or standard detection mode, secondary electron imaging or SEI, the SEM can produce very high-resolution images of a sample surface, revealing details from 1 to 5 nm in size.
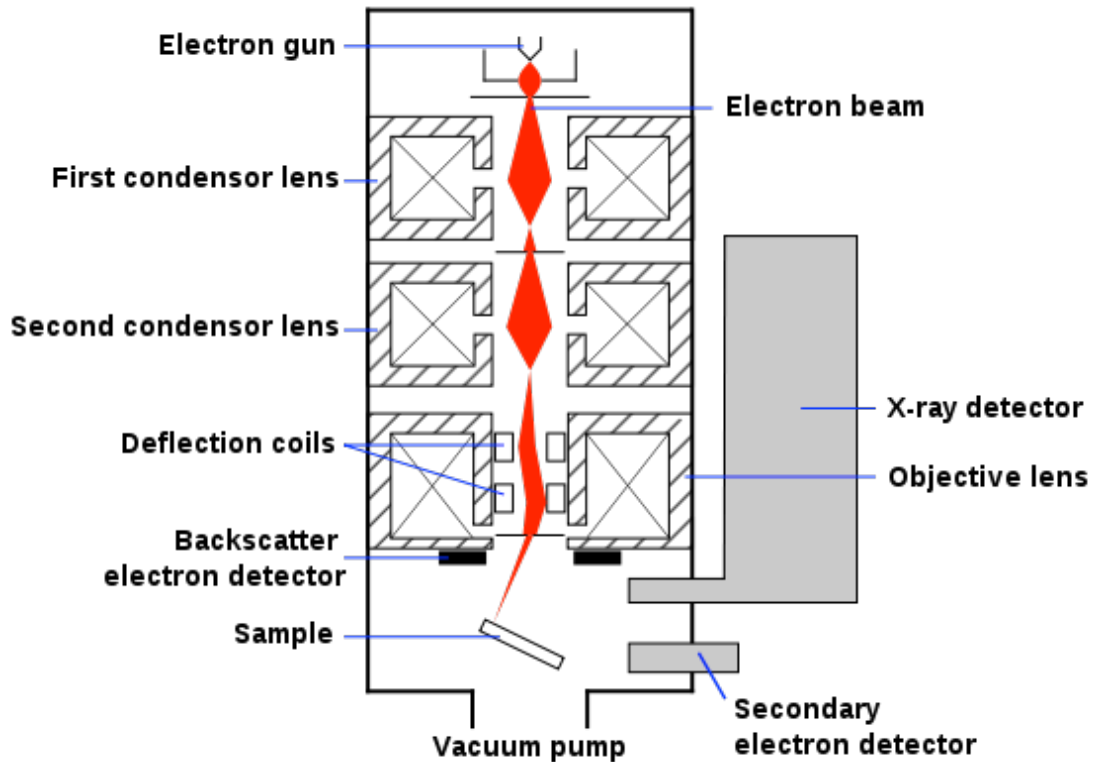
Figure 4.4: Schematic of a Scanning electron microscope (SEM) (from [13]).

In a typical SEM, an electron beam is thermionically emitted from an electron gun fitted with a tungsten filament cathode. Tungsten is normally used in thermionic electron guns because it has the highest melting point and lowest vapour pressure of all metals, thereby allowing it to be heated for electron emission, and because of its low cost.

The electron beam, which typically has an energy ranging from 0.5 keV to 40 keV, is focused by one or two condenser lenses to a spot about 0.4 nm to 5 nm in diameter. The beam passes through pairs of scanning coils or pairs of deflector plates in the electron column, typically in the final lens, which deflect the beam in the x and y axes so that it scans in a raster fashion over a rectangular area of the sample surface. When the primary electron beam interacts with the sample, the electrons lose energy by repeated random scattering and absorption within a teardrop-shaped volume of the specimen known as the interaction volume, which extends from less than 100 nm to around 5 µm into the surface. The size of the interaction volume depends on

the electron's landing energy, the atomic number of the specimen and the specimen's density. The energy exchange between the electron beam and the sample results in the reflection of high-energy electrons by elastic scattering, emission of secondary electrons by inelastic scattering and the emission of electromagnetic radiation, each of which can be detected by specialized detectors. The beam current absorbed by the specimen can also be detected and used to create images of the distribution of specimen current. Electronic amplifiers of various types are used to amplify the signals that are displayed as variations in brightness on a cathode ray tube. The raster scanning of the CRT display is synchronised with that of the beam on the specimen in the microscope, and the resulting image is therefore a distribution map of the intensity of the signal being emitted from the scanned area of the specimen. The image may be captured by photography from a high-resolution cathode ray tube, but in modern machines is digitally captured.

4.7 Scanning tunneling microscopy

A scanning tunneling microscope (STM) is a powerful instrument for imaging surfaces at the atomic level. For an STM, good resolution is considered to be 0.1 nm lateral resolution and 0.01 nm depth resolution [14]. With this resolution, individual atoms within materials are routinely imaged and manipulated.

The STM is based on the concept of quantum tunneling. When a conducting tip is brought very near to the surface to be examined, a bias (voltage difference) applied between the two can allow electrons to tunnel through the vacuum between them. The resulting tunneling current is a function of tip position, applied voltage, and the local density of states (LDOS) of the sample [15]. Information is acquired by monitoring the current as the tip's position scans across the surface, and is usually displayed in image form. STM can be

a challenging technique, as it can require extremely clean and stable surfaces, sharp tips, excellent vibration control, and sophisticated electronics.
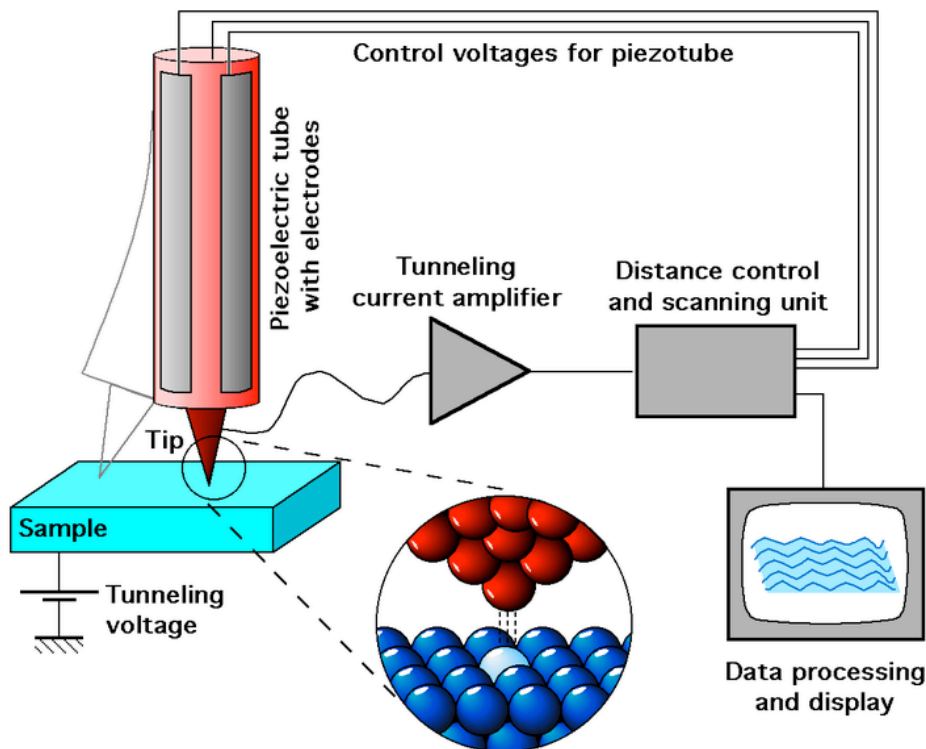
Figure 4.5: Schematic view of a STM setup (from [16]).

4.8 Raman spectroscopy

Raman spectroscopy is a spectroscopic technique based on inelastic scattering of monochromatic light, usually from a laser source. Inelastic scattering means that the frequency of photons in monochromatic light changes upon interaction with a sample. The frequency of the reemitted photons is shifted up or down in comparison with original monochromatic frequency, which is called the Raman effect. This shift provides information about vibrational, rotational and other low frequency transitions in molecules. Raman spectroscopy can be used to study solid, liquid and gaseous samples.

The mechanism by which the Raman effect occurs can be understood from the interaction between the oscillating induced polarization or the dipole moment of the molecule (P) and the time-dependent electric field vector of the incident radiation (E).

$$E_i = E_i^0 \cos 2\pi c \omega_0 t,$$

(4.22)

where E_i^0 is the ith component of the time-dependent electric field amplitude and ω_0 is the frequency of the electric field (E_i). The time-dependent induced polarization (P) is also caused by the electric field (E), which interacts through the molecular polarizability α.

$$P = \alpha E$$

(4.23)

As the molecule vibrates (undergoes atom displacements), the electronic charge distribution and, hence, the polarizability (α) varies in time. The polarizability is related to the electron density of the molecule and is often visualized in three dimensions as an ellipsoid and represented mathematically as a symmetric second-rank tensor. The time-dependent amplitude (Q_k) of a normal vibrational mode executing simple harmonic motion is written in terms of the equilibrium amplitude Q_k^0, the normal mode frequency ω_k, and time (t).

$$Q_k = Q_k^0 \cos 2\pi c \omega_k t$$

(4.24)

An expression for the induced polarization can be derived in terms of the normal coordinate and electric field by writing the polarizability as a Taylor series in the normal coordinate and retaining only the linear terms. For the ij component, then,

$$\alpha_{ij} = \alpha_{ij}^0 + \sum_{k=1}^{3n-6} \left(\frac{\partial \alpha_{ij}}{\partial Q_k}\right) Q_k + \ldots$$

(4.25)

The combination of equations (4.22-4.25) shows that the induced polarization is composed of nine terms similar to the $\alpha_{ij}E_i$ component depicted in equation (4.26).

$$\alpha_{ij}E_i = \alpha_{ij}^0 E_i^0 \cos 2\pi c \omega_0 t +$$

$$E_i^0 \sum_{k=1}^{3n-6} \tfrac{1}{2}\left(\frac{\partial \alpha_{ij}}{\partial Q_k}\right)_e Q_k^0 \qquad X$$

$$\left[\cos 2\pi c (\omega_0 + \omega_k) t + \cos 2\pi c (\omega_0 - \omega_k) t\right].$$

(4.26)

The first term in equation (4.26) corresponds to the elastic component of the scattered light (Rayleigh scattering), while the second term corresponds to the inelastically scattered Raman component. Equation (4.26) also indicates that Raman scattered light can occur at two new frequencies different from the incident light frequency. These correspond to Stokes (W_o - W_k) and anti-Stokes (W_o+ W_k) scattering processes.

Interaction between incident electromagnetic radiation and the electrons in a solid can occur to yield scattering because the time-varying electric field of the radiation can induce a dipole moment (M) in the solid. The induced dipole moment will vary with the frequency of the incident field and generate elastic scattering (Rayleigh) at the same frequency as the incident radiation, but scattered over 360°. For inelastic scattering, energy can be "removed" from the induced dipole moment if a vibrational excitation (phonon) can be produced in the solid. This excitation is characterized by a time-varying

dipole moment during vibration of the normal mode, associated with that phonon. As with a single molecule, this vibrational mode must exhibit a change in polarizability during the vibration to exhibit Raman activity. Following a Raman scattering process, the system will be left in a higher vibrational level corresponding to a Stokes process and emission of red-shifted light, or a lower level resulting from anti-Stokes scattering and emission of blue-shifted light from the wavelength of the incident excitation. Figure 4.6 depicts these two scattering processes and shows the relationship between the Stokes/anti-Stokes intensity ratio and the Boltzmann factor.
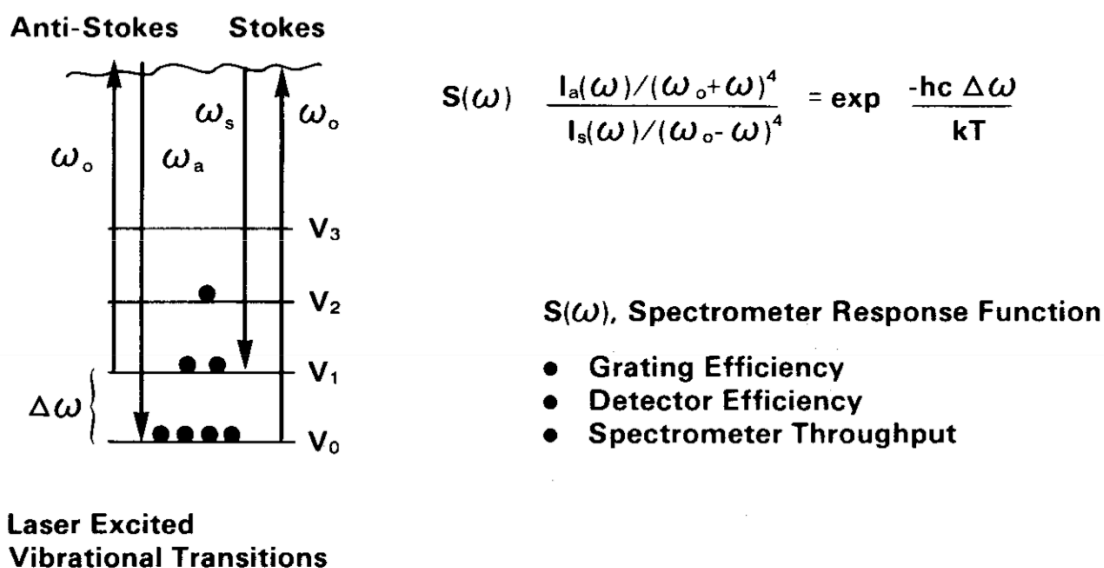
Figure 4.6: Laser-excited vibrational transitions and the relationship of Stokes/Anti- Stokes band intensity ratios to temperature (from [17]).

4.9 Energy-dispersive X-ray spectroscopy

Energy dispersive X-ray spectroscopy (EDS or EDX) is an analytical technique used for the elemental analysis or chemical characterization of a sample.

If a localized electron has been knocked out of an atom the atom is in an excited, high energy, state. At some later time the empty electron state will be filled and the atom will relax, giving off the excess energy as a secondary effect. There are essentially three ways in which this relaxation can happen. If the vacant electron state is an outer state then the energy to be given off will be small and is commonly emitted in the form of a photon that may be in the visible range. This effect is known as cathodoluminescence.

If on the other hand the vacant state is an inner state the amount of energy to be released is larger and there are two main possibilities: a characteristic X-ray or a characteristic (Auger) electron may be emitted. These two processes are shown schematically in figure 4.7. If an X-ray is to be emitted a single outer electron jumps into the inner shell vacancy (figure 4.7(a)). The energy of the X-ray is then the difference between the energies of the two excited states and this is specific to a particular atomic species. The wavelength of this X-ray can be calculated from

$$\lambda = \frac{hc}{\Delta E}$$

(4.27)

where h is Planck's constant, c is the speed of light and ΔE is the energy difference between excited states.
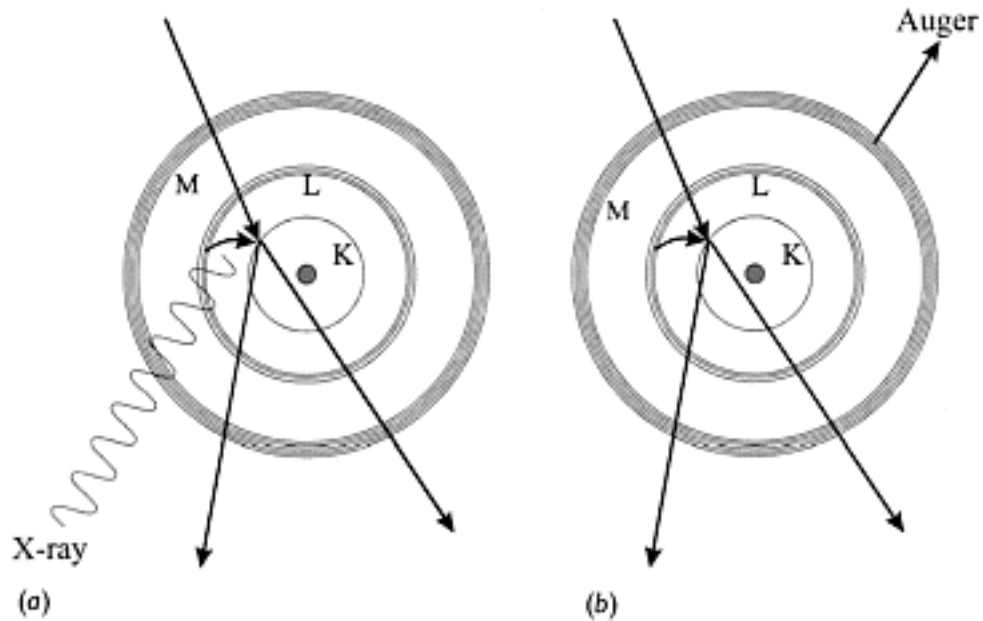
Figure 4.7: The two ways in which an inner-shell-excited atom can relax. In both cases a K shell electron has been knocked out – in (*a*) a characteristic (K_α) X-ray is emitted while in (*b*) an Auger electron (KLM) is ejected (from [18]).

These energies and wavelengths are different for each atomic species and by measuring them we can determine which elements are present in the specimen.

Before one can use the X-rays for analytical purposes one needs to know which of the many characteristic X-ray lines for each element is the most intense; this enables us to choose the best line to use as an index of how much of each element is present in the sample.

It transpires, that in the K series the lines $K_{\alpha 1}$ and $K_{\alpha 2}$ (which may be so close together that they cannot be distinguished) are seven to eight times more intense than $K_{\beta 1}$ and $K_{\beta 2}$ (another close pair). Consequently the K 'doublet', as it is called, is most frequently used for analysis. However, it is not always possible to excite the K series of lines in an electron beam instrument since, as the atomic number of the emitting element increases, the energy required to knock out a K-shell electron also increases. For example, elements heavier than tin ($Z = 50$) need electrons of more than 25keV to excite any K lines at all, and are not efficient producers of K X-rays until the incident electron energy is about 75keV. Since we would like to be able to analyze a specimen

in an SEM, where electron energies of perhaps only 30keV are available, we must look for other characteristic X-rays that are more easily excited in order to detect heavy elements. Fortunately the L series of lines shown in figure 4.8, or even the M series for very heavy elements, has very suitable properties. Again it turns out that of the vast number of possible lines, $L_{\alpha 1}$ and $L_{\alpha 2}$ are far stronger than the remainder, which can normally be ignored. A similar effect narrows the M series down to a few useful lines. Table 4.1 shows the energy and associated wavelength of the strongest K, L and M lines of the elements. The most efficient production of X-rays generally occurs when the bombarding electrons have about three times the X-ray energy. A study of table 4.1 will show that the selected elements have at least one strong X-ray line with energy less than 10keV and therefore there should be no difficulty in analyzing all the elements, using a scanning electron microscope operating at 25–30keV.
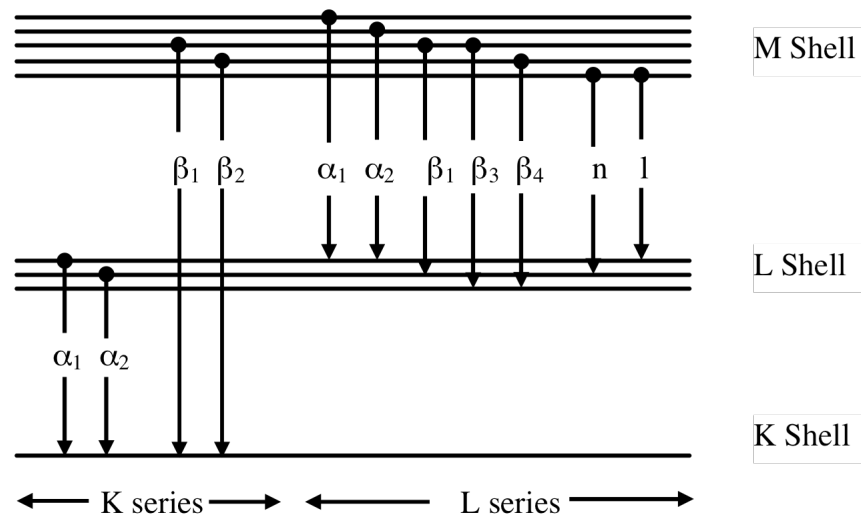
Figure 4.8: Some of the more common transitions between the K, L and M shells of an atom that lead to the X-ray lines indicated (from [18]).

Element	Atomic Number Z	Relative Actomic Mass A_r	$K_{\alpha 1}$ E(keV) (a)	λ(nm) (b)	$L_{\alpha 1}$ E(keV) (a)	λ(nm) (b)	$M_{\alpha 1}$ E(keV) (a)	λ(nm) (b)
Hydrogen	1	1.0						
Helium	2	4.0						
Lithium	3	6.9	0.05					
Beryllium	4	9.0	0.11	11.40				
Boron	5	10.8	0.18	6.76				
Carbon	6	12.0	0.28	4.47				
Nitrogen	7	14.0	0.39	3.16				
Oxygen	8	16.0	0.52	2.36				
Fluorine	9	19.0	0.68	1.83				
Neon	10	20.2	0.85	1.46				
Sodium	11	23.0	1.04	1.19				
Magnesium	12	24.3	1.25	0.99				
Aluminium	13	27.0	1.49	0.83				
Silicon	14	28.1	1.74	0.71				
Phosphorus	15	31.0	2.01	0.61				
Sulphur	16	32.1	2.31	0.54				
Chlorine	17	35.5	2.62	0.47				
Argon	18	39.9	2.96	0.42				
Potassium	19	39.1	3.31	0.37				
Calcium	20	40.1	3.69	0.34	0.34	3.63		
Scandium	21	45.0	4.09	0.30	0.39	3.13		
Titanium	22	47.9	4.51	0.27	0.45	2.74		
Vanadium	23	50.9	4.95	0.25	0.51	2.42		
Chromium	24	52.0	5.41	0.23	0.57	2.16		
Manganese	25	54.9	5.90	0.21	0.64	1.94		
Iron	26	55.8	6.40	0.19	0.70	1.76		
Cobalt	27	58.9	6.93	0.18	0.77	1.60		
Nickel	28	58.7	7.48	0.17	0.85	1.46		
Copper	29	63.5	8.05	0.15	0.93	1.33		
Zinc	30	65.4	8.64	0.14	1.01	1.23		

Table 4.1: The energy and associated wavelength of the strongest K, L and M shells (from [18]).

Statistical rules predict the smallest concentration of an element that can be detected with an EDX system. If one is trying to detect a very minor element, very long (hours) acquiring times are required. In this instance more sensitive techniques can be employed such as secondary ion mass spectroscopy (SIMS).

The minimum detection limit (m_{dl}) or `lower limit of detection' (l_{ld}) is given by:

$$m_{dl} = \frac{k\sqrt{2}}{c'}\sqrt{\frac{N_b}{T}} \qquad (4.28)$$

where N_b = background intensity (under the peak of interest), T = counting lifetime for the experiment and c' = counts per sec per wt% of the element in question.

$$c' = \frac{N_p - N_b}{c} \qquad (4.29)$$

where c = wt% concentration of the element in question, k = 1 when the peak is identified at 68.3% confidence, k = 2 when the peak is identified at 95.4% confidence and k = 3 when the peak is identified at 99.7% confidence of the selected elements.

Most EDX analysis programs operate at 95.4% (k=2) confidence levels [18]. EDX detection limits are therefore ~0.2 % for heavy elements and 4-5 % for light elements, when T< 300 seconds [18].

4.10 Glow discharge technique (direct current)

Electric glow discharge is a type of plasma formed by passing a current at 100 V to several kV through a gas at low pressure. The simplest type of glow discharge is a direct-current glow discharge. In its simplest form, it consists of two electrodes in a cell held at low pressure (0.1–10 Torr; about 1/10000th to 1/100th of atmospheric pressure). The cell is typically filled with argon, but other gases can also be used. An electric potential of several hundred volts is applied between the two electrodes. A small fraction of the population of atoms within the cell is initially ionized through random processes (thermal collisions between atoms or with alpha particles, for example). The ions (which are positively charged) are driven towards the cathode by the electric potential, and the electrons are driven towards the anode by the same potential. The initial population of ions and electrons collides with other atoms, ionizing them. As long as the potential is maintained, a population of ions and electrons remains. The electric fields in the system are restricted to sheaths at each of the electrodes. The sheath fields are such as to repel electrons trying to reach either electrode.
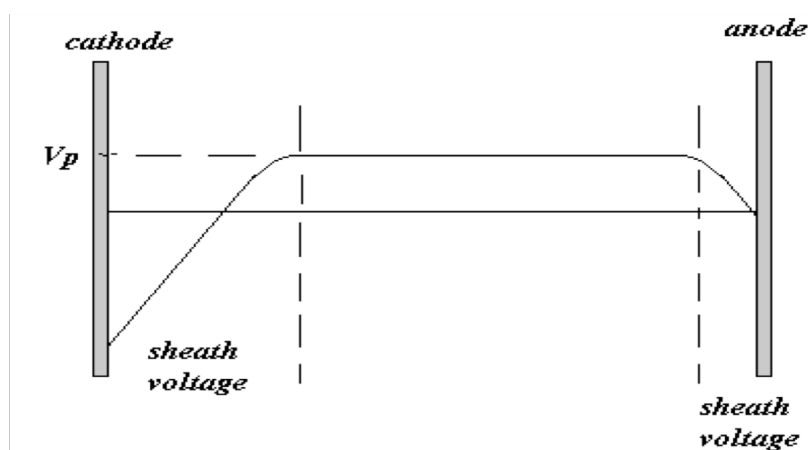
Figure 4.9: Voltage distribution in a dc glow discharge process (from [19]).

4.11 References

1. B Baral, SSM Chan and RB Jackman, J. Vac. Sci. Technol. A 14 2303 (1996).

2. F Fang, CA Hewett, MG Fernandes and SS Lau, IEEE Transactions on Electron Devices 36 1783 (1989).

3. SA Grot, GS Gildenblat, CW Hatfield, CR Wronski, AR Badzian, T Badzian and R Messier, IEEE Electron Devices Letters 11 100 (1990).

4. GS Gildenblat, SA Grot and A Badzian, Proceedings of the IEEE 79 647 (1991).

5. Y Mori, H Kawarada and A Hiraki, Appl. Phys. Lett. 58 940 (1991).

6. K Das, V Venkatesan, K Miyata, DL Dreifus and JT Glass, Thin Solid Films 212 19 (1992).

7. S.M. Sze, Physics of Semiconductor Device. John Wiley & Sons, Inc. New York, New York (1981).

8. D.K.Schroder, Semiconductor Material and Device Characterization, 2nd ed. (Wiley, New York, 1998).

9. Macdonald JR, Impedance Spectroscopy, Wiley, New York (1987).

10. R F Davis, Diamond Films and Coatings, Development, Properties and Applications (Noyes) p 14 (1993)

11. Daniel Vera V, Dielectric Relaxation, Academic Press, London (1967).

12. M Aoki, YM Chiang, I Kosacki, LJ Lee, J Tuller and YP Liu, J. Am. Ceram. Soc. 79 1169 (1996).

13. http://en.wikipedia.org/wiki/Scanning_electron_microscope.

14. C. Bai, Scanning tunneling microscopy and its applications. New York: Springer Verlag. (2000).

15. C. Julian Chen, Introduction to Scanning Tunneling Microscopy. Oxford University Press (1993).

16. http://en.wikipedia.org/wiki/Scanning_tunneling_microscope.

17. G.E. McGuire, Characterization of Semiconductor Materials - Principles and Methods, Volume 1.. William Andrew Publishing/Noyes (1989).

18. P.J. Goodhew, J. Humphreys**,** R. Beanland, "Electron Microscopy and Analysis", Third edition, Taylor & Francis (2004).

19. Alexander A. Fridman, Lawrence A. Kennedy, Plasma physics and engineering (Taylor & Francis) 2004.

Chapter 5: Electronic properties of homoepitaxial (111) highly boron-doped diamond films

5.1 Introduction

5.2 Experimental methods

5.3 Results

5.4 Discussion

5.5 Conclusions

5.6 References

5.1 Introduction

It has been known for some time that boron within crystalline diamond leads to the formation of an acceptor state and hence p-type conductivity [1], with natural so-called type IIb boron-containing stones being blue in colour due to the presence of substitutional boron atoms. An activation energy for the acceptor states of around 0.37eV was established. High-pressure high-temperature (HPHT) grown diamond can be doped by the addition of pure boron to the growth capsule. Compensation of the boron acceptors by donor levels within the crystal, most normally associated with nitrogen, was found to be growth sector dependent with (110) directions displaying the highest number of uncompensated acceptors at low doping concentrations, whilst (111) suffered the least from compensation at high doping levels [2]. The emergence of chemical vapour deposition (CVD) methods for the formation of diamond films led to a number of investigations of the nature of boron within CVD grown homoepitaxial, single crystal, films [3-5]. These studies concentrated on (100) oriented growth, and used tri-methylborane (C_3H_9B) as a source of boron during the CVD process. Metallic conduction was reported for the temperature range 300-770K for a boron concentration of 3 x 10^{20} cm^{-3} [3]. A study by Visser $et\ al$ [6] reported on the influence of crystal orientation in terms of (100) and (110) samples; higher boron concentrations and lower carrier mobilities were found for the (110) samples compared with (100), for

the same growth conditions, which was explained in terms of a differing growth mechanism for each. In a comprehensive study of homoepitaxial (100) films grown by microwave-plasma CVD, Borst and Weiss [7] found that the activation energy for the boron-induced acceptor state varied from 0.37eV to effectively zero over the boron concentration range 10^{17} – $3 \times 10^{20} cm^{-3}$, consistent with the expected metal-insulator (Mott) transition of 2×10^{20} cm^{-3} [8]. The influence of compensating nitrogen within CVD grown (100) diamond homoepitaxial films has been explicitly studied by Sonoda and co-workers [9], who reported a four times increase in Hall mobility values when ultra-high purity, low nitrogen containing, growth gases were used during the CVD process. Lagrange et al [10] grew homoepitaxial (100) films with boron concentrations within the range 5×10^{16} to $8 \times 10^{20} cm^{-3}$. For boron concentrations up to $2 \times 10^{17} cm^{-3}$ the activation energy was observed to be the 0.37eV expected for the ionisation of boron with compensation ratios of around 10%. Above this and up to $10^{19} cm^{-3}$ an E_a value of 0.185 was determined, with a compensation ratio less than 10%, whilst hopping conduction was considered dominant above this, with metallic conductivity at boron concentrations above $3 \times 10^{20} cm^{-3}$.

An important development in the field of diamond electronics has been the development of n-type diamond homoepitaxial films through the introduction of phosphorus containing gases during the CVD process [11]. However, it has now been firmly established that the phosphorus donor level lies deep within the diamond band gap at around 0.6eV, and that the most effective creation of substitutional phosphorus requires the use of (111) crystal orientations [12]. The pursuit of diamond-based bipolar devices would therefore appear to require the development of high quality boron doped (111) films to enable the use of phosphorus doped n-type diamond. Moreover, the deep donor level created by phosphorus implies that the fabrication of devices for high temperature applications is likely to be the most useful avenue to explore for this form of diamond technology. Indeed, high temperature electronics is seen as one of the major future uses of active

diamond devices. However, little has currently been reported on the electronic properties of boron-doped (111) films, and insight into the behaviour of doped diamond at high temperatures (>500K) is limited. Ri and co-workers [13] recently reported that the growth and doping mechanisms during homoepitaxial growth of boron doped films on (111) diamond films by CVD methods strongly differed from those on (100). They observed an increase in Hall mobility values and a decrease in compensation ratio as the methane concentration within the CVD process was increased, the opposite observation to that for the growth of boron doped (100) films. In the current study we have used Hall effect measurements, and STM analysis to evaluate the properties of a range of CVD grown homoepitaxial (111) orientated boron-doped diamond films within the temperature range 300-800K. It will be shown that high mobility valance band transport can be maintained to much higher doping levels in diamond (111) than in (100), which is highly advantageous when it comes to the design of devices based on this material.

5.2 Experimental methods

The samples studied here were grown at CEA laboratories, Saclay, France by Dr Haitao Ye of the Diamond electronics group, University College London. Microwave plasma-enhanced chemical vapour deposition (MWPECVD) of homoepitaxial diamond films was carried out using methane-hydrogen-tri-methylborane (TMB) gas mixtures. The growth of high quality CVD diamond critically relies upon the use of ultra-pure gases; in the current work H_2 was generated *in-situ* from ultra pure water by a 0.5 L/min H_2 generator (F-DBS Strumenti Scientifici) giving nitrogen impurity levels better than N90. Methane was used with N55 purity (99.9995%, Messer B50) and TMB (C_3H_9B) supplied as a 2000ppm mixture in N70 H_2 (99.99999%, Messer B10) with a nitrogen level less than 1.5ppm. HPHT prepared single crystal diamond substrates that were (111) oriented and of type Ib (Sumitomo) were used throughout. These were cleaned *ex-situ* using a boiling (($NH_4)_2S_2O_8$): H_2SO_4

(1:1) solution and rinsed in a (1:1) mixture of (H_2O_2) and (NH_4OH), which is known to leave a graphite free, oxidised diamond surface [14]. Following insertion into the MWPECVD chamber samples were further cleaned using a pure hydrogen-plasma (500sccm, 20W, 5 minutes) prior to growth. Table 5.1 shows the growth conditions used to generate five different types of samples, where the principal variable is the concentration of the TMB within the growth gas mixture.

Sample Type	1	2	3	4	5
CH_4 flow (sccm)	0.8	0.74	0.74	0.74	0.74
H_2 flow (sccm)	500	500	500	500	500
TMB flow (sccm)	0	0.024	0.05	0.1	1.25
Growth duration (hours)	1.5	1.5	1.5	1.5	1.5
Power (W)	20	20	20	20	23
Temperature (^0C)	880	880	880	880	910

Table 5.1: The growth conditions used for samples 1-5.

Hall-effect analysis was performed using a Lakeshore 7504 Hall system with an Advanced Research Systems helium atmosphere-based closed-cycle refrigerator for low temperature measurements (15-300K), and a Lakeshore evacuated probe system for high temperature measurements (300-800K). The magnetic field was oscillated between −1 and 1 T as the signal was recorded. This aspect of the Hall experiments performed here is particularly important when investigating wide band-gap systems, such as diamond, where significant drift in the background voltage can be encountered during detection of the Hall voltage. An example of this is shown in figure 5.1, where it can be readily seen that a single measurement of the Hall voltage could produce misleading results, as it would comprise of a voltage due to

the Hall effect plus a value associated with background drift. The use of field switching method allows this problem to be overcome. Scanning tunneling microscopy (STM) measurements were performed using a "nanosurf" STM in air.

It has been widely observed that the CVD growth of diamond within a chamber that has previously been exposed to boron containing gases will always lead to some level of boron doping within the film, due to the persistence of boron within the growth environment [15]. In the present case, films were grown using a flow rate of TMB, from zero up to 1.25sccm. All films were grown to a thickness of approximately 1μm.

5.3 Results

STM images revealed a change in surface morphology when the highest boron levels within the CVD growth gas mixture were used. Retention of the substrate surface profile is maintained through to sample type 4. For example, figure 5.2(a) shows an STM image for sample type 2, indicating a root-mean-square (RMS) value of 0.2nm, typical of samples 1- 4, whilst figure 5.2(b) shows an image typical for sample type 5. In this case growth domains or 'hillocks' can be observed and the RMS value reaches around 15nm. The very fact that clear STM images could be produced for all films indicates that some electrical conductivity was present, even when films were grown without the purposeful introduction of boron containing gas to the growth mixture.

Hall effect measurements, carried out over the temperature range 300-800K are presented in figures 5.3-5.5. Figure 5.3 displays the sheet resistivity vs 1000/T in a semi-logarithmic plot (a) for samples 1-3 (b) samples 4-5. Data recorded for sample types 1-3 were qualitatively similar, showing near-linear characteristics at high temperatures, with a slightly different slope being

apparent at lower temperatures. For the lightest doped sample (1), the transition is around 350K, whereas for sample 3 it is closer to 450K. The resistivity values fall with sample number, i.e. 1>5. In the case of sample type 4 it is more difficult to distinguish the two regimes and the resistivity has decreased by a further order of magnitude. For sample type 5, the shape of the graph is completely changed, showing little resistivity variation over the entire temperature range, with the sheet resistivity again decreasing to 50 Ohm/sq over the measured range.

Sheet carrier densities are plotted in figure 5.4, again against 1000/T in semi-logarithmic format for samples (a) 1-3 (b) 4 and 5. For sample 1 the carrier density can be seen to range from 10^{18} cm^{-3} at low temperatures (300K) to 2 x 10^{19} cm^{-3} at high temperatures (800K). A similar trend is evident for sample 2, but the values are now 7 x 10^{18} cm^{-3} to 6 x 10^{19} cm^{-3}. Sample 3 shows some scatter within the data set, but values between 7 x 10^{18} and 6.5 x 10^{19} cm^{-3} can be determined. Interestingly, the trends observed for samples 4 and 5 differ strongly from the others. In both cases there is some scatter in the data points, but the change of carrier density with temperature is much less pronounced and lies within the range 1 – 3 x 10^{20} cm^{-3} for sample 4, to 9 x 10^{20} – 2 x 10^{21}cm^{-3} for sample 5.

Figure 5.5(a) & (b) presents the mobility data as a function of temperature for the various samples; (a) for samples 1-3 (b) for samples 4 and 5. Sample 1 shows an increase in mobility, peaking at 20cm^2/Vs at 450K, before declining to around 15cm^2/Vs at 800K. In the case of sample 2 the mobility value can be seen to gradually rise from around 1.3 cm^2/Vs at 350K to 11cm^2/Vs at 600K, decreasing to 8.5cm^2/Vs at 800K. Sample 3 displays a similar trend with a mobility of 1.7cm^2/Vs recorded at 300K, 9cm^2/Vs recorded at 600K and 7.5cm^2/Vs recorded at 800K. Sample 4 (figure 5.5(b)) shows an increase from 6-14 cm^2/Vs with increasing temperature, whilst sample 5 (figure 5.5(b)) exhibits a less significant trend, with much lower mobility values in the region of 1.5 cm^2/Vs.
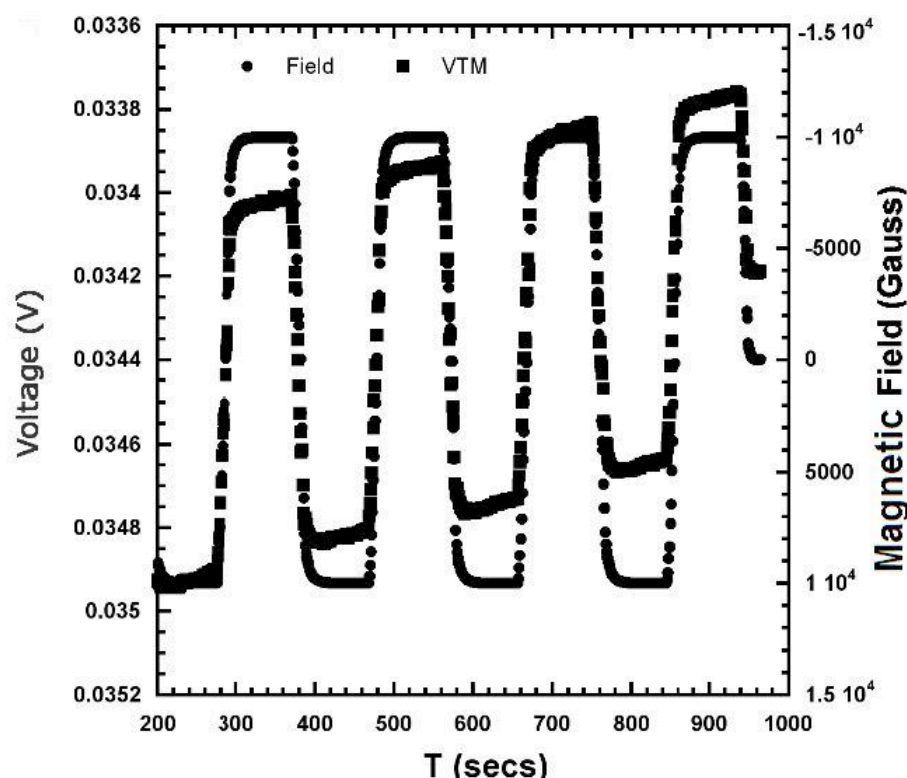
Figure 5.1: Hall voltage (left scale) and magnetic field variation (right scale) plotted as a function of time during a Hall measurement. The stable field variation can be contrasted with the background drift that is apparent in the Hall voltage.
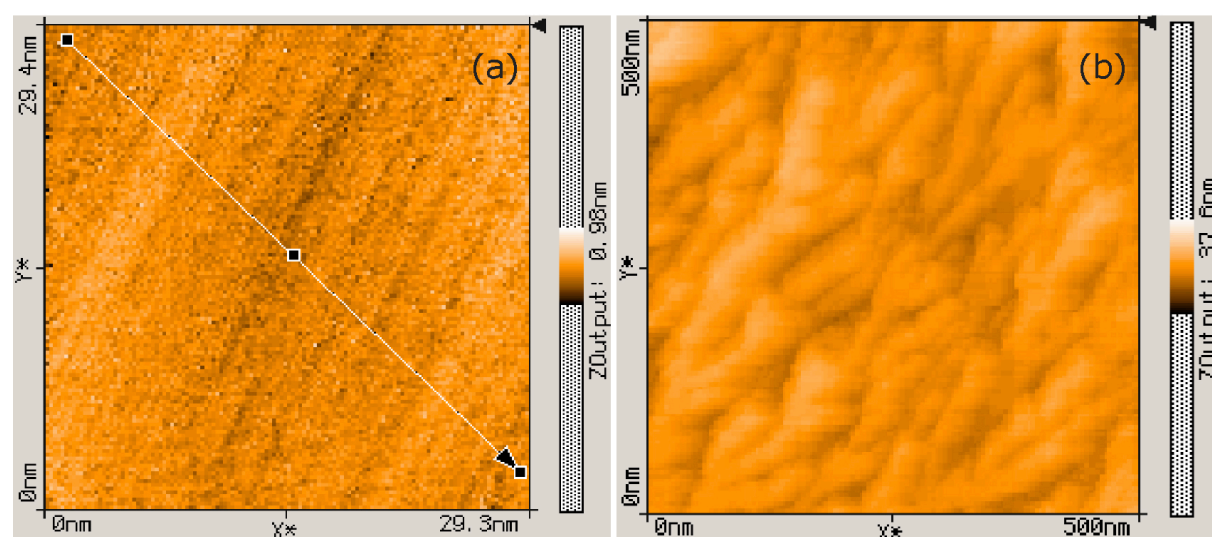
Figure 5.2: Scanning tunnelling microscope (STM) images for (a) sample type 2, indicating a rms value of 0.2nm and (b) sample type 5 showing domains or 'hillocks' with an rms value of around 15nm.
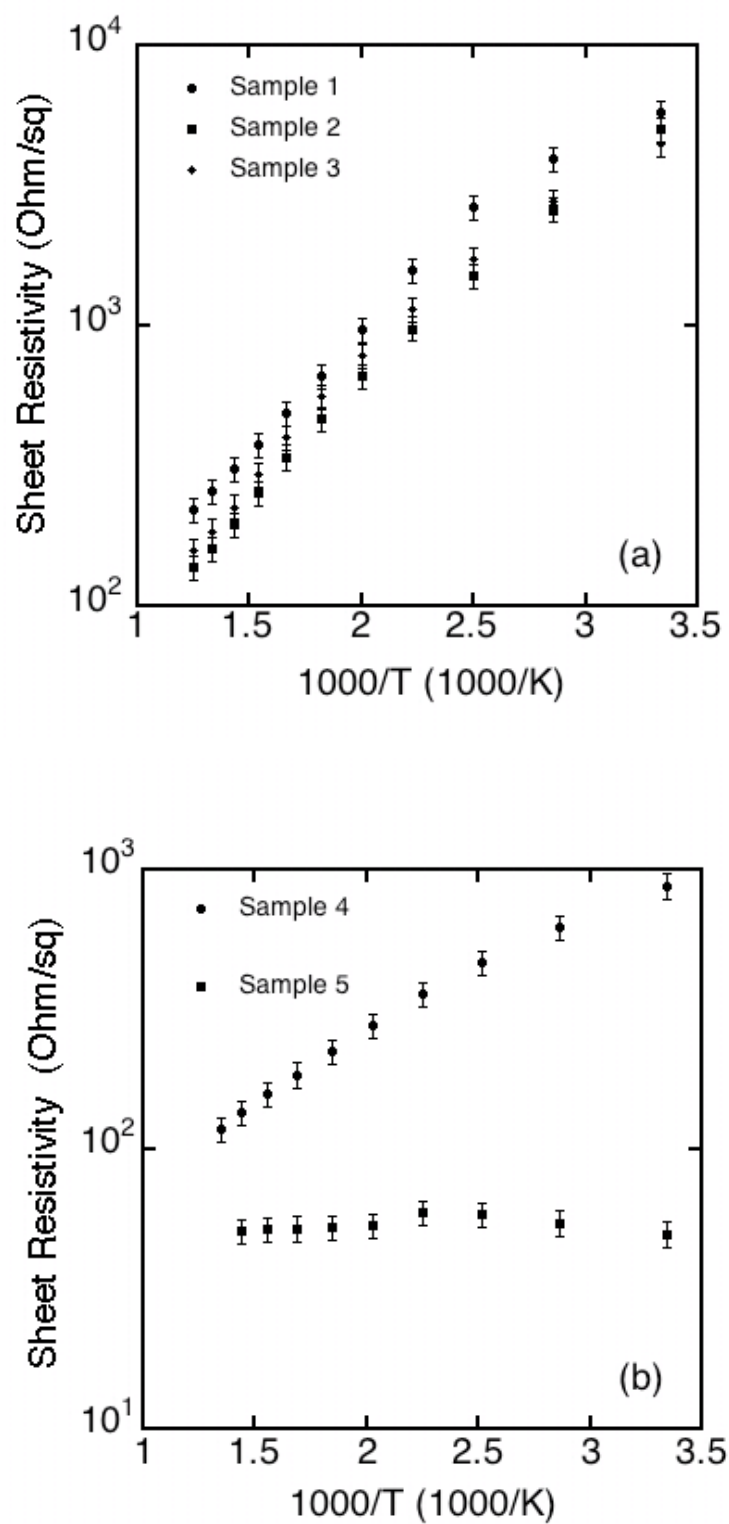
Figure 5.3: Log (sheet resistivity, Ohm/square) vs 1000/T (a) for samples 1-3 (b) samples 4 and 5.
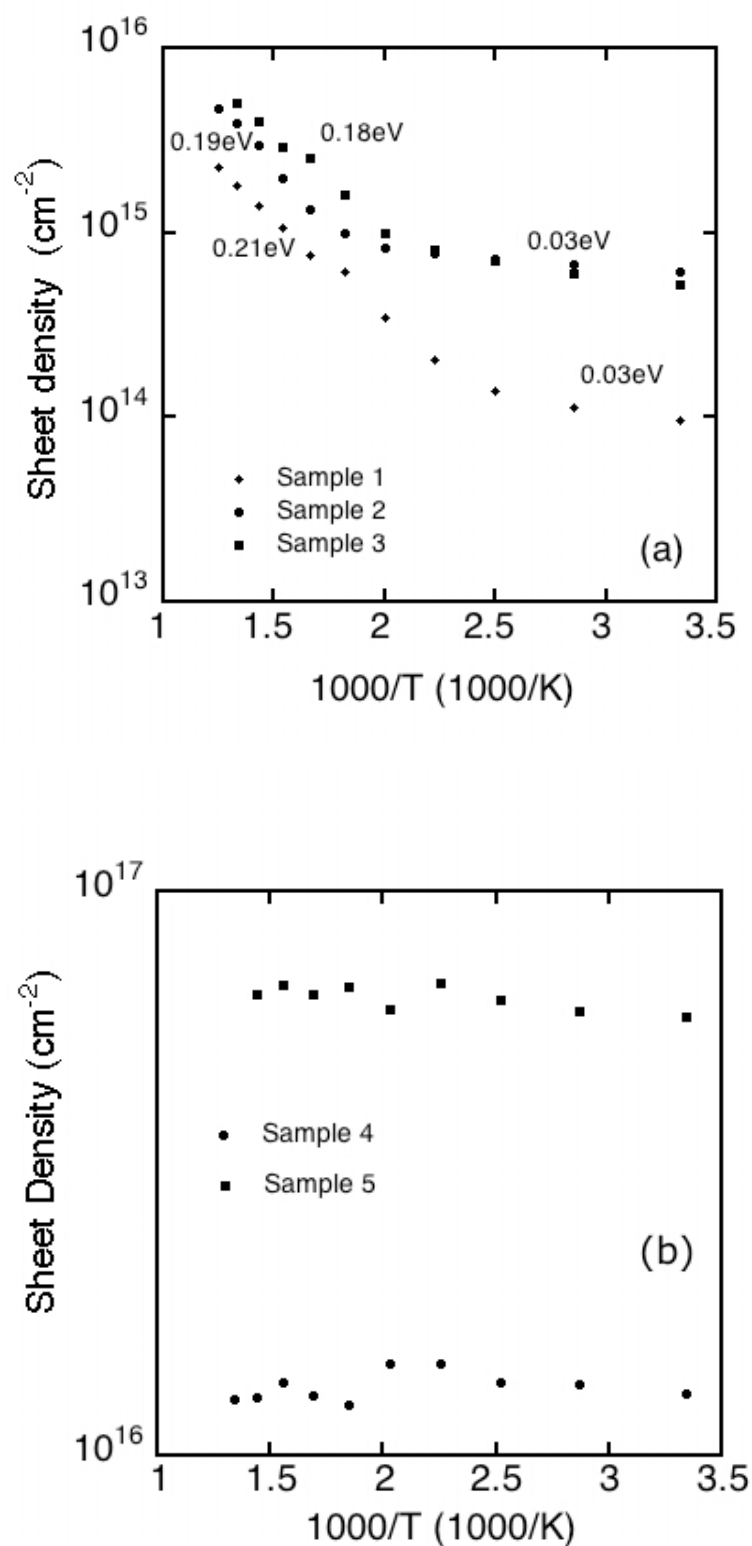
Figure 5.4: Log (sheet density vs 1000/T (a) for samples 1-3 (b) samples 4 and 5.
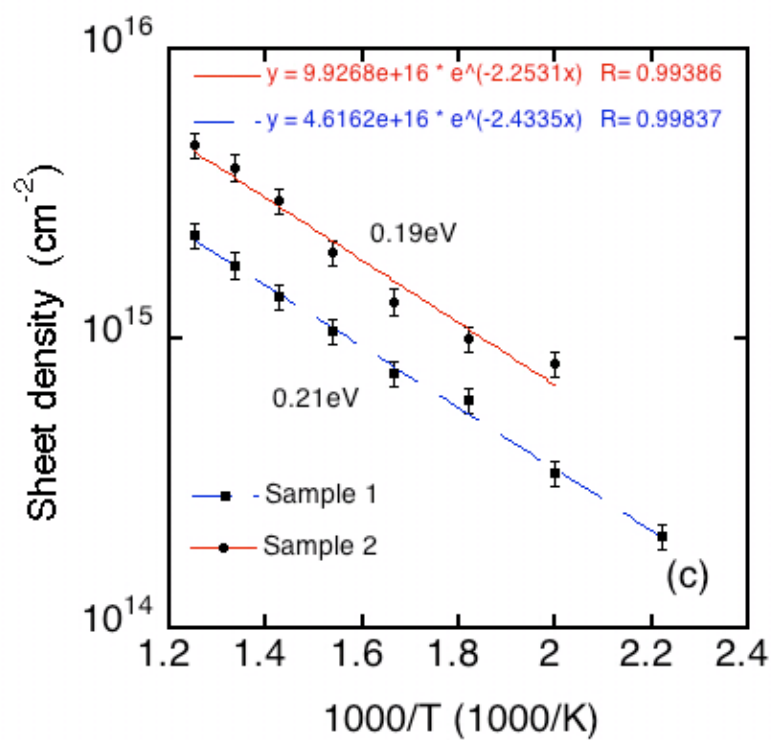
Figure 5.4 (c): Arrhenius fits to sheet density vs 1000/T for samples 1 & 2.
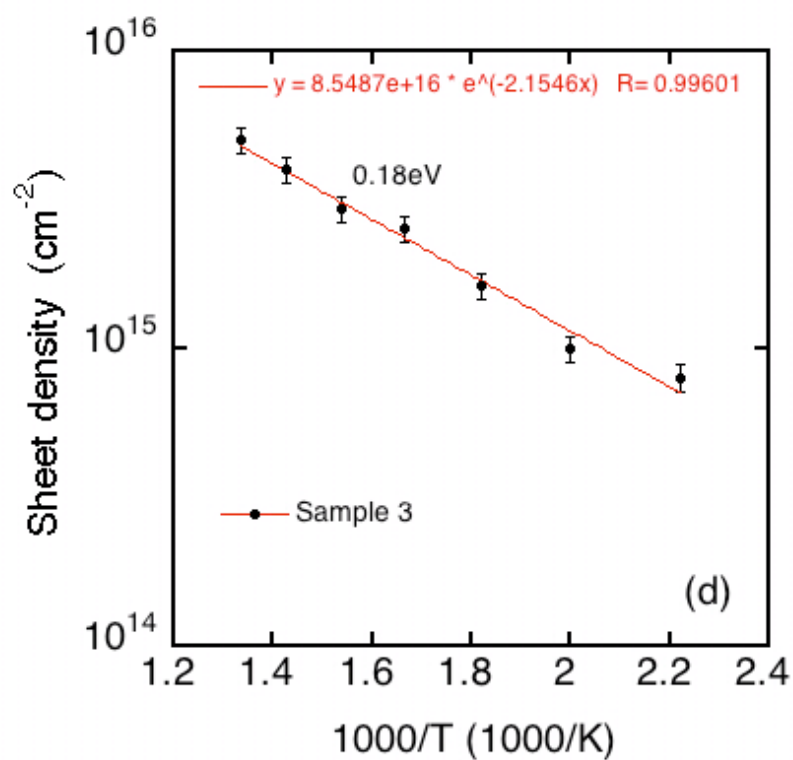
Figure 5.4 (d): Arrhenius fit to sheet density vs 1000/T for sample 3.
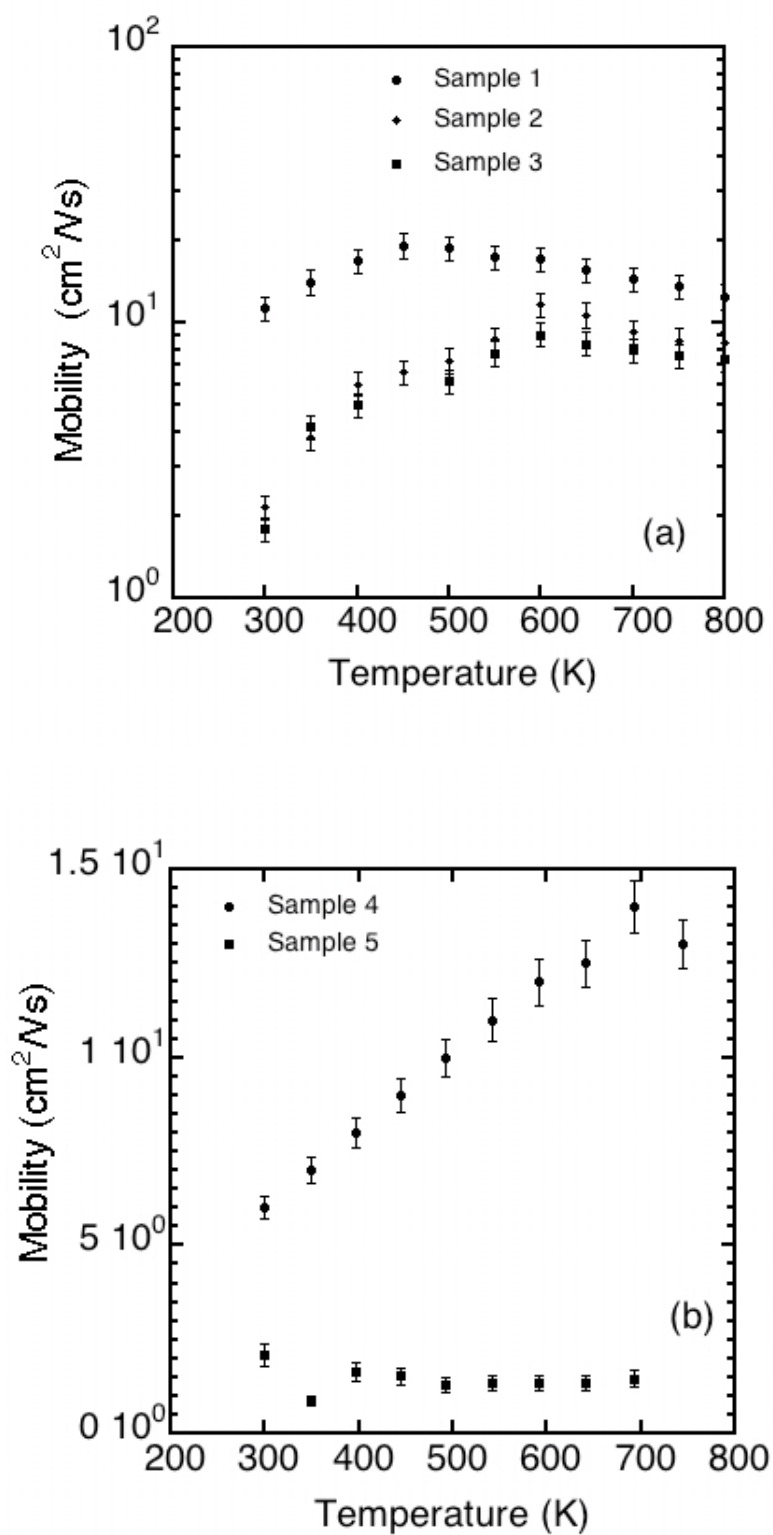
Figure 5.5: Hole mobility (cm²/Vs) vs T (Kelvin) (a) for samples 1-3 (b) for samples 4 and 5.

5.4   Discussion

In the current study the temperature range investigated was from 300-800K, and samples 1-3 were expected to have a lower doping density than samples 4 and 5. This would indeed appear to be the case, given the variation in sheet resistivity that can be seen within figure 5.3. Thermal activation energies associated with the change in resistivity of each sample type can be determined from these plots, and these are given in table 5.2. Borst and Weiss [7] have previously identified a decreasing trend in the activation energy associated with boron doped diamond films with increasing boron concentration for (100) diamond films. Their data would suggest that the activation energies measured in the present arise due to very high doping levels within the diamond films.

The strong variation in the activation energy for electrical conduction within these samples implies the existence of more than one conduction mechanism. In addition to the transport of free carriers (in our case holes within the valance band), doped semiconductors can support conduction through carrier 'hopping'. Hopping conductivity is a conventionally associated with low temperatures in materials such as silicon, but can occur at room temperature or above in diamond, as the boron acceptor state is deep within the diamond band gap. Hopping conduction is normally restricted to samples with significant compensating defects, as donors are required to supply an electron to the boron acceptors, which are not thermally ionised at modest temperatures. A compensation ratio $K = N_D / N_A$ can be used to characterise differing samples. Charge transfer occurs by tunnelling in the process of nearest neighbour hopping [16] or by thermal activation in variable hopping range [17].

Mamin and Inushima [18] discussed the basis of conductivity in heavily boron-doped diamond films, referring to the (100) system. Under high

doping conditions it was supposed that the nearest neighbour of each boron atom might no longer be carbon, with combinations such as B-B, B-C-B, B-C-C-B etc, becoming likely. The fraction of boron atoms occupying these states will depend upon both statistical laws and the nature of the growth conditions used. It can also be supposed to be affected by the crystallographic orientation of the growth plane. This kind of non-trivial state will form a shallow acceptor level with an energy less than 0.37eV; Mamin and Inushima assumed that these states have an energy of 0.06eV (B states associated with B-B, B-C-B, B-C-C-B complexes) above the valance band, and that the relevant statistical law was N_2 (additional boron states) = $N_B^2 V_0$, where V_0, the volume of the interaction area was taken as $5nm^3$). This leads to the assumption that when $N_B = 10^{19}$ cm^{-3}, N_2 will be equal to 5×10^{17} cm^{-3}. If we further assume that the number of compensating donors, N_D, is small compared to N_B, then as the doping level increases N_D will increase more slowly than N_2, until we reach a point where $N_2 > N_D$. In this case the donors only compensate the states associated with N_2 since the energy associated with these states is so small compared to the 0.37eV of N_B. The conductivity behaviour of the samples should now change dramatically, with the co-existence of band and hopping conductivity over a wide temperature range. It was proposed that the emergence of a range of shallow states at very high doping levels leads to conductivity that is mainly hopping in character. Langrange and co-workers [10] proposed that the transition to hopping conductivity in high quality homoepitaxial (100) diamond films occurred at a boron concentration of 1×10^{19} cm^{-3}, with metallic conduction at boron levels of $> 2 \times 10^{20}$cm^{-3}. Hopping conductivity is generally seen as undesirable within semiconductor systems, as it is associated with low mobility values [8].

To determine the concentrations N_A and the compensating level of N_D numerical simulations were performed using the equation for a partially compensated semiconductor,

$$P (p + N_D) / (N_A - N_D - p) = [2\pi m_h kT/h^2]^{3/2} \exp(-E_A/kT) \ldots \qquad (5.1)$$

Where p, m_h, k, T and E_A are the hole concentration, the effective mass of the hole, the Boltzmann constant, sample temperature, Planck constant h and the activation energy for the ionisation of the hole, respectively [19]. The density difference N_A – N_D can be estimated from extrapolation to high temperatures of the log p vs T^{-1} plots. The value of m_h can be taken to be $0.48m_0$. These values N_A – N_D and N_D can be seen in table 5.2, alongside the measured carrier concentrations at 800K. The compensation ratio, N_A/N_D can be seen to be very low, lying in the range 0.1-0.5%.

Sample type	Activation energy (eV)	Measured carrier concentration (cm^{-3})	$N_A - N_D$ by extrapolation to high T (cm^{-3})	N_D determined by simulation (cm^{-3})	$K=N_A/N_D$ Determined by simulation	Carrier mobility (cm^2/Vs) @ 700K/800K	Maximum Carrier mobility (cm^2/Vs)
1	0.21	3×10^{19} (800K)	2×10^{20}	1×10^{18}	0.5%	15 (800K)	20 (450K)
2	0.19	7×10^{19} (800K)	5×10^{20}	7×10^{17}	0.14%	9 (800K)	10 (600K)
3	0.18	7.2×10^{19} (800K)	5.2×10^{20}	6×10^{17}	0.12%	9 (800K)	10 (600K)
4	0.095	2×10^{20} (700K)	-	-	-	14 (700K)	15 (700K)
5	0.004	9×10^{20} (700K)	-	-	-	1.5 (700K)	3 (300K)

Table 5.2: Measured activation energies for sample types 1-5, the measured actual value of acceptor state density (N_A), N_D (by simulation) and the carrier mobilities measured in this study.
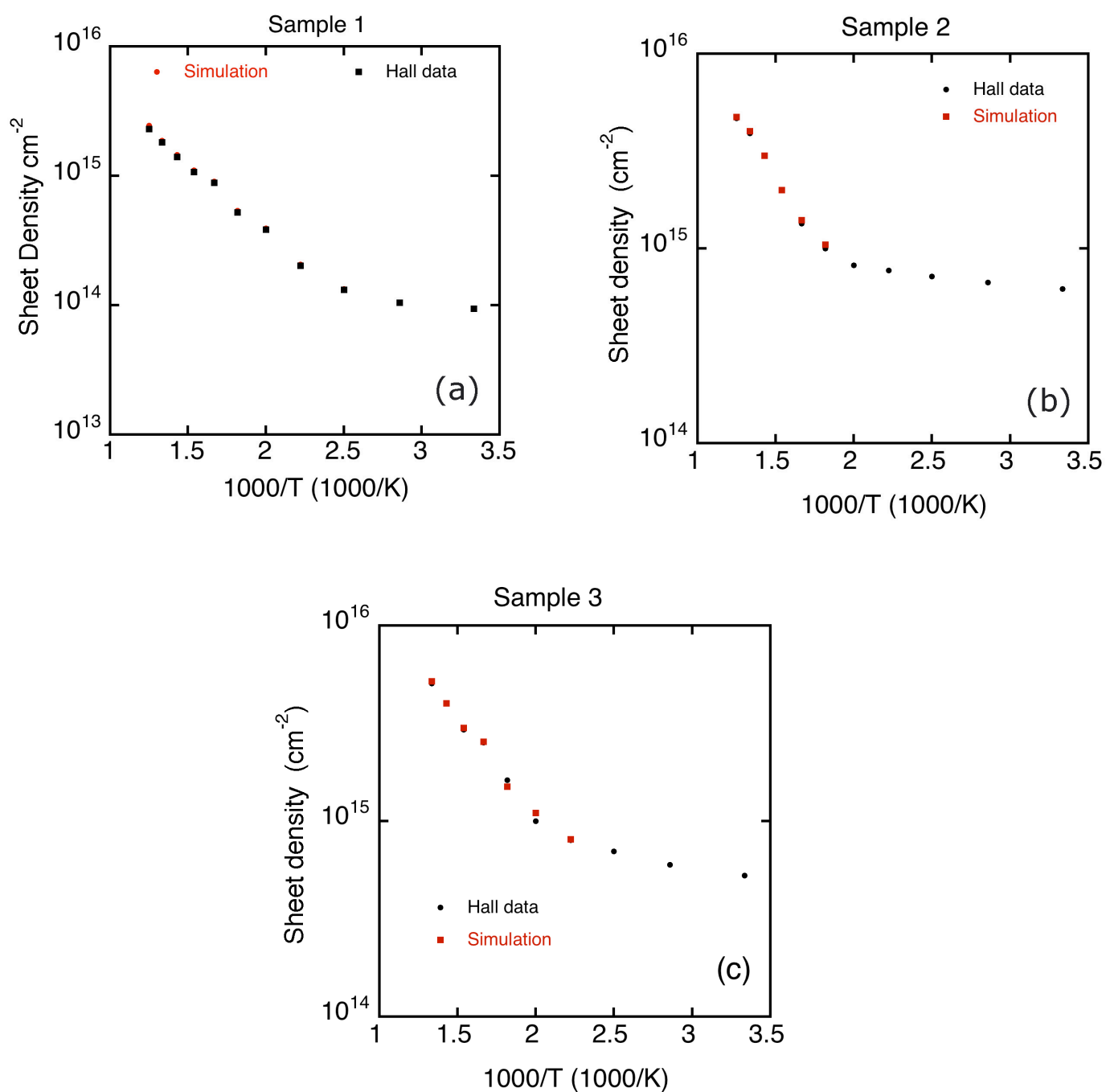
Figures 5.6(a)-(c): Experimental and simulated P values (sheet density) for given values of N_D (see table 5.2) for samples 1-3.

It is well established in conventional semiconductor systems that ionised impurity scattering dominates observed carrier mobility values at low temperatures, whilst phonon scattering controls high temperature mobilities [16]. When carriers are moving relatively slowly (low T regime) the change in mobility is expected to follow a $T^{1.5}$ trend, whilst at higher temperatures, the influence of thermal acoustic phonons is likely to lead to a variation according to $T^{-1.5}$. Such classical behaviour has rarely been seen in diamond films. For example, Tsubota et al [17] prepared boron-doped (100) homoepitaxial films using microwave-plasma CVD identifying a $T^{2.8}$ relationship for mobility between 200 and 300K, with a $T^{-2.8}$ relationship being apparent within the range 300-500K. Whilst offering no explanation for these values, the authors noted the results were consistent with other studies involving both natural type IIb (boron containing) and CVD grown boron doped homoepitaxial films. At low temperatures of 243K, and the extremely low hole concentration of 5 x 10^{12} cm^{-3} (not useful for device applications) a Hall mobility value as high as 2020 cm^2/Vs was recorded. Earlier work by Hatta, Sonoda and Ito [20], again concentrating on homoepitaxial (100) films, found mobility to be dependent upon $T^{-(2.7, -3.1)}$ within the temperature range 300-500K. More recently, Teraji and co-workers [21] grew boron doped (100) homoepitaxial films using a high power density microwave plasma CVD approach. The films showed very low compensation ratios (of the order of 1%) and mobility values that varied with temperature according to $T^{-(1.3, -1.6)}$ at temperatures below 270K, with a value of $T^{-(4.0, -4.5)}$ above this temperature. These curious results were suggested to result from phonon scattering at low temperatures with the reason for the higher temperature result remaining unclear. These observations suggest diamond can behave in a manner that conflicts with established semiconductor theory. Again, high Hall mobility values (2750 cm^2/Vs) were reported for low temperatures (215K) and very low carrier concentrations (3 x 10^{14} cm^{-3}). Wang et al [22] reported a $T^{-3.9}$ dependence on mobility for the entire temperature range 300-800K for

(100) homoepitaxial films with an acceptor concentration of 1×10^{19} cm^{-3} ($N_D \sim 10^{17}$cm^{-3}) and a room temperature Hall mobility of 910cm^2/Vs. This discussion highlights the difficulty in considering the origin of carrier scattering at differing temperatures and different doping regimes, even within the relatively well-studied diamond (100) boron-doped system.

In terms of the (111) system, little is currently known, with Gi and co-workers [13] confining their observations to the temperature range 200-450K, and making no comment on the variation of mobility with temperature. They reported a room temperature mobility value of 364 cm^2/Vs for the very low carrier concentration of 2.9×10^{13} cm^{-3} (again not useful for devices). The compensation ratios determined were high at 3-28%.

In the current case, low compensation ratios have been determined, alongside carrier concentrations and relatively high mobility values, at high temperatures (800K). For example, in the case of sample type 1, (table 5.2) the value for hole mobility peaks at ~20cm^2/Vs (450K) at the (high) carrier concentration of 3×10^{19} cm^{-3}, and only falls to 15cm^2/Vs at 800K, where phonon scattering is expected to reduce the mobility value. Moreover, the lower temperature variation of mobility as $T^{1.3}$ and the higher temperature variation being as $T^{-0.9}$ in this sample is indicative of near-classical conduction within this semiconducting diamond. In sample type 4, the 800K mobility value is rather similar to sample type 1 (14 cm^2/Vs), despite the increase in carrier concentration to 2×10^{20} cm^{-3}, and the peak in mobility value is now at 700K rather than 450K. Indeed, a trend in increasing the temperature for the peak in mobility value is evident through sample types 1-4. This result implies a decrease in the relative effect of phonon scattering compared to ionised impurity scattering as the dopant concentration increases. This is not surprising in itself, but it is surprising that the mobility values remain relatively high for all of these sample types. The observation of valence band conduction at

higher carrier concentrations here compared to (100) boron-doped diamond films is very encouraging for the high temperature operation of diamond devices based around highly boron doped (111) layers, as device operation will not be degraded as severely by high temperatures as would have previously been expected. It can be speculated that the very low compensation levels achieved in these samples are indicative of the very high quality homoepitaxial process that has been achieved. Since compensation is required for hopping conductivity to occur, this result is likely to be the reason that high mobility (valance band conduction) is maintained in sample type 4; in studies of boron-doped diamond (100) the doping level evident in sample type 4 would have already led to the loss of valance band-conduction and the onset of the very low mobility values associated with hopping. In the present case it is only sample type 5 (9 x 10^{20} cm^{-3} holes, table 5.2) that displays the (low) mobility values indicating the onset of carrier hopping (1.5 cm^2/Vs).

5.5 Conclusions

High quality homoepitaxial films have been grown on type 1b (111) single crystal diamonds. Tri-methyl boron (TMB) has been used to introduce boron as a substitutional dopant species during the homoepitaxial growth process, with free carrier (holes) concentrations as high as 2 x 10^{20} cm^{-3} whilst maintaining (valance) band conduction displaying mobilities of the order of 14 cm^2/Vs. These high values are thought to arise through delaying the onset of hopping conductivity within these films, due to the extremely low compensation levels observed for these films. Only at carrier concentrations measured as high as 9 x 10^{20} cm^{-3} does the mobility collapse to values of 1.5 cm^2/Vs. Interestingly, the mobility values in these films are not strongly degraded by increasing temperatures, with the maximum values of mobility in some films actually occurring at 700K.

These results are very promising for the potential application of highly boron doped (111) homoepitaxial diamond layers for high temperature device applications. It is clear that the ultra-pure gases used for growth in the current instance and the growth parameters used can lead to very high quality doped diamond. The integration of these types of layers with more lightly phosphorus doped diamond (111) epitaxial layers can be seen to be an essential step towards the realisation of bipolar devices from diamond for high temperature device applications.

5.6 References

1. AT Collins and AWS Williams, J. Phys. C: Sol. State Phys., 4 1789 (1971).
2. RC Burns, V Cvetkovic, CV Dodge, DJF Evans, MLT Rooney, PM Spear and CM Welbourn, J. Cryst. Growth, 104 257 (1990).
3. N Fujimori, H Nakahata and T Imai, Jap. J. Appl. Phys., 29 824 (1990)
4. H Shiomi, Y Nishibayashi, N Fujimori, Jap. J. Appl. Phys., 30 1363 (1991).
5. SA Grot, CW Hatfield, G Sh Gildenblat, AR Badzian and T Badzian, Appl. Phys. Letts., 58 1542 (1991).
6. EP Visser, GJ Bauhuis, G Janssen, W Vollenberg, WJP Van Enckevort and LJ Giling, J. Phys.: Cond. Mat., 4 7365 (1992).
7. TH Borst and O Weis, Phys. Stat. Sol., (a) 154 423 (1996).
8. B. I. Shklovskii and A. L. Efros, in: Electronic Properties of Doped Semiconductors, Ed. M. Cardona, Springer-Verlag, Berlin 1984.
9. S Sonoda, JH Won, H Yagi, A Hatta, T Ito and A Hiraki, Appl. Phys. Letts., 70 2574 (1997).
10. JP Lagrange, A Deneuville and E Gheeraert, Carbon 37 807 (1999).
11. S.Koizumi, H.Ozaki, M.Kamo, Y.Sato and T.Inuzuka Appl. Phys. Lett., 71 1065 (1997).

12. M Katagiri, J Isoya, S Koizumi and H Kanda, Appl. Phys. Letts., 85 6365 (2004).

13. SG Ri, H Kato, M Ogura, H Watanabe, T Makino, S Yamasaki and H Okushi, Diam. & Relat. Mat., 14 1964 (2005).

14. B Baral, SSM Chan and RB Jackman, J. Vac. Sci. Technol. A 14, 2303 (1996).

15. A. Tajani, C. Tavares, M. Wade, C. Baron, E. Gheeraert, E. Bustarret, S. Koizumi, D. Araujo, Physica Status Solidi (a), 201 2462 (2004).

16. A. Miller and E. Abrahams, Phys. Rev. 120, 745 (1960).

17. T Tsubota, T Fukui, T Saito, K Kusakabe, S Morooka and H Maeda, Diam. & Relat. Mat., 9 1362 (2000).

18. RF Mamin and T Inushima, Physical Review B, 63 033201 (2001).

19. C Wang, M Irie, K Kimura, T Teraji, T Ito, Jap. J. Appl. Phys., 40 4145 (2001).

20. A Hatta, S Sonoda and T Ito, Diam. & Relat. Mater., 8 1470 (1999).

21. T Teraji, H Wada, M Yamamoto, K Arima and T Ito, Diam. & Relat. Mat., 15 602 (2006).

22. C Wang, M Irie, K Kimura, T Teraji, T Ito, Jap. J. Appl. Phys., 40 4145 (2001).

Chapter 6: An Impedance spectroscopic investigation of the electrical properties of δ-doped diamond structures

6.1 Introduction

6.2 Experimental methods

6.3 Results

6.4 Discussion

6.5 Conclusions

6.6 References

6.1   Introduction

The potential of diamond as a semiconductor for the realisation of high frequency and high power transistors has been recognised for many years [1]. The emergence of microwave plasma-enhanced chemical vapour deposition (CVD) for the growth of high quality single crystal diamond layers [2] has led to material with electronic properties that surpass those of the best natural diamonds. Electron and hole mobilities have been reported as high as 4500 and 3800 cm^2/Vs respectively [3]. Progress in the use of this type of material for the fabrication of high frequency devices has recently been reviewed [4]. Whilst problems relating to the growth of high quality diamond layers can be considered broadly solved, effective doping remains an issue. Boron can be routinely introduced during the CVD process creating acceptor states that display an activation energy of some 0.37eV [5]; at room temperature few boron atoms will be active resulting in poor electrical characteristics. At high boron concentrations an impurity band begins to form, leading to a very low (meV) activation energy, but conduction then occurs through 'hopping' leading to very low hole mobility values [5]. A possible solution to this problem is to use the concept of δ-doping that has been widely used within III-V semiconductor technology [6]. This involves the formation of very thin,

highly doped regions within a homostructure. Provided the doped, or δ, layer is only a few atom layers thick, carriers will move in a region close to, but outside, this layer. The resultant separation between carriers and the donor or acceptor atoms that created them leads to enhanced mobility. From a quantum perspective the δ-layer distribution must be less than the free carrier de Broglie wavelength ($\lambda = \dfrac{h}{p}$, where h is Planck's constant and p is momentum).
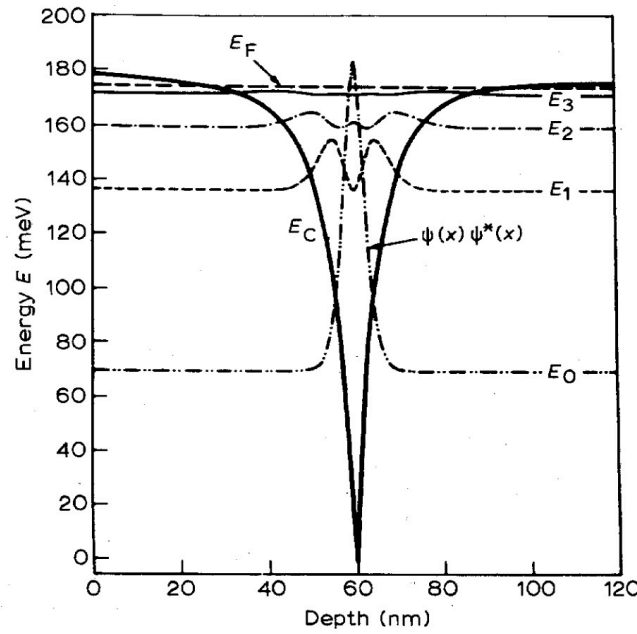
Figure 6.1 (a): Self-consistently calculated sub-band energies and wave-functions of δ-doped GaAs with a sheet donor concentration of $5.0 \times 10^{12} \text{cm}^{-2}$ (from Schubert *et al.* (from [6]). The δ-doped layer here is 60nm below the surface.
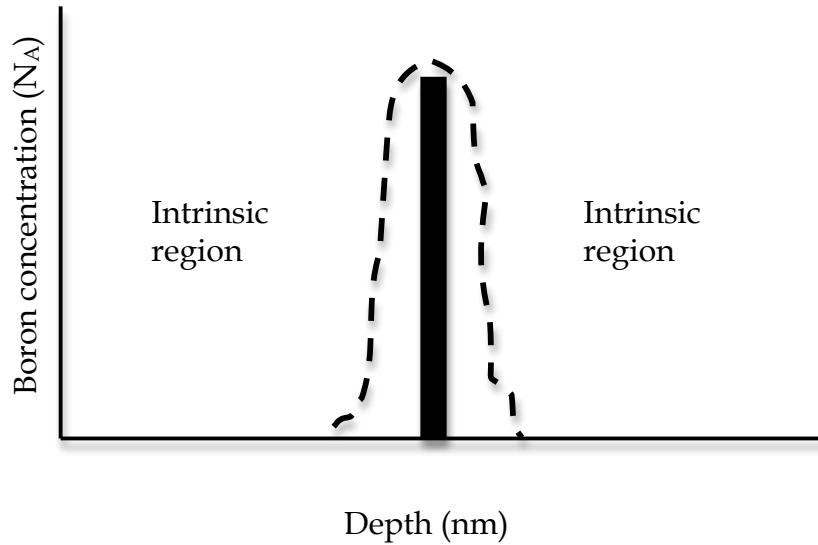
Figure 6.1(b): An ideal δ-doped (solid line) and an actual δ-doped profile (dashed line) grown by CVD methods for a capped δ-doped structure (from [6]).

Figure 6.1 (a) shows the variation of electrostatic potential with distance away from a δ-doped plane of donor atoms. If the width of this V-shaped potential well is comparable to the free carrier de Broglie wavelength, this will result in a quantization of the allowed electron (or hole) energies, as indicated in figure 6.1(a). Also shown is the square of the wavefunction amplitude of the electrons corresponding to each confined state. This quantity determines the charge distribution of the free carriers. The wavefunction of the electrons (or holes) in the lowest sub-band have a peak at the delta plane resulting in strong carrier scattering originating from the ionized impurities in the δ-doped layer. In the second band, the wavefunction as seen in figure 6.1 (a) exhibits a node at the delta-plane and peaks ~ 3nm either side. The spatial separation of free carriers and ionized impurities reduces the strength of the scattering resulting in a much higher mobility for this band. As the sub-band index increases so does the spatial extent of the wavefunction, further reducing the strength of ionized impurity scattering. This, however, has a

limiting effect on carrier mobility. As sub-bands in k-space continue to be filled, eventually the donor or acceptor ions in the δ-layer lose all of their scattering influence after a certain index, only for surface scattering to begin to take effect causing the mobility to decrease.

Since the δ-layer is ideally heavily doped, in the case of diamond the problem associated with the otherwise high activation energy is overcome, with the prospect of high mobility hole transport outside of the δ-layer itself. This idea was initially considered by Kobayashi and co-workers [7], and has been explored by a number of groups since [8-21].

Kunze *et al* [15] used CVD to grow a 6nm (FWHM) thick δ-layer onto a type Ib synthetic diamond crystal coated with a 500nm CVD grown intrinsic buffer layer. The δ-layer was capped with a 100nm intrinsic layer. The delta layer in this case was grown using a solid boron source, inserted into the plasma for a short period of 5 s. The growth conditions for the buffer diamond layer (1.5% CH_4 in H_2 at a total pressure of 30 Torr) in this case were determined by the growth conditions for the narrow delta-layer in order to avoid growth interruptions whilst the growth temperature was maintained at 650 °C. This low growth temperature was chosen in order obtain a narrow doping profile due to smaller growth rates at lower temperatures (5 nm/minute) [15]. After the insertion of the solid boron source into the plasma a growth interrupt was performed to remove residual boron from the chamber involving a 30 s "outgrowth" time (microwave plasma turned off) and then the CH_4 flow was turned of, allowing diamond growth for 2 minutes using the residual CH_4 in the growth chamber at 750 °C (11nm/min). Electrical measurements using a cyclic etch-measure approach indicated that the boron concentration within the δ-layer was > 10^{19} cm^{-3}, as is desirable for reduction of the activation energy of the dopant [5]. However, sufficient dopant existed in the capping layer to prevent these structures being useful for field-effect transistor (FET) applications, as channel modulation would not be possible. An activation

energy of 180meV at temperatures above 170K was attributed to conduction within the cap, with a low temperature activation energy of ~3meV being considered to arise from the δ-layer itself. Conduction activated with an E_a of 1.5eV was ascribed to the buffer layer. In later work [17] the same group formed δ-layers with a FWHM of ~1nm. Here, they manually inserted the boron rod for 2 s into a hydrogen plasma with no methane content. This was followed by a growth step of 3 s, with a dilute H_2/CH_4 pulse. Then the plasma was switched off and the gas mixture evacuated. Following this growth interrupt the chamber was filled with a H_2/CH_4 gas mixture to grow a nominally undoped capping layer of 1nm. The chemical boron profiles of these samples were analyzed using the high resolution elastic recoil detection method. Residual boron was detected in the capping layer on top of this 1.1nm δ-layer making these diamond layers less attractive for electronic applications for reasons stated previously.
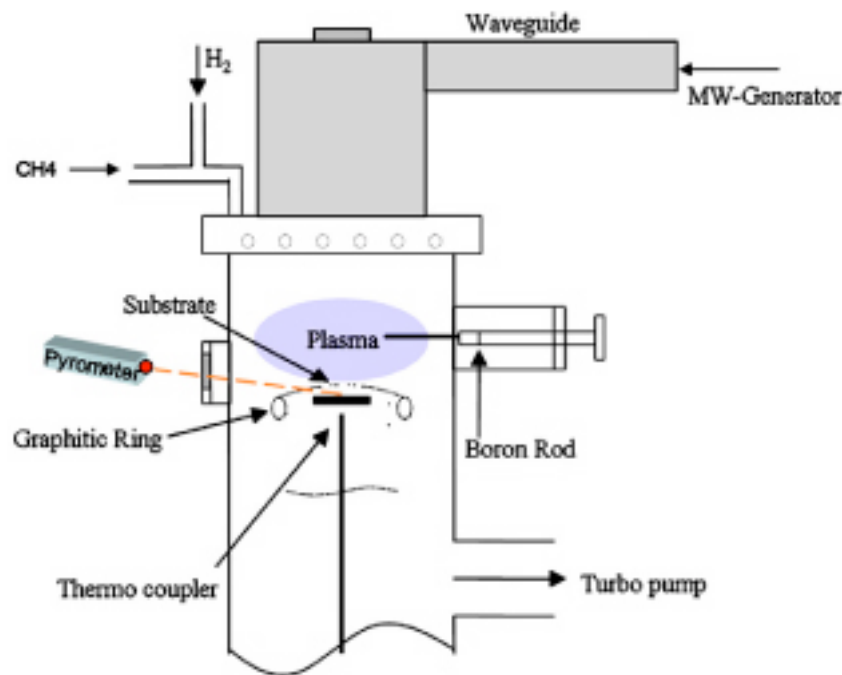
Figure 6.2(a): Schematic showing a simplified version of the MPCVD system used to grow δ-layers (from [15]).

El-Hajj and co-workers [20] used electrochemical profiling in an attempt to

investigate the nature of electrical conduction within similar δ-layers. This enabled them to determine a free carrier value of 10^{21} cm^3, in good agreement with the δ-layer boron concentration. The reported Hall mobility values, at 20-30cm^2/Vs, are far lower than those expected for an ideal δ-structure, indicating that carrier transport is still largely confined to the δ-layer itself. It is clear that a much greater insight into the nature of electrical conduction within these complex diamond δ-layers is required if they are to be optimised for use within high frequency FET applications. This chapter shows that impedance spectroscopy (IS) is capable of distinguishing differing conduction paths within δ-based diamond structures. A number of samples are studied here, enabling considerable insight into the nature of the conduction processes occurring to be achieved.

6.2   Experimental methods

The Element Six laboratory, Kings Ride Park, Ascot, Berkshire, UK, supplied the samples studied here. Microwave plasma-enhanced CVD was used to produce both intrinsic and boron-doped layers on type Ib synthetic single crystal diamond samples. The buffer layer was grown with a methane concentration of approximately 0.3% in hydrogen at a pressure of 2.5 kPa. The thickness was 100 nm. The growth was then interrupted, and the boron δ-doped layer was then grown by maintaining a background pressure, of boron, whilst pulsing CH_4/H_2 into the chamber for no longer than 5 seconds. This procedure consists of a sequence of gas flow pulses controlled and timed by mass flow controllers and computerized valves. Finally, an intrinsic cap layer (nominally undoped) of 20 nm was grown on top of the δ-doped profile in a separate MPECVD system to avoid residual background boron doping the intrinsic diamond layers. SIMS analysis showed the δ-layer to have a boron concentration of ~5 x 10^{20} atoms cm^{-3}. Prior to analysis all samples were subjected to wet chemical treatments that are known to leave the surface free from organic contaminants and in a strongly oxidised state [23], avoiding so-

called 'surface conductivity' [24]. Au contacts were evaporated onto the top surface of the samples, which were then placed inside a stainless steel vacuum chamber providing both atmospheric control and electrical shielding during analysis. A heater within the chamber enabled measurements to be obtained within the temperature range 300-673K. To ensure thermal stability samples were annealed in air at 673K (1 hour) before measurements were performed. In addition some samples were subjected to 1123K anneal in an N_2 flowing ambient (20 minutes) followed by a repeat of the wet chemical treatment. Table 6.1 gives details of the sample set that has been studied here.

Sample No	δ-layer thickness (FWHM)	Capping layer thickness
δ-1	5nm	None
δ-2	3.2nm	None
δ-3	5nm	15-20nm
δ-4	3.2nm	15-20nm

Table 6.1: Samples studied; all δ-layers are grown on a 100nm intrinsic layer supported on a type Ib synthetic diamond substrate. The δ-layer in each case is boron doped, with $N_A \sim 5 \times 10^{20}$ cm^{-3}.

Impedance spectroscopy is a powerful technique that can be used to characterise the electrical properties of materials and their interfaces with electrically conducting electrodes. The technique measures the impedance as a function of applied frequency; a typical 'Cole-Cole' representation has the real component of the impedance plotted against the imaginary component. This results in a semicircular response, where the RC characteristics of the impedance can be determined by fitting a RC parallel circuit model to the data. The impedance equation for a RC parallel circuit model is as follows:

$$Z_{RC} = \frac{R_1}{1 + \omega^2 C_1^2 R_1^2} - \frac{j\omega C_1 R_1^2}{1 + \omega^2 C_1^2 R_1^2} \tag{6.1}$$

In the case of a material that supports multiple conduction paths a number of semicircles may be seen, often overlaying each other meaning that careful fitting of the data to ideal semicircles is required to extract useful information [25]. This technique has been useful deployed previously for studying electrical conduction in both single crystal and nanocrystalline diamond films [26-29]. In the experiments described here measurements were performed with a Solartron SI1260 instrument fitted with a high input impedance module 1296, operating in the range 0.1Hz-10MHz. All measurements were performed as a function of temperature, such that the activation energy for each conduction path observed could be determined. To confirm that experimental observations do not relate to the type Ib substrate underlying the δ-structures impedance measurements were obtained for a Ib crystal alone; the resistance remained considerably greater than that recorded for all epitaxial samples measured (at greater than 10^9 Ohm) over the full temperature range.

Probe 1   Probe 2

Au contact   Sample   Au contact

Heater
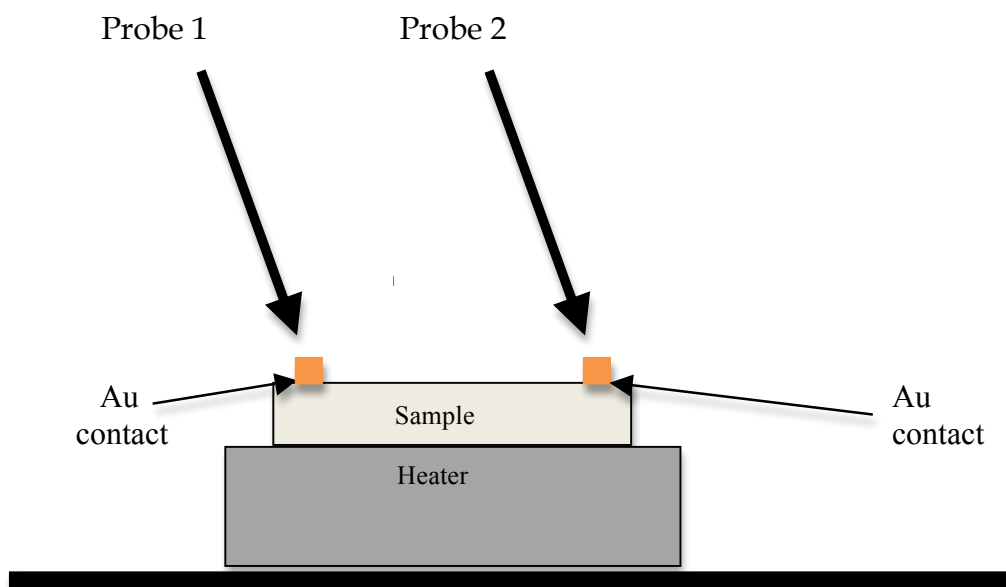
Figure 6.2(b): Schematic of experimental setup for impedance spectroscopic measurements. Distance between Au contacts was kept at 2.5mm for all samples measurements.

6.3 Results

6.3.1 Uncapped samples δ-1 and δ-2

Figure 6.3 (a) and (b) shows the measured data in Cole-Cole plot format for sample δ-1, recorded at temperatures within the range 300K – 673K. The distorted form of the semicircular response seen here is indicative of partially resolved overlapping semicircles; a higher and a lower frequency component are present. The fact that the plots for the different temperatures broadly overlay each other indicates little variation in resistance over the measured temperature range. Figure 6.3(c) shows the Cole-Cole plot measured after annealing sample δ-1 at 1123K. This plot is significantly different to those seen in figure 6.3 (a) & (b). It is now only possible to see a single semicircular response, and the data sets obtained at different temperatures do not overlay each other. Intriguingly, as the temperature increases to 423K the diameter of the semicircles reduces, indicative of a reduction in resistance, but as the temperature rises to 473K the semicircle grows in magnitude once again. These trends were reproducible over several temperature cycles. Fitting the data contained within figures 6.3(a) - (c) enables the resistance to be determined for the various components as a function of temperature; from these values Arrhenius plots can be constructed as shown in figures 6.3(d) and (f) for sample δ-1 before and after the 1123K anneal treatment two almost constant resistance trends are seen corresponding to individual low and high frequency semicircular responses and are labelled as trends R_1 & R_2 respectively (as is the case for all samples throughout this study). In the case of figure 6.3(d) R_1 yields an E_a of 8meV whilst no fit could be obtained from R_2. The single semicircular response seen following the 1123K treatment (figure 6.3(e)) can be seen to give rise to both 28meV and a 0.33eV activation energy regime. The Cole-Cole plots for uncapped sample δ-2 were qualitatively very similar to those for uncapped sample δ-1 (fig. 6.4(a) and (b)); the Arrhenius plot taken from the measured data for sample δ-2 is shown in figure 6.4(d) and

(e), again showing two resistance paths, both data trends display metallic conductivity. However, a major difference between the samples was noted following the 1123K anneal treatment of uncapped sample δ-1, whereas uncapped sample δ-2 remained virtually unchanged (figure 6.4(e))
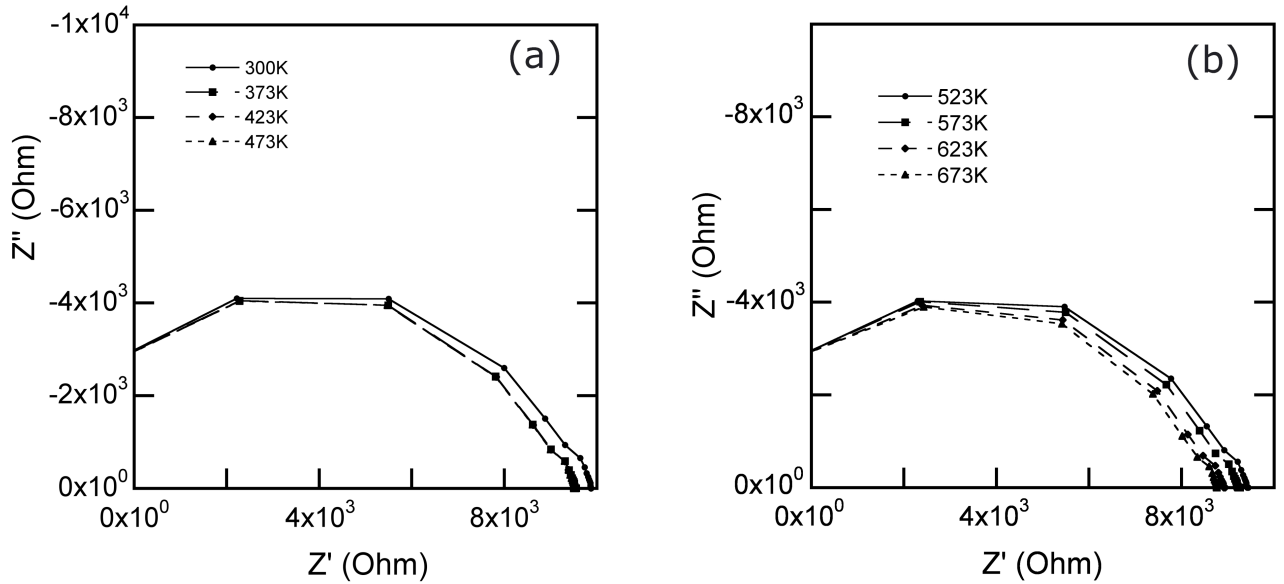
Figure 6.3 (a) and (b): Cole-Cole plots for uncapped sample δ-1 after 673K anneal in air.
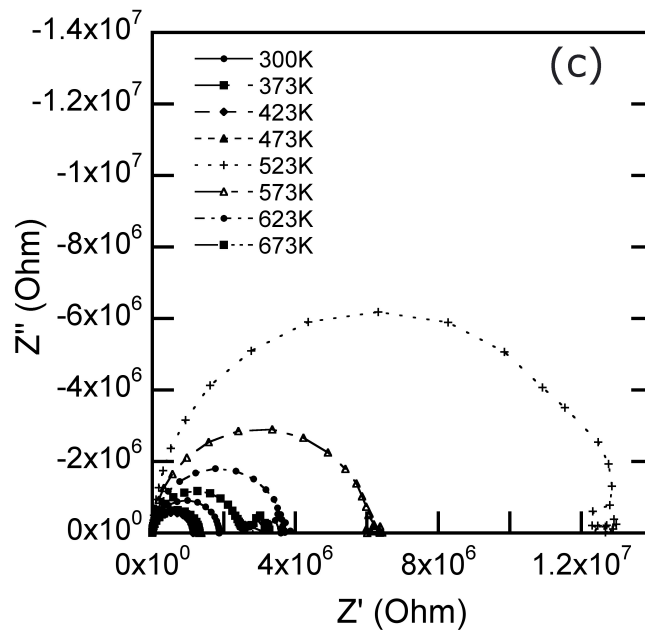
Figure 6.3 (c): Cole-Cole plots after 1123K anneal in a flowing N_2 ambient.
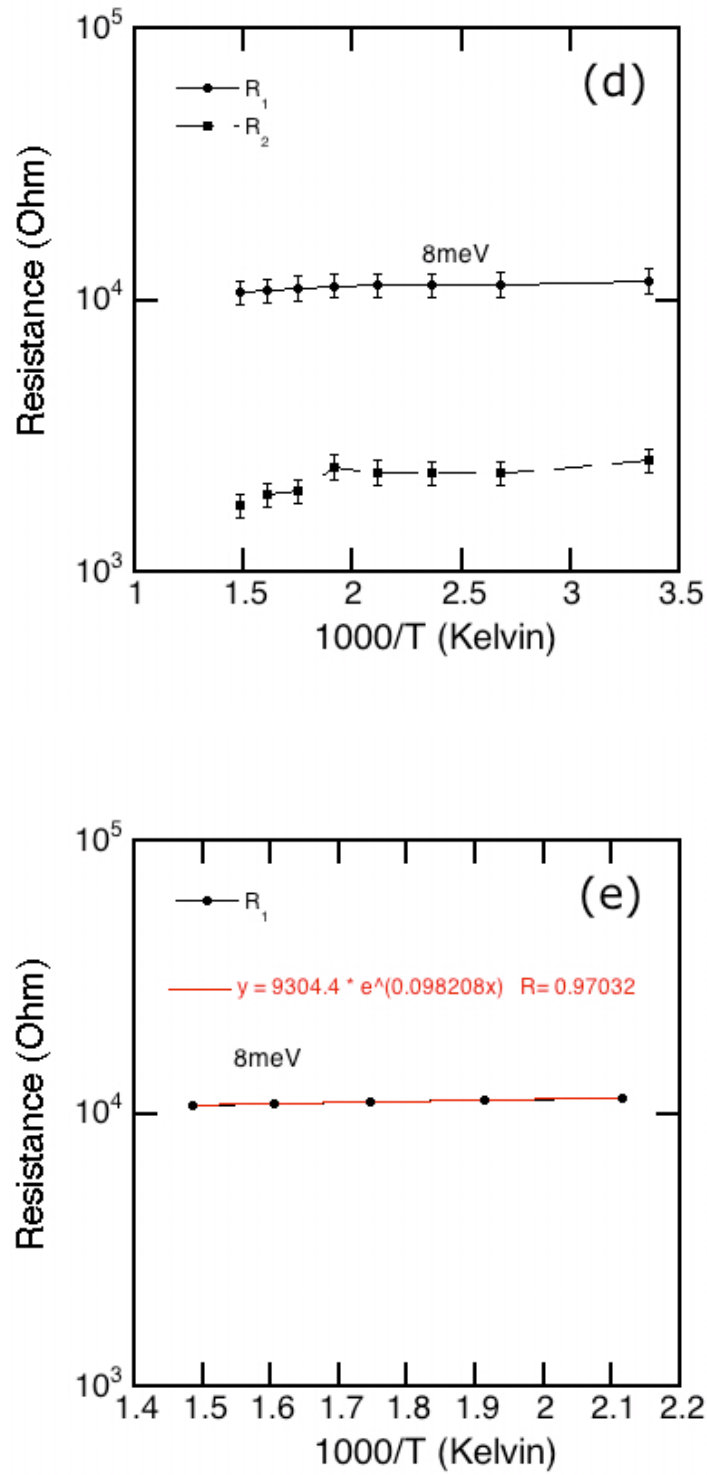
Figure 6.3 (d) & (e): Arrhenius plots displaying the modeled resistance against 1000/T for uncapped sample δ-1 after 673K anneal in air (d) and (e) Arrhenius fits to data.
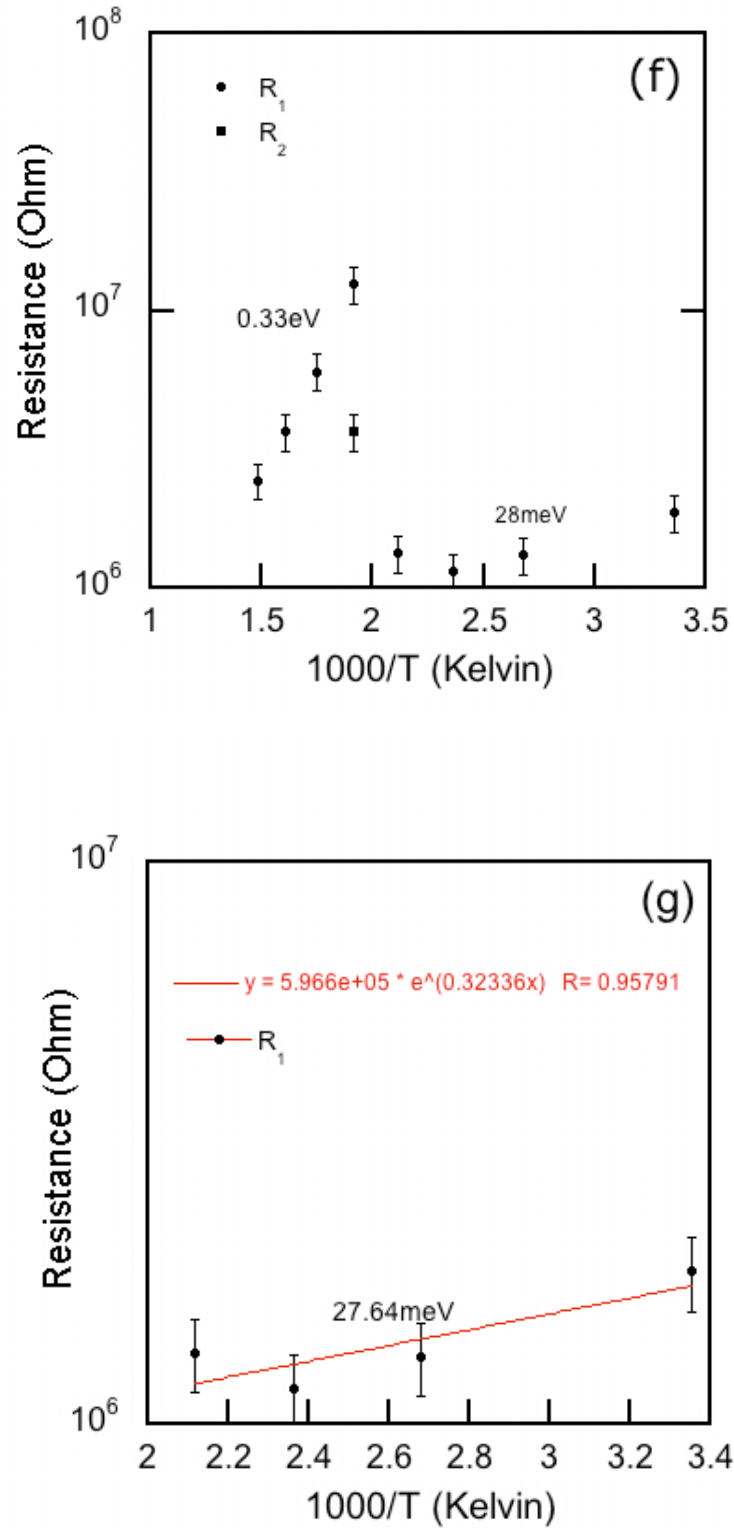
Figure 6.3 (f) & (g): Arrhenius plots displaying the modeled resistance against 1000/T for uncapped sample δ-1 after 1123K anneal in air (f) and (g) Arrhenius fits to data (low temperature region).
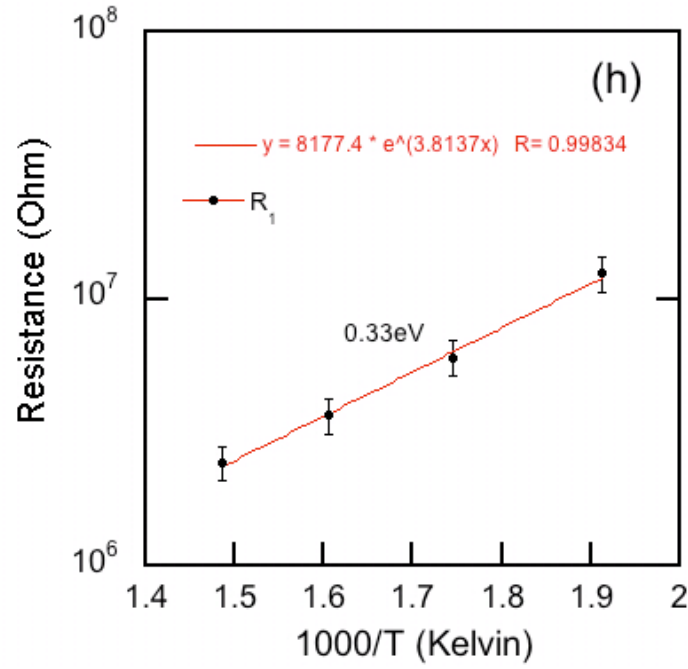
Figure 6.3 (h): Arrhenius fit to experimental data for sample δ-1 after 1123K anneal in air (high temperature region).
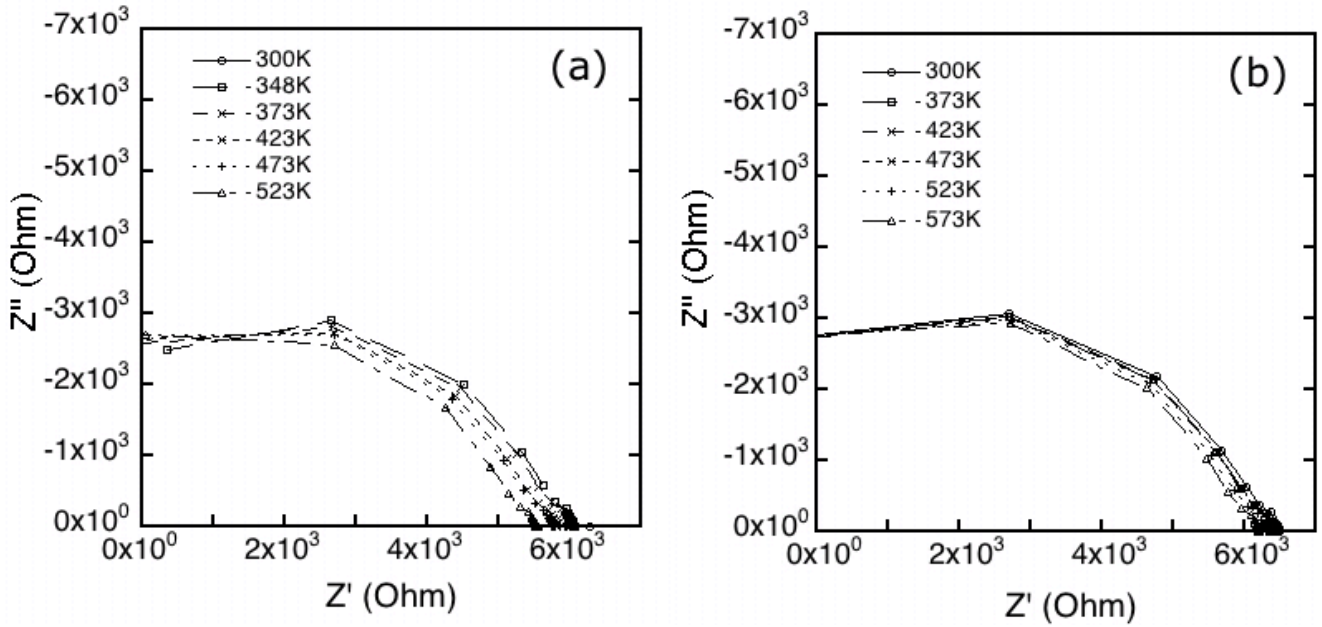
Figure 6.4 (a) & (b): Cole-Cole plots for uncapped sample δ-2 after annealing at (a) 673K (in air) and (b) 1123K in a flowing N_2 ambient.
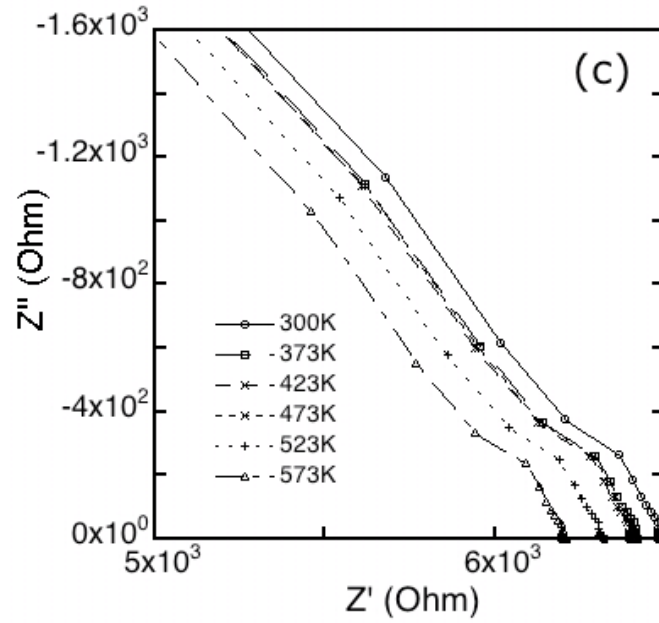
Figure 6.4 (c): Cole-Cole plot for uncapped sample δ-2 after annealing at 1123K; this overlapping semicircular response is observed in the low frequency range of the spectrum.
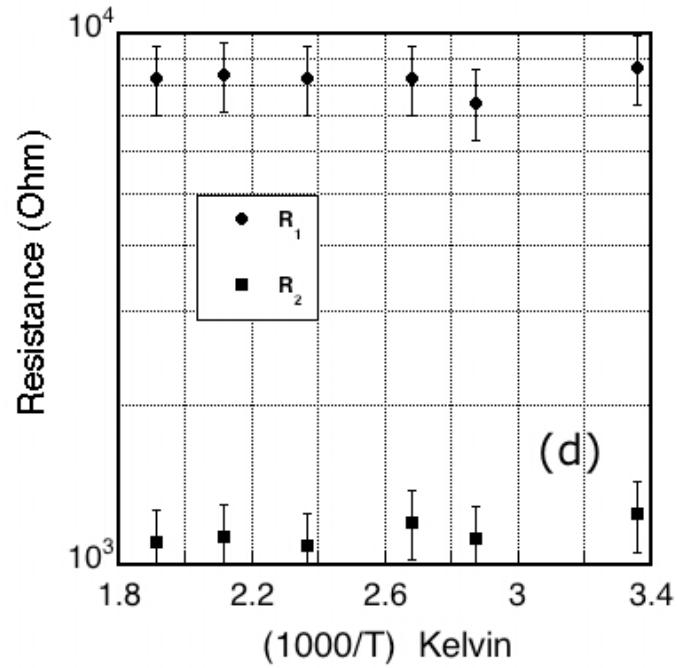
Figure 6.4 (d): Arrhenius plot for uncapped sample δ-2, before 673K anneal treatment
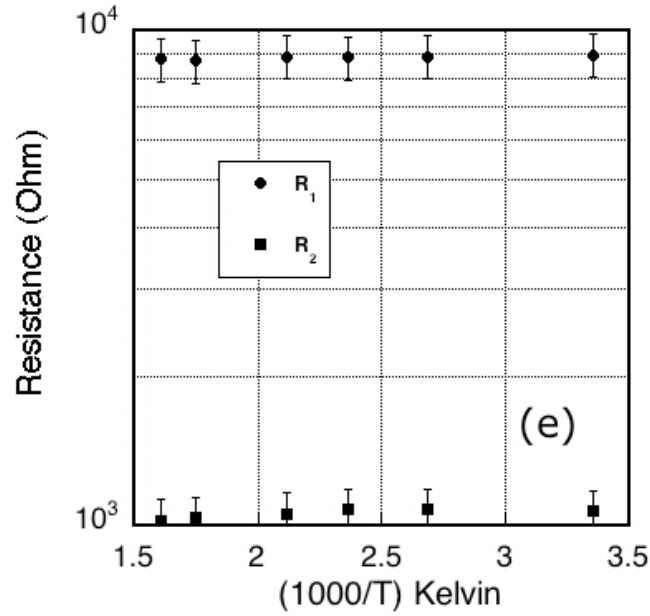
Figure 6.4 (e): Arrhenius plot for uncapped sample δ-2 after 1123K anneal treatment.

6.3.2 Capped samples δ-3 and δ-4

Cole-Cole plots are shown for capped sample δ-3 (after 1123K anneal treatment) in figures 6.5(a)-(i). Complex behaviour is apparent. Inspection of figure 6.5(a) reveals the presence of two semicircular responses (a lower resistance semicircular response is present, see figure 6.5(e)), whilst in figure 6.5(b) the situation is clearly somewhat more complicated once the temperature has increased. First, inspection of the values on the axes shows that the film has become *more resistive* as the temperature increases to 373K. Further, the shape of the response has altered. Moreover, impedance measurements for a temperature of 423K show a further increase in resistance values and a rather dramatic change in the shape of the graph (figure 6.5(b)). Also shown in figure 6.5(b) are the measurements obtained for a temperature of 473K. Intriguingly, the impedance values are now *lower* than those for 373K and 423K, so the sample now becomes *less resistive* as the temperature further increases. This trend is maintained until 673K. Careful fitting to these data sets

reveals the presence of two semicircular responses at each temperature increment with a third being observed at temperatures of 373K and 523K. Figure 6.5(g) shows the Arrhenius plot obtained from the modeling of the semicircular responses observed from within the respective Cole-Cole plots; two distinct E_a's of 0.25eV and 1.75eV are determined here. R_1 displays metallic like behavior.
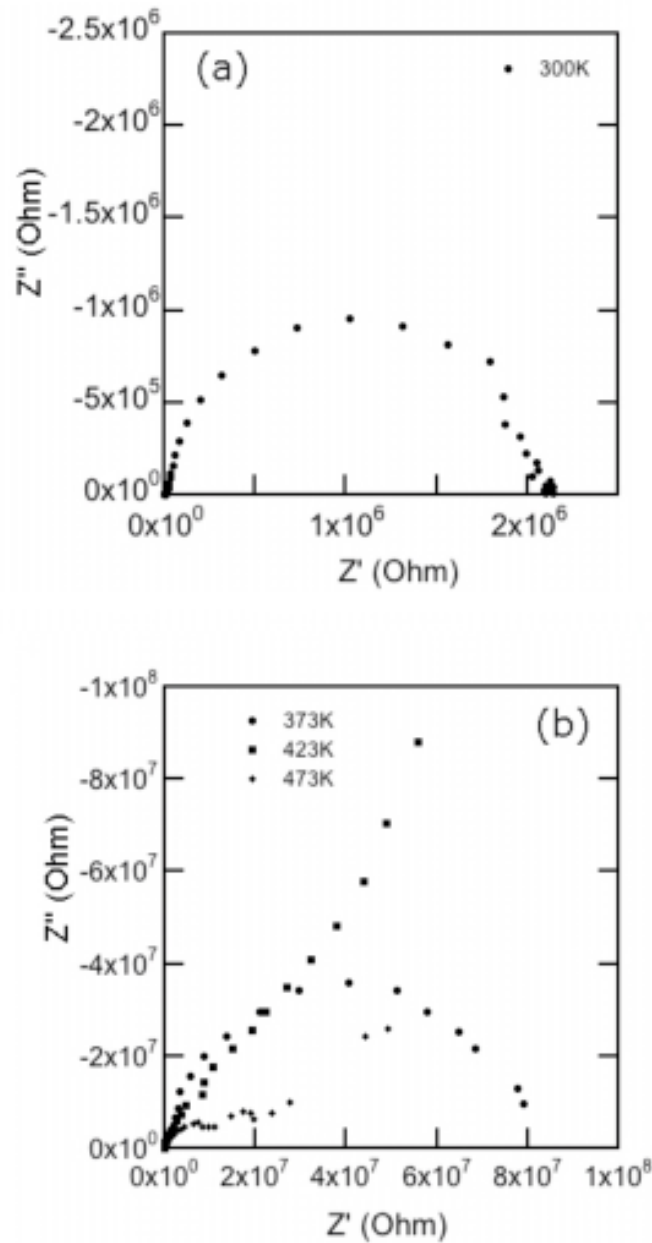
Figure 6.5 (a) & (b): Cole-Cole plots for capped sample δ-3 (after 1123K anneal treatment) at (a) room temperature and (b) 373K- 473K.
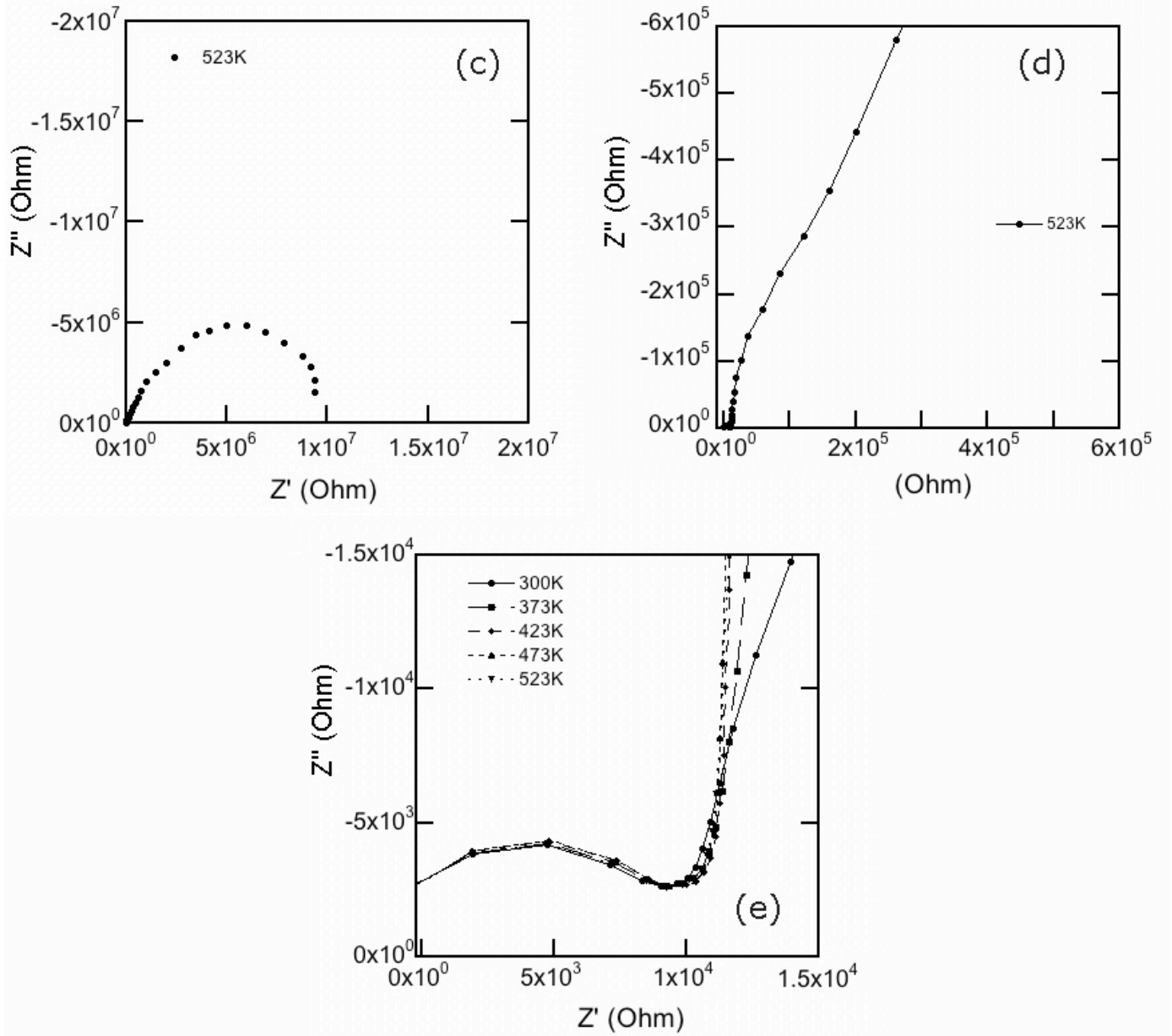
Figure 6.5 (c) - (e): Overlaying semicircular responses, representing differing conduction pathways that exist for capped sample δ-3 (after 1123K anneal) at 523K. Figure 6.5(e) shows a third semicircle present at high frequencies. This semicircular response is observed over the entire measured temperature range for capped sample δ-3 (see figure 6.5 (f)).
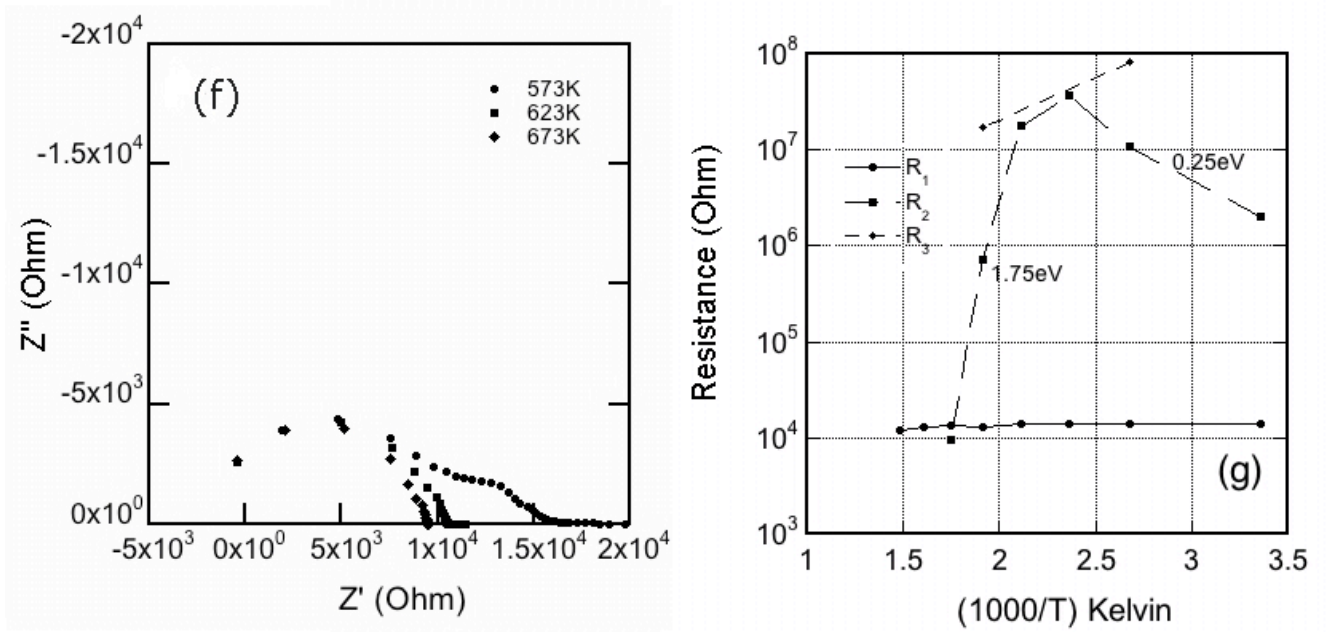
Figure 6.5 (f) & (g): Cole-Cole plot displaying semicircular responses (f) for capped sample δ-3 from 573-673K, and Arrhenius plot (g) displays the modelled resistance over the measured temperature range plotted against 1000/T.
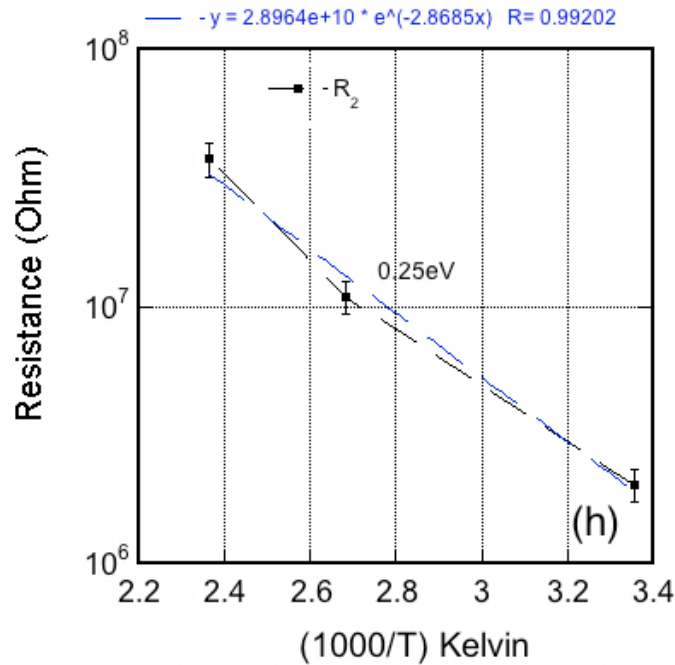
Figure 6.5 (h) Arrhenius fit to experimental data for sample δ-3 after 1123K anneal in air (low temperature region).

133
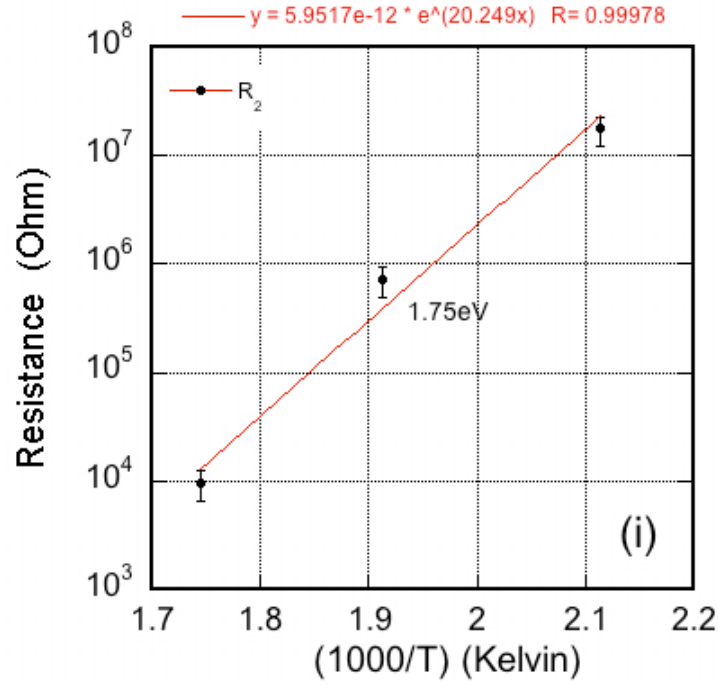
Figure 6.5 (i) Arrhenius fit to experimental data for sample δ-3 after 1123K anneal in air (high temperature region).

Cole-Cole plots demonstrating the electrical behavior of capped sample δ-4 are shown in figures 6.6(a)-(d) and 6.7(a)-(e) before and after 1123K anneal treatment. Careful fitting to this data reveals three semicircular components emerging at differing temperatures. Visual inspection of fig. 6.6 and fig. 6.7 indicates strong changes following the annealing treatment; this is borne out in the Arrhenius plots for both data sets shown in figure 6.6(e) and 6.7 (f) respectively. Before annealing three states with activation energies of 5meV, 0.2eV and 0.21eV are apparent, whilst a single E_a of 0.25eV is apparent after. R_1 now displays metallic like characteristics and insufficient data points are available to determine the activation energy of R_3 (third state).
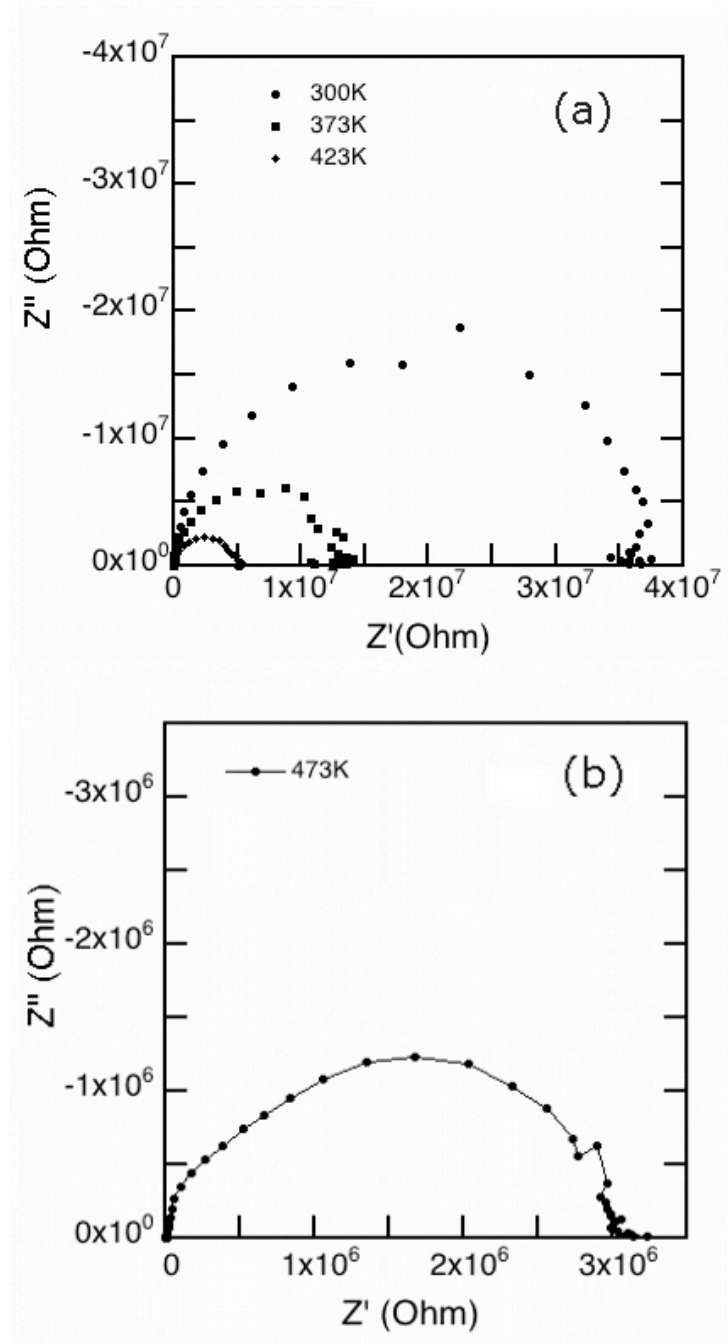
Figure 6.6 (a) & (b): Overlaying Cole-Cole plots from 300-473K for capped sample δ-4 after annealing at 673K.
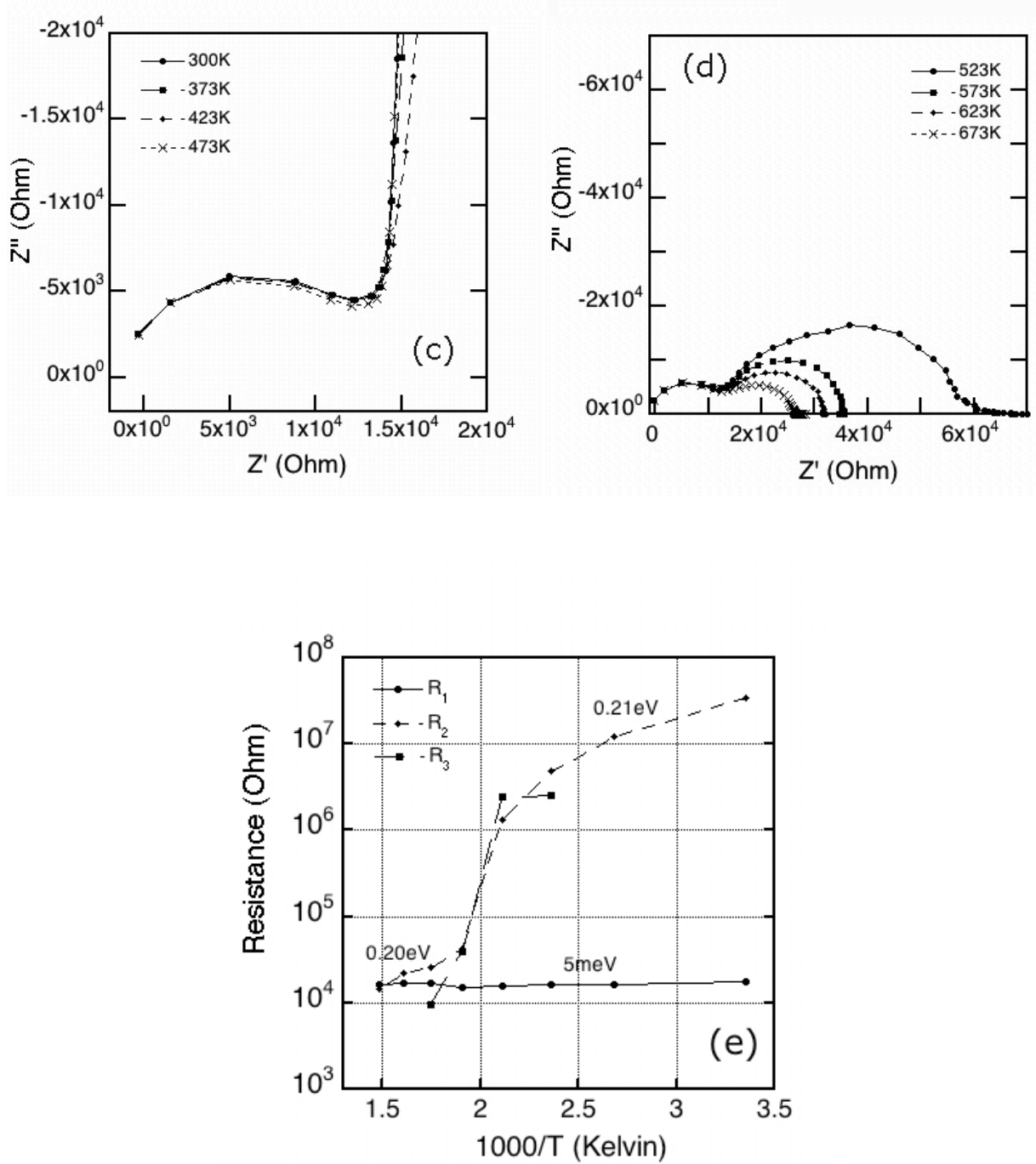
Figure 6.6 (c) - (e): Cole-Cole plots displaying (c) the presence of a single semicircular response at lower resistances (high frequency range) from 300-473K and (d) overlaying semicircular responses 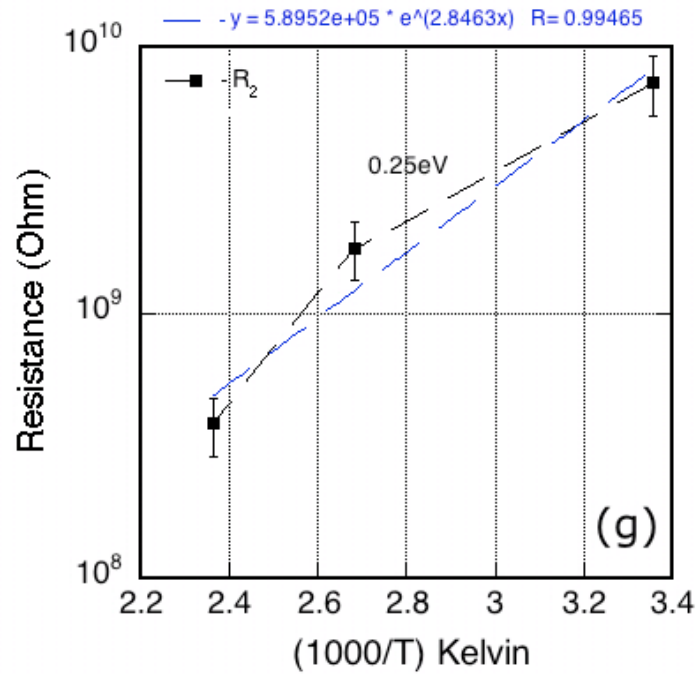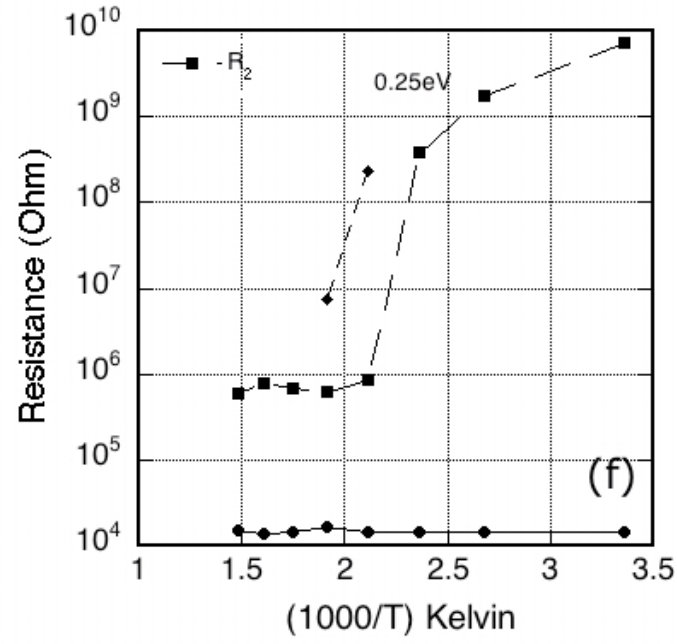from 523-673K after 673K anneal in air. An Arrhenius plot is shown in (e), documenting the individual resistance trends for the activated conduction pathways as a function of temperature for capped sample δ-4.
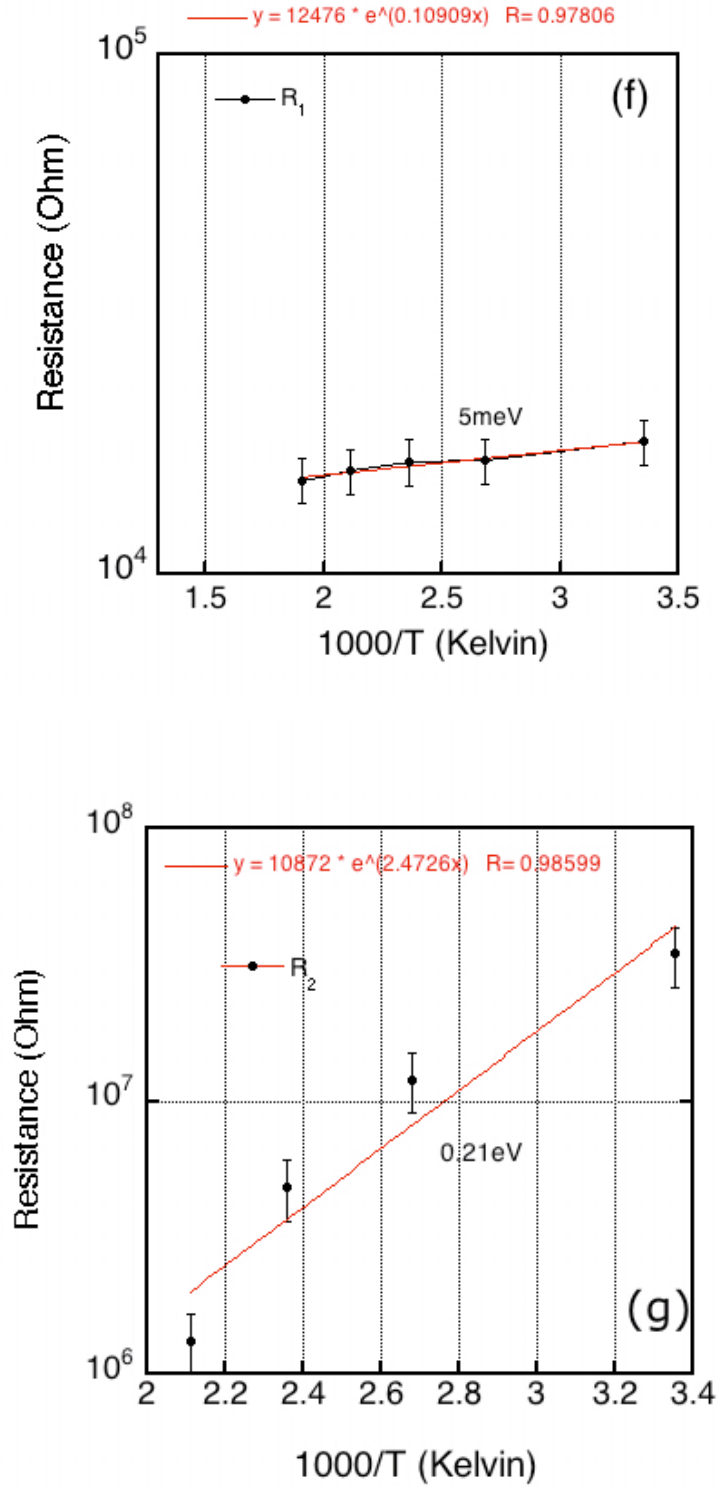
Figure 6.6 (f) & (g): Arrhenius fits to experimental data for sample δ-4 after 673K anneal in air for R_1 (f) and R_2 (g).
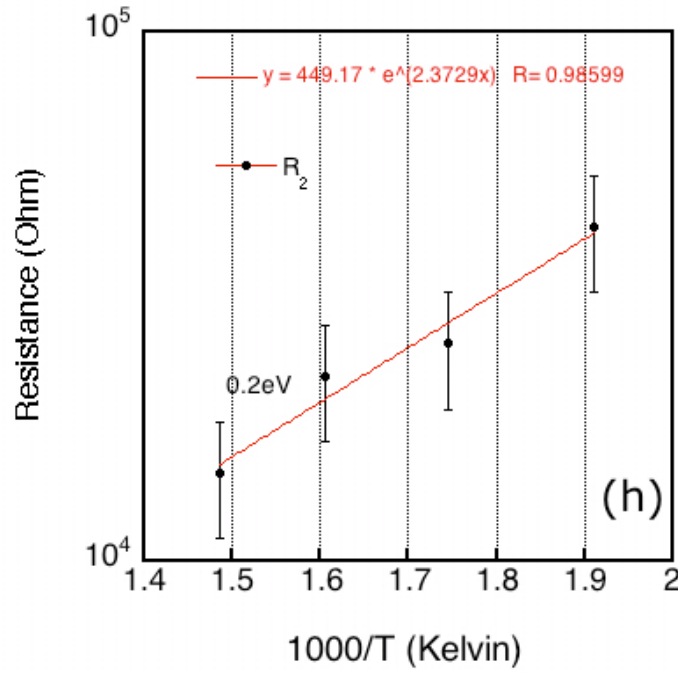
Figure 6.6 (h): Arrhenius fit to R$_2$ experimental data for sample δ-4 after 673K anneal in air.
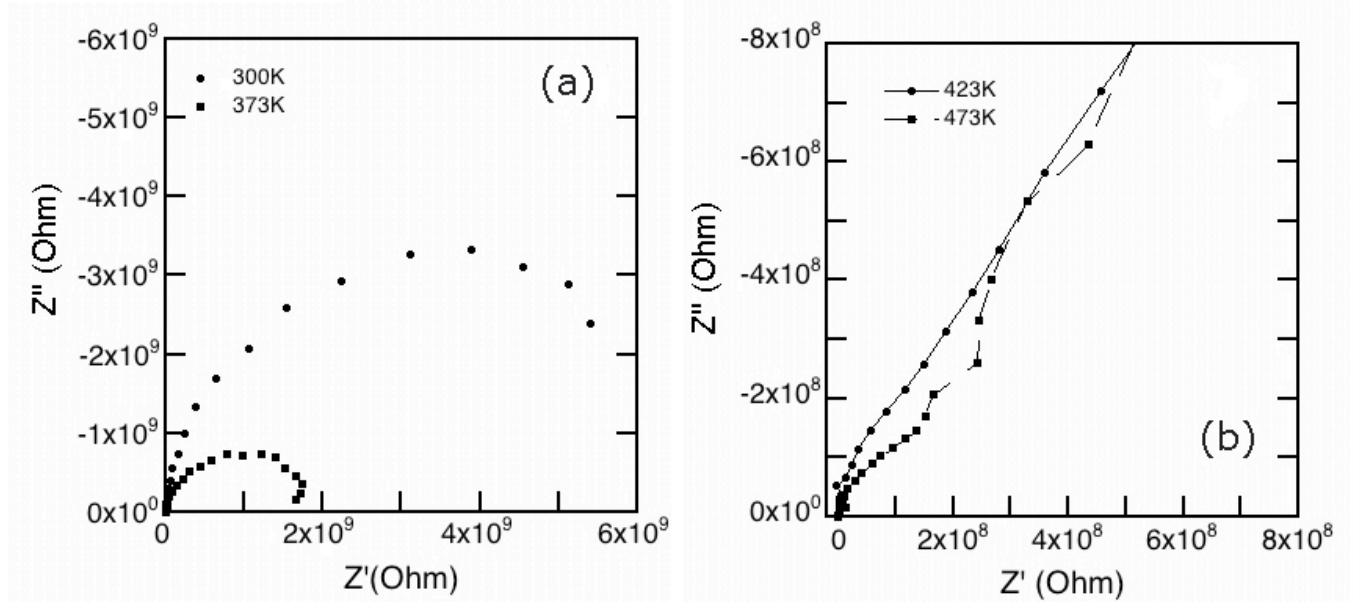
Figure 6.7 (a) & (b): Cole-Cole plots revealing overlaying semicircular responses from 300–473K for capped sample δ-4 after 1123K annealing treatment (see figure 6.7 (h) & (i)).
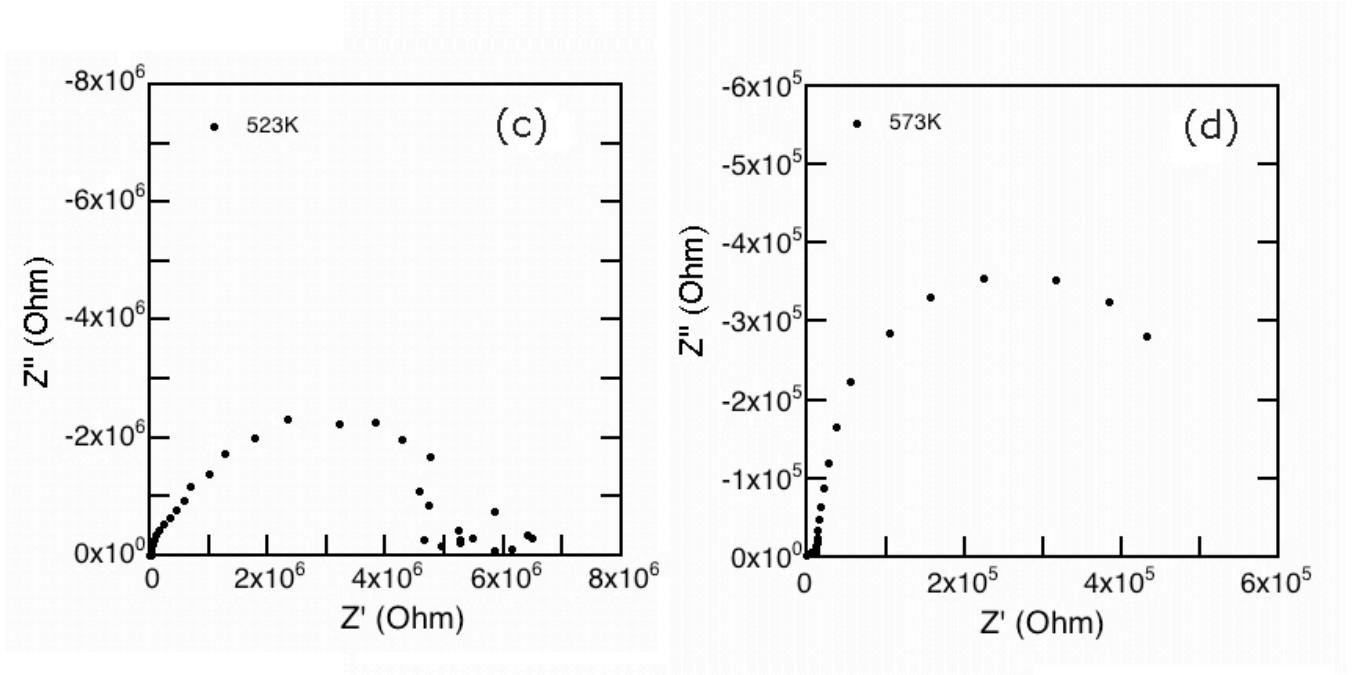
Figure 6.7 (c) & (d): Cole-Cole plots revealing overlaying semicircular responses from 523-573K for capped sample δ-4 after 1123K annealing treatment.
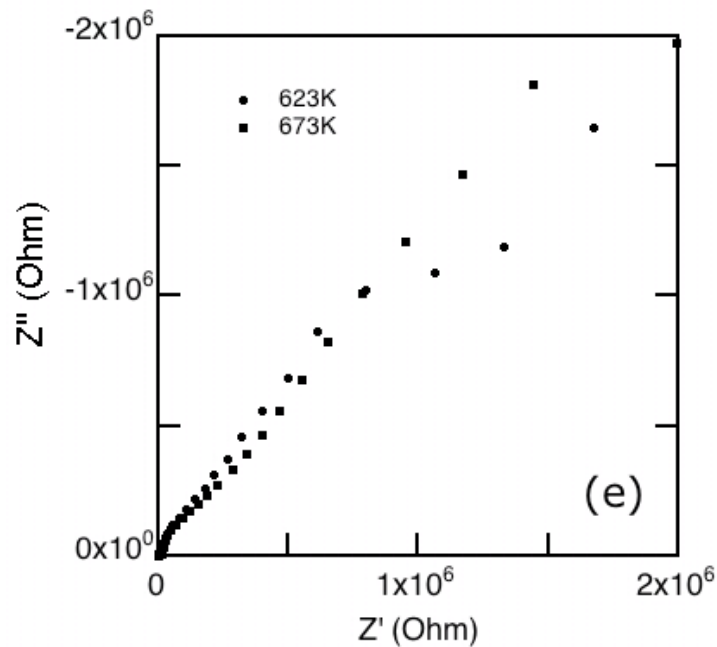
Figure 6.7 (e) Cole-Cole plot displaying semicircular responses from 623-673K (after 1123K treatment).

Figure 6.7 (f) & (g): Arrhenius plot (f) showing the individual resistance trends for the activated conduction pathways as a function of temperature for capped sample δ-4 (after 1123K treatment) and (g) Arrhenius fit to experimental data.
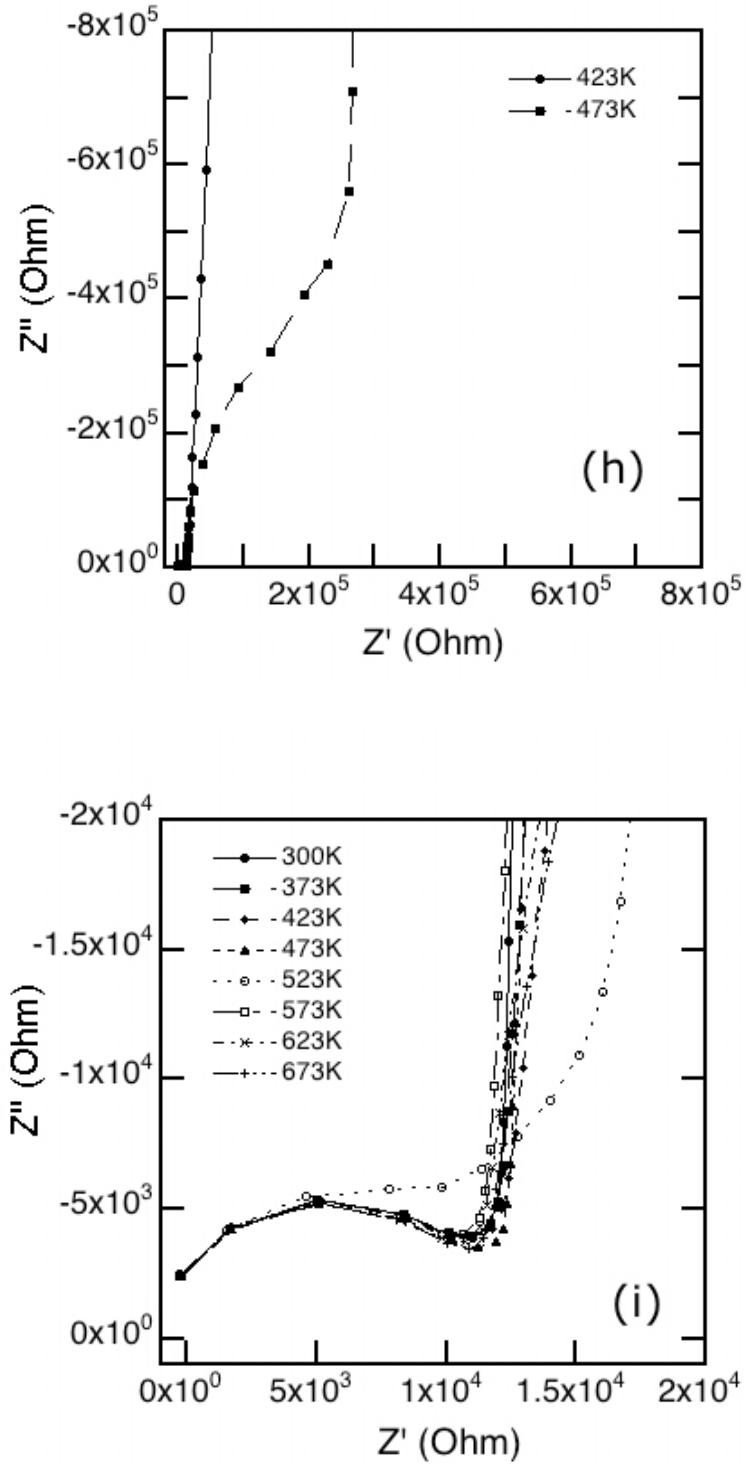
Figure 6.7 (h) & (i): Cole-Cole plots revealing overlaying semicircular responses at lower resistances (high frequency range) for capped sample δ-4 (after 1123K treatment) between (h) 423–473K and (i) 300-673K.

6.4 Discussion

6.4.1 Uncapped samples δ-1 and δ-2

It is apparent that both uncapped structures initially display similar electrical characteristics (figures 6.3(d) and 6.4(d)); that is, two conduction pathways one with a lower resistance than the other. R_1 can be seen to have an average resistance of ~7 x 10^3 Ohm with R_2 displaying an average resistance of ~1 x 10^3 Ohm. This is a promising result, as the less resistive path in this structure may be the result of conduction through a region where the carriers have a higher mobility. Little thermal activation is observed here, with values seen to be in 5-30meV range, in agreement with the known semi-metallic properties expected for the boron concentration in the diamond δ-layer [5]. R_1 can most probably be attributed to conduction in the boron δ-doped layer itself where the mobility is expected to be low; that this is indeed the case becomes more evident later in this chapter. The possible association of conduction path R_2 with a higher mobility state due to its lower resistivity could indicate carrier transport may be arising through movement outside of the δ-doped region. The modelled capacitance values observed here are in the pF range, indicative of transport through highly ordered crystalline material [25].

Annealing samples δ-1 & δ-2 at 1123K produces some rather interesting behaviour. The electrical properties of sample δ-1 (figure 6.3(f)) are substantially altered, with δ-2 remaining unchanged (figure 6.4(e)). For sample δ-1 the two overlaying semicircular responses observed initially disappear only to be replaced by a single semicircle. An increase in resistance of 2-3 orders of magnitude is seen in the respective Arrhenius plots. The modelled capacitance values indicate little change in these structures crystallinity as they remain in the pF range [25]. The recorded increase in resistance must arise through a loss of carriers and/or a reduction in carrier mobility. Figure 6.3(f) displays the Arrhenius plot (after 1123K anneal)

showing at low temperatures a resistance trend with a thermal activation of 28meV and at high temperatures an E_a of 0.33eV is obtained; the latter is comparable to boron's ionisation energy of 0.37eV when present at modest ($<10^{18}$ cm^{-3}) concentrations [5]. The lower temperature thermal activation energy determined here remains in the meV range, as expected for carriers arising from the heavily boron doped δ-layer. It is known that hydrogen is trapped within diamond that is grown using the CVD approach used here [30], and that this hydrogen can passivate boron acceptor states rendering them electrically inactive [31,32]. Hall effect analysis of this sample is presented in chapter 7 (figures 7.1(a)-(c)), here it can be seen that the free carrier density has fallen by one order of magnitude following 873K annealing (over the measured range). It is therefore possible to suggest that in the current case the annealing treatment is leading to the activation of previously inactive hydrogen related deep traps such that these traps may now charge and lead to a reduction in the number of free carriers in the diamond. That the annealing step makes no significant change to the activation data recorded for sample δ-2 suggests that the concentration profile in this sample is much more abrupt, and the two conduction paths observed, are most likely associated with the δ-layer itself and transport outside of it, are thermally stable.

6.4.2 Capped samples δ-3 and δ-4

Sample δ-3 has been characterised following 1123K annealing (figure 6.5(g)) and clearly displays more complex electrical behavior since three semicircular responses are now seen at differing temperatures. The lowest resistance path R_1 displays metallic behavior, it possible to assign this conduction path to the δ-layer itself, where the high doping level is expected to lead to metallic properties [5]. A higher resistance trend, R_2, displays an E_a value of ~0.25eV at lower temperatures, with the resistance *increasing* as the temperature initially *increases*, before the resistance sharply *declines* as the temperatures is further

increased, with an activation energy of some 1.75eV. The resistance of R_3 exhibits similar behaviour but not enough data points could be obtained for this to be properly analysed. This resistance trend indicates that thermally activated defects and trap states are influencing the transport properties of this capped δ-layer structure. The capacitance values derived from the RC parallel circuit model give valuable insight into the electrical behaviour of these different conduction paths. The capacitance values associated with R_1 are found to be in the pF range, indicative of high quality crystalline material [25] and are associated with conduction in the δ-layer itself. However, the remaining semicircles give rise to strongly different capacitance values of 3×10^{-11}F for R_2 and 3×10^{-10}F– 3×10^{-11}F for R_3 being observed. Such values are typically associated with a greater degree of disorder in the crystal [25-28]. It can therefore be proposed that poor quality interfacial material between the δ-layer and the underlying and capping intrinsic layers is responsible for these conduction paths. In the case of R_2 the conduction is controlled by two activated processes, the first dominating at low temperatures (0.25eV) and the second at high temperatures (1.75eV). The most obvious assignments for these states would be a boron interfacial concentration of ~10^{18} cm^{-3} (0.25eV) alongside a crystal defect (trapping) state (1.75eV). That R_3 displays similar trends (although too few data points exist for extraction of numerical values) may be explained if similar states exist in both interfacial regions, but that the resistance of one differs enough from the other to reveal a separate conduction path. Hence, sample δ-3 supports three conduction paths, one assigned to each of the δ-layer, the interface between the δ-layer and the buffer (i) layer and the interface between the δ-layer and the capping (i) layer. It is perhaps not surprising that conduction in the two interfaces differs given that the interfacial crystal disorder associated with a δ-layer grown on the intrinsic buffer may well differ from that obtained when intrinsic material is grown on to a heavily doped layer.

Sample δ-4 has been characterised before and after 1123K annealing. Once again complex behaviour is apparent. In the case of sample δ-4 before high temperature annealing there is some similarity between the Arrhenius plots for this sample, and sample δ-3 (figs. 6.5(g) and 6.6(e)). However, there is no initial increase followed by a decrease in the resistance as the temperature increases for this sample compared to sample δ-3. The observation of three conduction paths (R_1, R_2 & R_3) throughout the measurement is still evident with R_2 and R_3 being of comparable resistance at room temperature i.e. 10^6 - 10^8 to sample δ-3. The R_1 trend which averages at 10^4 Ohms is again indicative of a semi-metallic conduction process which we know to be the heavily boron doped δ-layer with an E_a of the order of 5meV. Conduction path R_2 at lower temperatures has a thermal activation of 0.21eV and at high temperatures 0.2eV. These values could both be attributed to interfacial boron in the concentration range 10^{17} - 10^{18} cm^{-3}, but states associated with other crystal defects cannot be ruled out. The same trend in the capacitance is seen here as in sample δ-3, with R_1, R_2, and R_3 displaying capacitances in the range of pF, 10^{-11}F and 10^{-10} – 10^{-11}F respectively.

Figure 6.7(f) displays the resistance trends observed following 1123K annealing for sample δ-4. Once again three conduction paths can be identified. However, R_2 now only displays a single activation energy, of 0.25eV; too few data points exist for R_3 to confirm whether this is the case for this conduction path. R_1 displays metallic conductivity (boron δ-doped layer). It is important to consider the material change between samples δ-3 and δ-4; δ-4 has the thinner δ-layer (similar to uncapped δ-2), whilst δ-3 has the thicker layers (similar to uncapped δ-1). In the case of uncapped δ-2, high temperature annealing did not change the nature of the conduction paths being supported, with the two identified states displaying meV activation energies. If it is assumed that the underlying (buffer) layer interface with the δ-layer is similar in both δ-2 and δ-4, then it is possible to assign the 0.25eV state associated with R_2 to be boron in the interface between the δ-layer and the *capping layer* rather

than the interface with the *buffer layer*. This would imply that R_3 would be associated with the interface between the buffer layer and the δ-layer; although the data does not exist for δ-4, the implication from the measurements for δ-2 is that this path will display meV activation energy and is likely to be a high mobility conduction path compared to R_1 which is associated with the δ-layer itself. This idea is further supported by the capacitance values obtained from the RC parallel circuit model for sample δ-4 that are less than 10pF.

Data trends observed in this chapter in some instances display less than ideal fits to the mathematical model and in some cases with too few data points. The induced error in the activation energies determined here, and the influence this has on our understanding of the conduction mechanisms occurring in the study has been taken into consideration in this section.

It is also important to note that the boron concentrations in these films are $\sim 5 \times 10^{20} cm^{-3}$. This is approximately 0.3% of boron in the diamond film. These very high doping levels shall induce significant stress in the boron-doped δ-layer, however it is not expected to be sufficient to result in the formation of grain boundaries as these doping levels are within the solid-solubility rate for diamond thin films [34].

6.4.3 Equivalent circuit models for δ-doped structures

6.4.3.1 Uncapped δ structures

Capacitance values extracted from the single RC parallel circuit used for each conduction pathway were in the pF range.
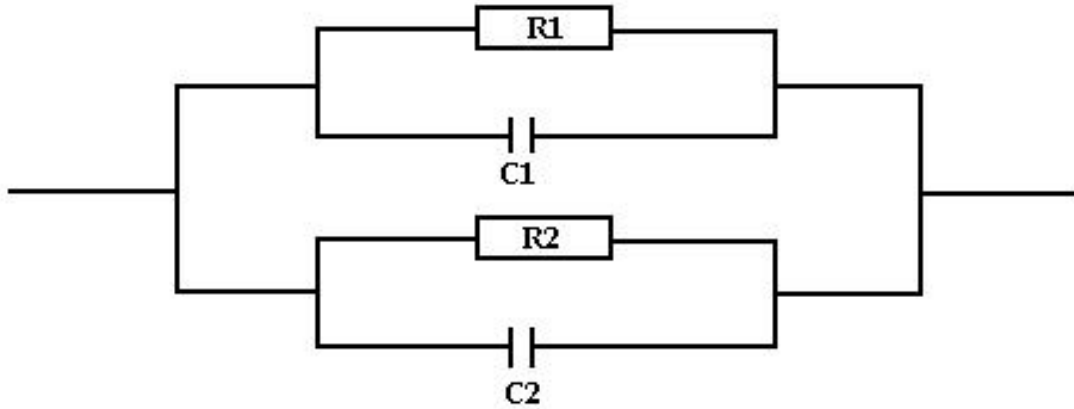

Figure 6.8 (a): RC equivalent circuit of uncapped δ-doped structures.

where R1 is the resistance of the heavily boron δ-doped layer and C1 is the corresponding capacitance. R2 represents the conduction pathway which is believed to occur at the interface between the heavily boron δ-doped layer and the underlying buffer layer (see figure 6.9).

6.4.3.2 Capped δ structures

Modelling of the capped structures is more complex due to added resistance from the intrinsic diamond cap. The dielectric strength of diamond varies with the level of crystallinity, for polycrystalline diamond (electronic grade) the dielectric strength is ~0.4 MV/cm increasing to 4MV/cm for single crystal diamond (depending on quality) [35,36]. Given that the diamond cap here is grown on top of a highly boron-doped layer, it is very likely the induced stress created from the δ-doped substrate yields a polycrystalline/highly disordered diamond cap. The AC potential applied to our samples was $5V_{rms}$ (capping layer thickness between 15-20nm), resulting in a field of 2.5MV/cm. Taking

the field strength into consideration, breakdown of the diamond cap to the δ-doped layer underneath is expected. The following model for carrier transport is therefore proposed:
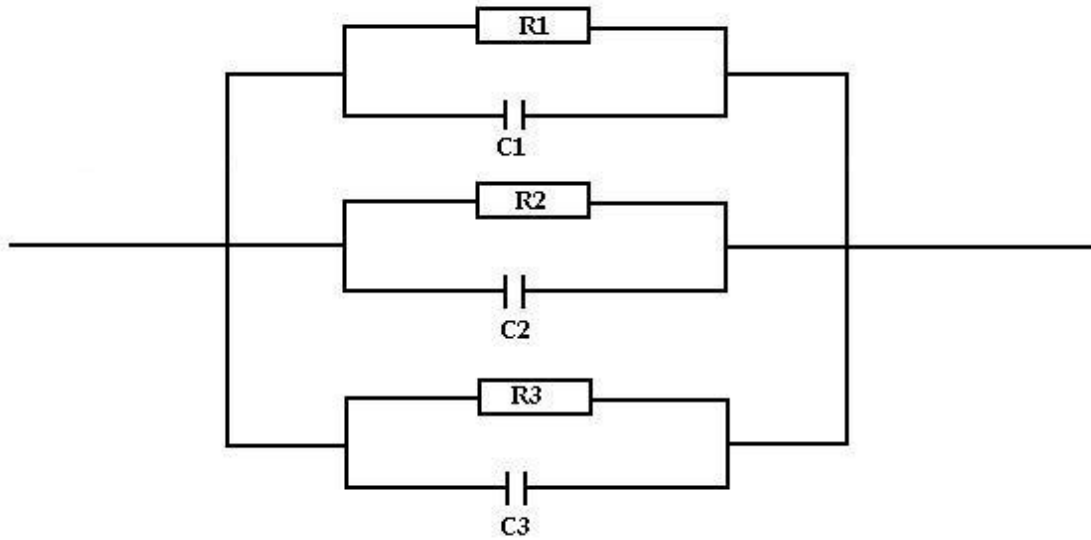

Figure 6.8 (b): RC equivalent circuit of capped δ-doped structures.

where R1 represents the conduction path most likely occurring between the δ-layer and the diamond cap and C1 is the corresponding capacitance. R2 represents conduction through the heavily boron δ-doped layer and C2 is the corresponding capacitance. R3 represents conduction through interfacial region between the heavily boron δ-doped layer and the underlying intrinsic diamond buffer layer and C3 is the corresponding capacitance.
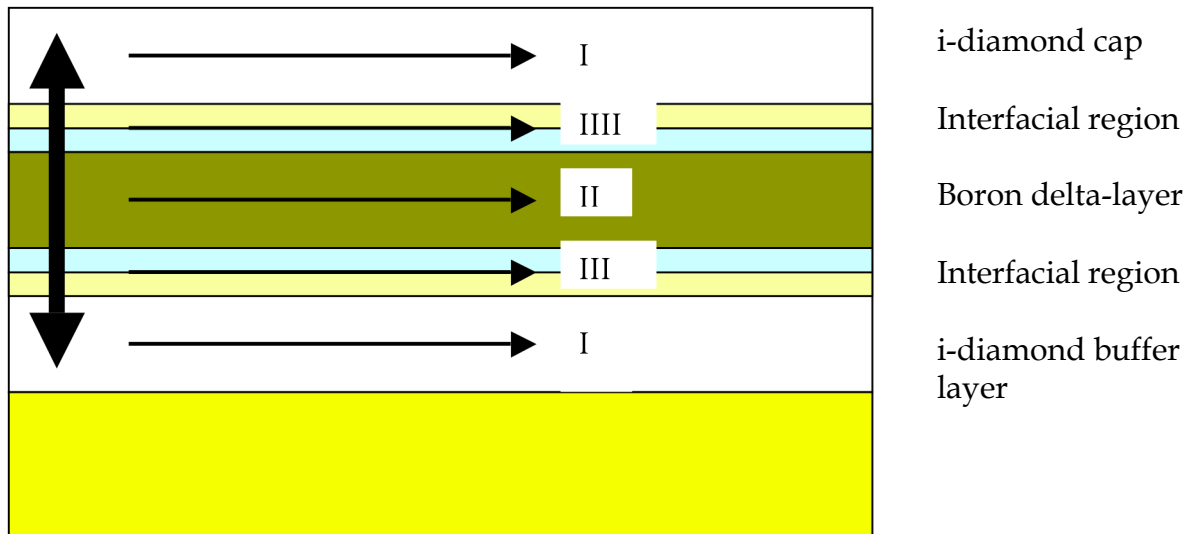
Figure 6.9: Schematic representation of possible conduction paths; carriers emerge from the delta layer but may move under the influence of different crystalline regions. Transport in the i-diamond cap and i-diamond buffer is desirable, as this band transport should result in high carrier mobilities.

6.5 Conclusions

Impedance spectroscopy has clearly shown itself to be a powerful, non-destructive, method for investigating the electrical properties of complex doped diamond structures. In the case of the δ-doped samples studied here, multiple conduction paths have been identified, which can be attributed to conduction within the heavily boron doped δ-layer and the (nominally) intrinsic regions adjacent to the δ-layer. Samples with an intrinsic capping layer have been shown to support three parallel conduction paths, assigned to the δ-layer, and to two differing layers or interfaces between the δ-layer and the underlying buffer and overlying cap. It has been shown that in some δ-doped structures, that boron acceptor states may exist in the interfaces between the intrinsic material and the δ-layer. In the absence of a capping layer, reduction of the δ-layer thickness from 5nm to 3.2nm removed this

interfacial region, presumably though the formation of a more atomically abrupt δ-layer-buffer layer interface. In this case two conduction paths can be identified, both with temperature independent resistance trends. Whilst one of these will clearly relate to the δ-layer, with its expected low mobility, the other most likely arises through transport in the underlying buffer layer, offering the prospect of high mobility transport. When the thinner (3.2nm) δ-layer structure supports a capping layer, a conduction state associated with a region most likely populated with boron at a concentration of ~10^{17} cm^{-3} again arises, assigned to the interfacial region between the capping layer and the δ-layer. . In the absence of a capping layer, reduction of the δ-layer thickness from 5nm to 3.2nm removed this interfacial region, presumably though the formation of a more atomically abrupt δ-layer-buffer layer interface. In this case two conduction paths can be identified, both with temperature independent resistance trends.

In summary, the performance of the 5nm δ-layer structures (δ-1, δ-3) is complex, and most likely dominated by conduction in the interfacial regions between the δ-layer and the intrinsic regions, as well as conduction within the δ-layer itself. In the case of the 3.2nm samples (δ-2, δ-4) the situation appears improved with uncapped samples supporting only two conduction paths, one of which may be associated with high mobility transport outside of the δ-layer, the other low mobility transport within the δ-layer. Introduction of a capping layer creates a conduction path that is assigned to a boron interfacial region between the δ-layer and the cap; improvements to this interface region are required for the optimisation of diamond boron-doped δ-layer structures.

6.6 References

1. R.J. Trew, J-B.Yan and P.M. Mock, Proc. IEEE, 79, 598 (1991).
2. P.W. May, Phil. Trans. R. Soc. Lond. A358, 473 (2000).

3. J. Isberg, J. Hammersberg, E. Johansson, T. Wikstrom, D.J. Twitchen, A.J. Whitehead, S.E. Coe and G.A. Scarsbrook, Science 297, 1670 (2002).

4. R.S. Balmer, I. Friel, S.M. Woolard, C.J.H. Wort, G.A. Scarsbrook, S.E. Coe, H. El- Haj, A. Kaiser, A. Denisenko, E. Kohn and J. Isberg, Phil. Trans. R. Soc. A366, 251 (2008).

5. T.H. Borst and O. Weiss, Physica Status Solidi, A154, 423 (1996).

6. "Delta-doping of Semiconductors" E.F. Schubert (Ed.), (Cambridge University Press, 1996).

7. T. Kobayashi, T. Ariki, M. Iwabuchi, T. Maki, S. Shikama and S. Suzuki, J. Appl. Phys. 76, 1977 (1994).

8. H. Shiomi, Y. Nishibayashi, N. Toda, S. Shikata, IEEE Elect. Dev. Letts., 16, 36 (1995).

9. Y. Ando, T. Ariki, T. Kobayashi, Jpn. J. Appl. Phys. 34 3987 (1995).

10. H. Shiomi and Y. Kumazawa, Dia. Films & Technol., 6, 95 (1996)

11. K.H. Shim and J.T. Lim, Electronics Letts., 32, 1419 (1996)

12. Y. Shirakawa, H. Tanaka, Y. Young, T. Maki, T. Kobayashi, Dia. Films & Technol., 7, 357 (1997).

13. C. Uzan-Saguy, R. Kalish, R. Walker, D.N. Jamieson and S. Prawer, Diam. & Relat. Mater., 7, 1429 (1998)

14. A. Aleksov, A. Vescan, M. Kunze, P. Gluche, W. Ebert, E. Kohn, A. Bergmaier, G. Dollinger. Diam. & Relat. Mater., 8, 941 (1999).

15. M. Kunze , A. Vescan , G. Dollinger , A. Bergmaier , E. Kohn, Carbon, 37, 787 (1999).

16. A. Aleksov, A. Denisenko, M. Kunze, A. Vescan, A. Bergmaier, G. Dollinger, W. Ebert and E. Kohn, Semi. Sci. Technol., 18, S59 (2003).

17. A. Aleksov, M. Kubovic , N. Kaeb , U. Spitzberg , A. Bergmaier , G. Dollinger , Th. Bauer ,M. Schreck , B. Stritzker , E. Kohn, Diam. & Relat. Mater., 12, 391 (2003).

18. A. Denisenko and E. Kohn, Diam. & Relat. Mater., 14, 491 (2005).

19. A. Denisenko , G. Jamornmarn, H. El-Hajj, E. Kohn, Diam. & Relat. Mater., 16, 905 (2007).

20. H. El-Hajj, A. Denisenko, A. Bergmaier, G. Dollinger, M. Kubovic and E Kohn. Diam. & Relat. Mater., 17, 409 (2008).

21. H. El-Hajj, A. Denisenko, A. Bergmaier, G. Dollinger, M. Kubovic, R.S. Balmer and E Kohn. Diam. & Relat. Mater., 17, 1259 (2008).

22. N. Tumilty, J. Welch, H. Ye, R.S. Balmer, C. Wort, R. Lang and R.B. Jackman, Appl. Phys. Letts., 94, 05217 (2009).

23. B. Baral, S.S.M. Chan and R.B. Jackman, J. Vac. Sci. Technol. A 14, 2303 (1996).

24. O.A. Williams and R.B. Jackman, J. Appl. Phys., 96, 3742 (2004).

25. N. Hirose and A. R. West, J. Am. Ceram. Soc. 79, 1633 (1996).

26. H. Ye, O. A. Williams, R. B. Jackman, R. Rudkin, and A. Atkinson, Phys. Status Solidi A-Appl. Res. 193, 462 (2002).

27. HT Ye, RB Jackman, P Hing, J. Appl. Phys., 94, 7878 (2003).

28. HT Ye, O Gaudin, RB Jackman, P Muret, E Gheeraert Phys. Stat. Sol., A199, 92 (2003).

29. S. Curat, H. Ye, O. Gaudin, R.B. Jackman, S. Koizumi, J. Appl. Phys., 98, 073701 (2005).

30. M.I. Landstrass and K.V. Ravi, Appl. Phys. Letts., 55, 975 (1989).

31. M.I. Landstrass and K.V. Ravi, Appl. Phys. Letts., 55, 1391 (1989).

32. J. Chevallier, B. Theys, A. Lusson, C. Grattepain, Physical Review B, 58, 7966 (1998).

33. D. Ballutaud, F. Jomard, J. Le Duigou, B. Theys, J. Chevallier, A. Deneuville and F. Pruvost, Diam. & Relat. Mater., 9, 1171 (2000).

34. H. Umezawa, T. Takenouchi, Y. Takano, K. Kobayashi, M. Nagao, I. Sakaguchi, A. Ishii, Mi. Tachiki, T. Hatano, G. Zhong, Ma. Tachiki, H. Kawarada, Cond-mat/0503303 (2005).

35. H.O. Pierson, Handbook of Carbon, Graphite, Diamond and Fullerenes, Noyes, Park Ridge, NJ (1993).3a. C. Y. Fong, B. M. Klein, in Diamond: electronic properties and applications, edited by Lawrence S. Pan, Don R. Kania Boston: Kluwer Academic , c1995.

36. www.e6.com

Chapter 7: A Hall effect investigation of the electrical properties of δ-doped diamond structures

7.1 Introduction

7.2 Experimental methods

7.3 Results

7.4 Discussion

7.5 Conclusions

7.6 References

7.1 Introduction

A comprehensive introduction to boron δ-doped diamond layers can be read in chapter 6, section 6.1. Arguably, the most important material parameter when comparing the performance of boron δ-doped diamond layers for high power high frequency applications to those established within the III-V semiconductor industry is the carrier mobility and sheet density product. The advantage CVD diamond holds here over other competing delta-doping technologies is that it can routinely doped p-type to very high concentrations (1×10^{21} cm^{-3}) using boron [1]. However, attempting to grow very thin (<5nm) CVD diamond layers is non-trivial, given the growth rates normally associated with CVD diamond. In this chapter Hall effect measurements are performed to evaluate carrier mobility and sheet carrier density characteristics within these δ-doped diamond structures.

7.2 Experimental methods

The samples studied here were supplied by the Element Six laboratory, Kings Ride Park, Ascot, Berkshire, UK. These boron δ-doped diamond layers were grown using a microwave plasma–enhanced CVD reactor. A complete review of the growth conditions and procedures used to grow these δ-doped diamond layers can be found in chapter 6, section 6.2.

Hall-effect analysis was performed using a Lakeshore 7504 Hall system with an Advanced Research Systems helium atmosphere-based closed-cycle refrigerator for low temperature measurements (15-300K), and a Lakeshore evacuated probe system for high temperature measurements (300-800K). The magnetic field was oscillated between −1 and 1 T as the signal was recorded. This aspect of the Hall experiments performed here is particularly important when investigating wide band-gap systems, such as diamond, where significant drift in the background voltage can be encountered during detection of the Hall voltage.

Prior to analysis all samples were subjected to wet chemical cleaning and annealing at 673K in air (1 hour) that are known to leave the surface free from organic contaminants and in a strongly oxidised state [2], avoiding so-called 'surface conductivity' [3]. A second heat cycle is performed at 873K for 20 minutes in a flowing nitrogen ambient in an attempt to improve the electrical characteristics of these structures. In addition, further annealing at 1123K is performed. This data is not presented here as this heat cycle has negligible effect on the electrical characteristics of these boron δ-doped diamond layers.

7.3 Results

7.3.1 Uncapped samples δ-1 and δ-2

Figures 7.1(a)-(c) display the sheet resistivity, sheet carrier density and carrier mobility respectively for uncapped sample δ-1, recorded at temperatures within the range of 300-500K. The sheet resistivity trend (figure 7.1(a)) following annealing at 673K displays little change over the measured temperature range (metallic conductivity). Annealing at 873K results in increased sample resistivity to approximately 10^5 Ohm/sq, furthermore the resistivity of uncapped sample δ-1 over the measured temperature range now displays greater temperature dependence. After 873K anneal a thermally activated process with an E_a of 47meV becomes apparent. The sheet carrier density (figure 7.1(b)) is recorded between 2-3 x $10^{14} cm^{-2}$ over the measured temperature range for uncapped sample δ-1 after 673K anneal. The sheet carrier density, following 873K annealing decreases to 2-3x$10^{13} cm^{-2}$ (300K); at higher temperatures the sheet carrier density further reduces to 1-2x$10^{13} cm^{-2}$. Carrier mobility for uncapped sample δ-1 (figure 7.1(c)) varies between 1 and 4cm^2/Vs over the measured temperature range. Taking scatter in the data points into consideration no clear trend is present.

Figures 7.2(a)-(c) display sheet resistivity, sheet carrier density and carrier mobility respectively for uncapped sample δ-2, recorded at temperatures within the range of 300-500K. The sheet resistivity trends (figure 7.2(a)) before and after 873K annealing exhibit little change over the measured temperature range. The 673K trend displays a sheet resistivity of 2.5x10^4 Ohm/sq at 300K decreasing to 2.2x10^4 Ohm/sq at 500K. Annealing at 873K results in a marginally higher sheet resistivity (3.2x10^4 Ohm/sq at 300K), the trend thereafter is identical to that observed for the 673K trend. Two thermally activated processes are observed from both the 673 and 873K data trends with E_a's of 6meV, 9meV and 6meV, 16meV determined respectively. The sheet

carrier density of uncapped sample δ-2 is shown in figure 7.2(b). The 673K anneal trend displays a sheet carrier density of 2×10^{14} cm^{-2} over the measured temperature range. The 873K anneal trend displays similar values at lower temperatures; at higher temperatures from 400-500K a reduction in the sheet carrier density occurs from 2×10^{14} to 1×10^{14} cm^{-2}. Carrier mobility for uncapped sample δ-2 (figure 7.2(c)) varies between 0.8 and 2cm^2/Vs.

7.3.2 Capped samples δ-3 and δ-4

Figures 7.3(a)-(c) display the sheet resistivity, sheet carrier density and carrier mobility respectively for capped sample δ-3, recorded at temperatures within the range of 300-500K. The sheet resistivity trend (figure 7.3(a)) before and after 873K annealing exhibits a resistance of 8×10^3 Ohm/sq. Semi-metallic (3meV) and metallic resistance trends are recorded here. A sheet carrier density of 1-2 x 10^{14}cm^{-2} (figure 7.3(b)) is recorded over the measured temperature range after both a 673K and 873K anneal. Carrier mobility for capped sample δ-3 (figure 7.3(c)) before and after 873K annealing remains virtually unchanged, the mobility here varies between 3 and 4cm^2/Vs.

Figures 7.4(a)-(c) display the sheet resistivity, sheet carrier density and carrier mobility respectively for capped sample δ-4, recorded at temperatures within the range of 300-500K. The sheet resistivity trend (figure 7.4(a)) before and after 873K annealing displays a resistivity of 6-7x10^3 and 7-8x10^3 Ohm/sq respectively, these trends display metallic behaviour. A sheet carrier density of 2×10^{14}cm^{-2} (figure 7.4(b)) is recorded over the measured temperature range following each annealing treatment. Carrier mobility for capped sample δ-4 (figure 7.4(c)) in both cases remains between 2 and 3cm^2/Vs.
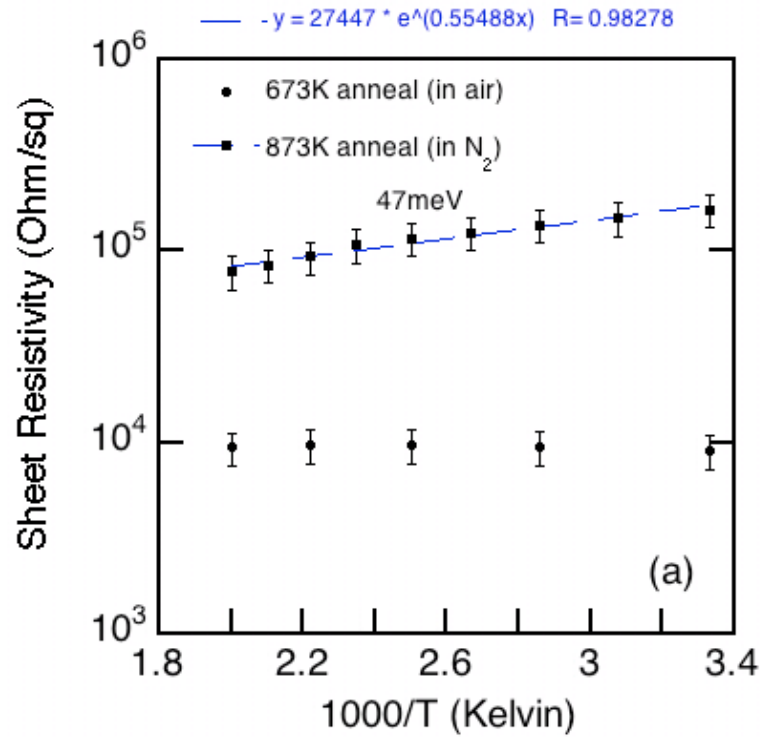
Figure 7.1(a): Sheet resistivity plotted against 1000/T for uncapped sample δ-1.
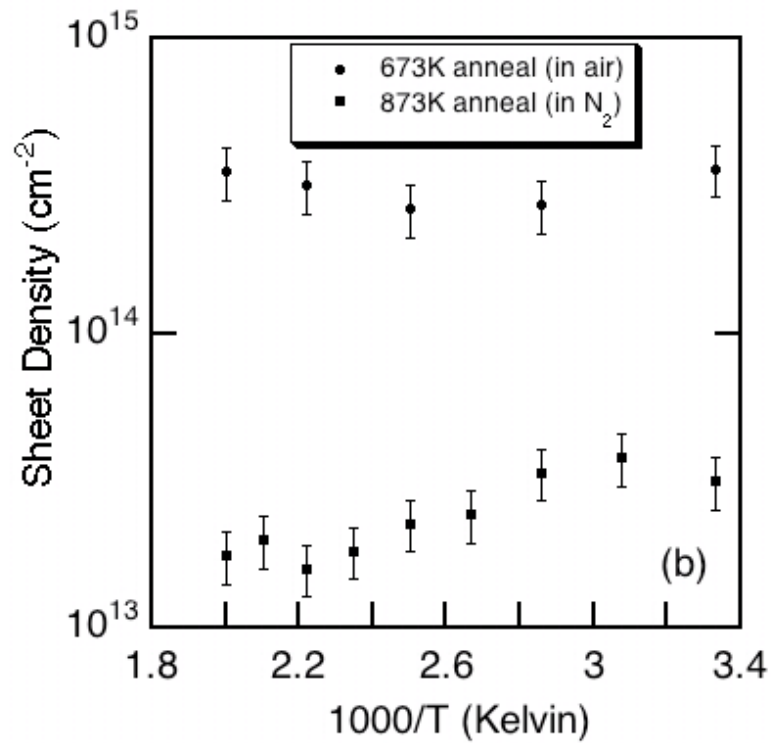

Figure 7.1(b): Sheet density plotted against 1000/T for uncapped sample δ-1.

157

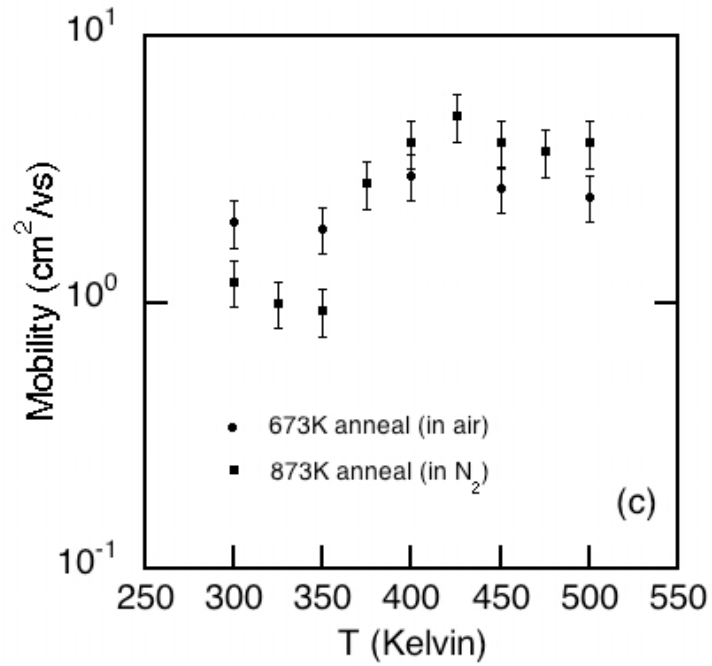Figure 7.1(c): Carrier mobility (hole) plotted against temperature for uncapped sample δ-1.
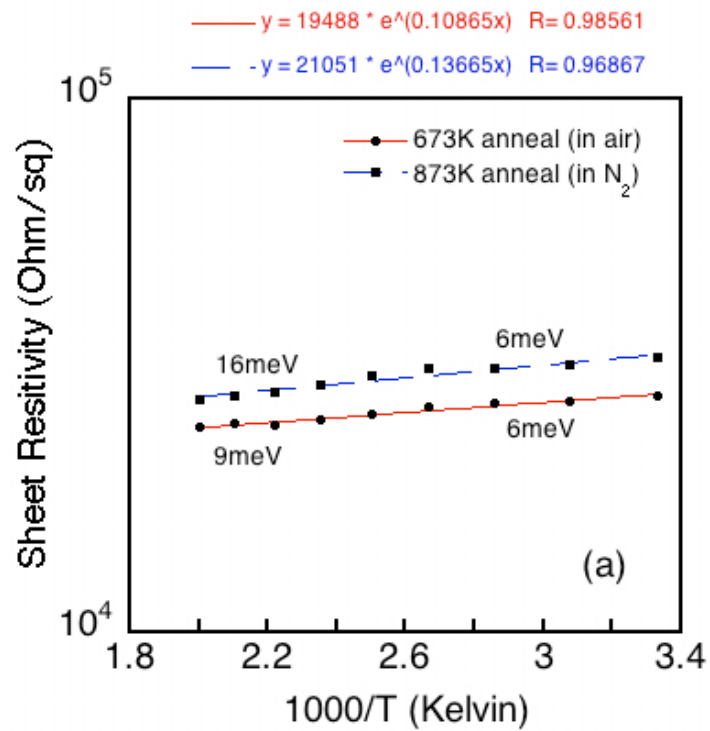

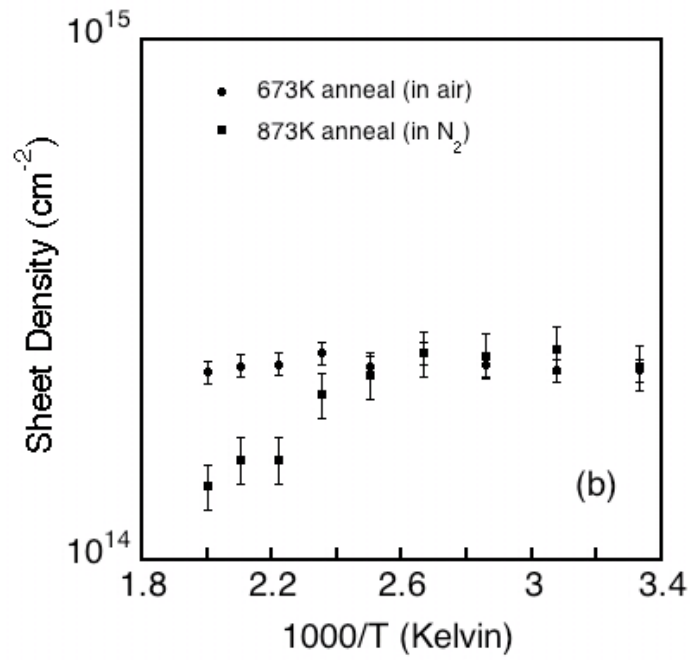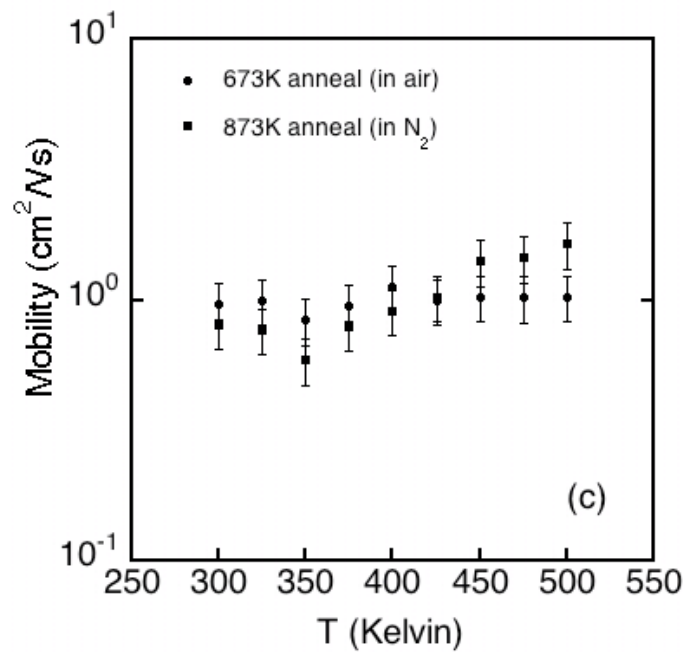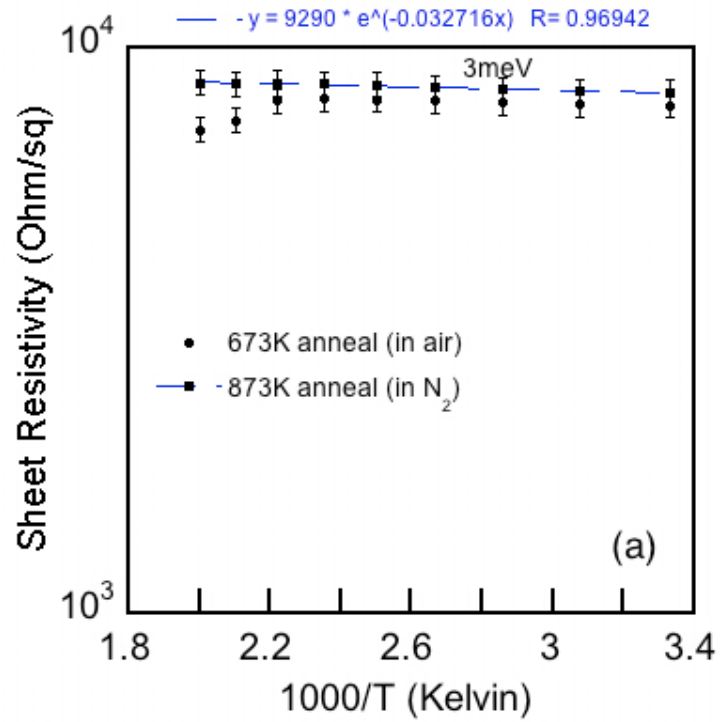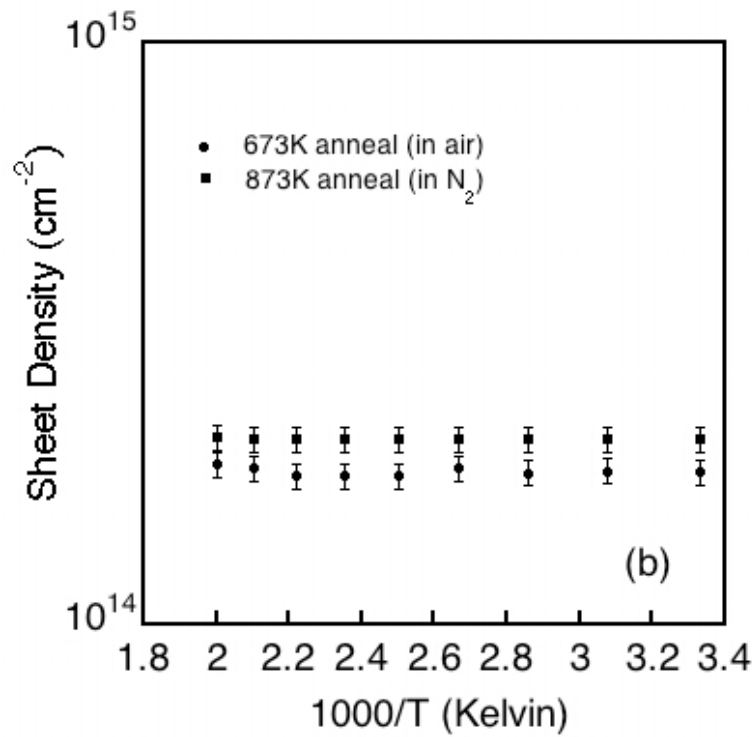Figure 7.2(a): Sheet resistivity plotted against 1000/T for uncapped sample δ-2.

Figure 7.2(b): Sheet density plotted against 1000/T for uncapped sample δ-2.

Figure 7.2(c): Carrier mobility (hole) plotted against temperature for uncapped sample δ-2.

Figure 7.3(a): Sheet resistivity plotted against 1000/T for capped sample δ-3.

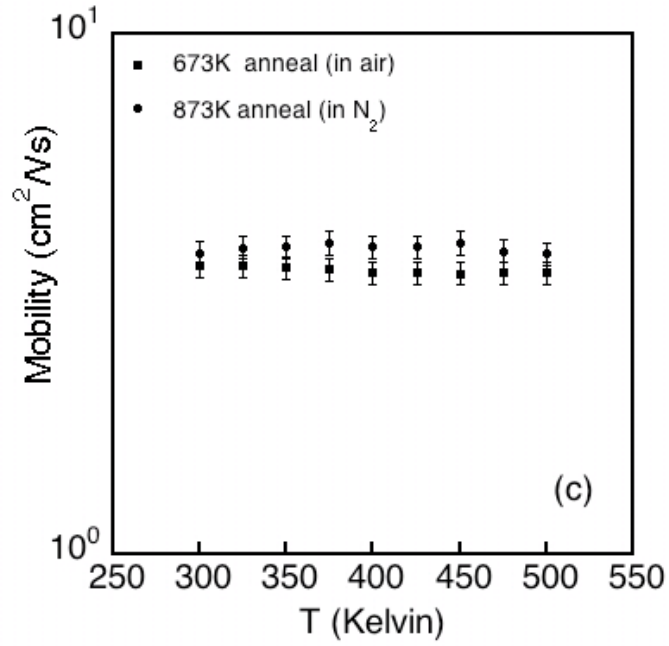Figure 7.3(b): Sheet density plotted against 1000/T for uncapped sample δ-3.

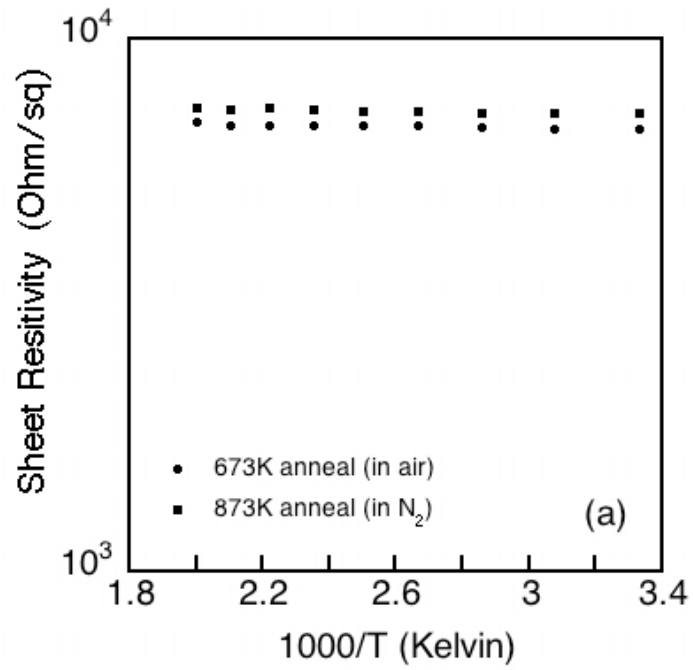Figure 7.3(c): Carrier mobility (hole) plotted against temperature for capped sample δ-3.

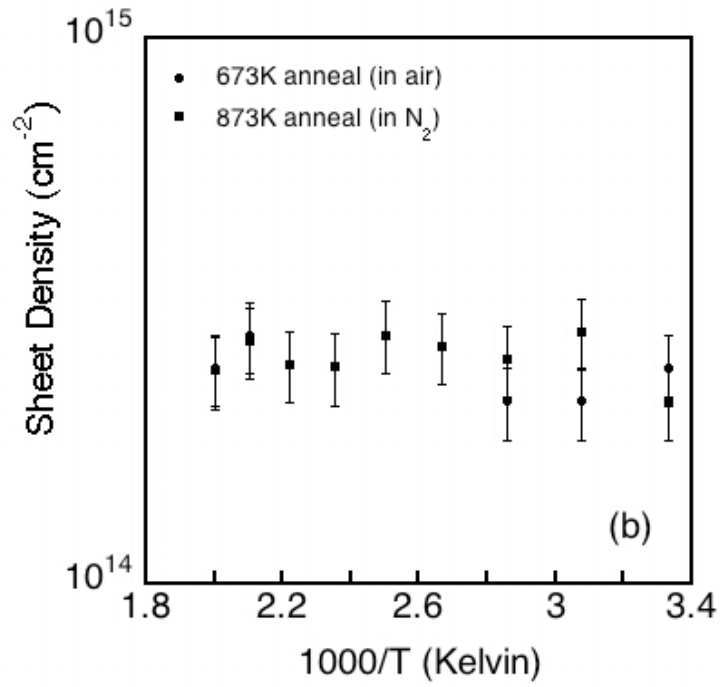Figure 7.4(a): Sheet resistivity plotted against 1000/T for capped sample δ-4.

Figure 7.4(b): Sheet density plotted against 1000/T for capped sample δ-4.
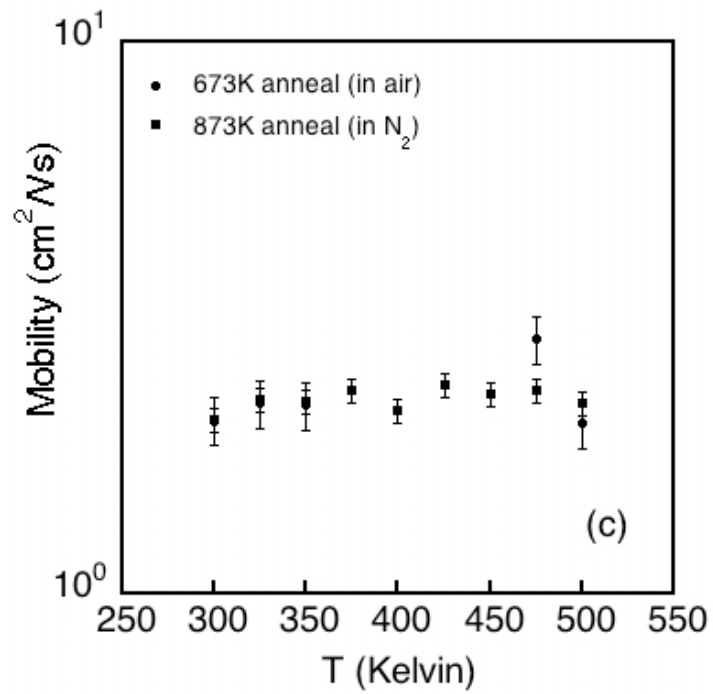

Figure 7.4(c): Carrier mobility (hole) plotted against temperature for capped sample δ-4.

7.4 Discussion

Chemical analysis (secondary ion mass spectroscopy, (SIMS)) performed by e6 laboratories, revealed a boron concentration between 4 and 7 x 10^{20} cm^{-3} in these δ-doped diamond layers, in agreement with Hall effect analysis (table 7.1).

Sample No	Carrier density (cm^{-2}) (300K)	δ-layer thickness (FWHM)	Carrier Concentration (cm^{-3})	SIMS (cm^{-3})
δ-1	2.5 x 10^{14}	5nm	5 x 10^{20}	5 x 10^{20}
δ-2	2.5 x 10^{14}	3.2nm	6 x 10^{20}	-
δ-3	1.8 x 10^{14}	5nm	4 x 10^{20}	4 x 10^{20}
δ-4	2.3 x 10^{14}	3.2nm	7 x 10^{20}	7 x 10^{20}

Table 7.1: Carrier concentrations (Hall effect) and chemically attained boron concentrations of δ-doped diamond layers (by SIMS).

Sheet resistivity and sheet carrier density values can be seen to display little change over the measured temperature range and after each heat treatment for all samples in this study, except uncapped sample δ-1. Thermal activation energies in the meV range alongside metallic conductivity are observed throughout, in good agreement to that expected for highly boron doped diamond films [1]. For sample δ-1 following a second anneal at 873K in nitrogen a reduction in sheet carrier density by 1 order of magnitude from $3x10^{14}$ to $2x10^{13}$ cm^{-2} (figure 7.1(b)) is seen, commensurate with an increase in the sheet resistivity from 10^4 to 10^5 Ohm/sq (figure 7.2(a)) for this sample. Since the CVD growth process is hydrogen-rich it is possible to speculate that a hydrogen-related defect or perhaps a hydrogen-complex could be responsible for this effect [4]. The sheet carrier density is reduced by one

order of magnitude, so it is not simply the removal of hydrogen passivation of boron, since this would be expected to lead to an increase in free carrier density. A more likely explanation may be that passivation of hydrogen-related deep traps may be being removed, such that these traps may now charge and lead to a reduction in the number of free carriers in the diamond [5,6]. That the 873K anneal step makes *no change* to the data recorded for the remaining samples suggests that the concentration profile in these samples is much more abrupt and thermally stable. Furthermore, annealing at high temperatures does not seem to have any obvious beneficial effect on the electrical characteristics of these structures.

Carrier mobilities reported for high quality δ-doped layers within III-V semiconducting technologies range from 10^3-10^4 cm^2/Vs [7]. El-Hajj and co-workers [8] reported (in 2008) Hall mobilities of boron δ-doped diamond layers at 20-30cm^2/Vs. In this study mobility values are recorded between 1 and 5 cm^2/Vs. The fact that carrier mobilities seen here are comparable to those routinely observed in heavily boron-doped diamond films [1] implies that a limited δ-doping effect is present in these structures, and more so that carrier transport is still mainly confined to the δ-layer itself. An impedance spectroscopic study presented in this thesis (chapter 6) and published in the *Journal of Applied Physics* [9] sheds further light on the origin of the low carrier mobilities recorded.

7.5 Conclusions

Highly boron δ-doped diamond layers have been produced using microwave-plasma CVD techniques as characterised by SIMS and Hall effect. All films display either thermal activation energies in the meV range for the release of carriers (holes) at very high carrier density levels or metallic resistance trends, as expected for these heavily boron-doped diamond films. Carrier transport observed in this study is mainly hopping in character. Improvements to the

growth conditions are necessary to ensure the development of this technology.

7.6 References

1. T.H. Borst and O. Weiss, Physica Status Solidi, A154, 423 (1996).

2. B. Baral, S.S.M. Chan and R.B. Jackman, J. Vac. Sci. Technol. A 14, 2303 (1996).

3. O.A. Williams and R.B. Jackman, J. Appl. Phys., 96, 3742 (2004).

4. M.I. Landstrass and K.V. Ravi, Appl. Phys. Letts., 55, 975 (1989).

5. M.I. Landstrass and K.V. Ravi, Appl. Phys. Letts., 55, 1391 (1989).

6. J. Chevallier, B. Theys, A. Lusson, C. Grattepain, Physical Review B, 58, 7966 (1998).

7. "Delta-doping of Semiconductors" E.F. Schubert (Ed.), (Cambridge University Press, 1996).

8. H. El-Hajj, A. Denisenko, A. Bergmaier, G. Dollinger, M. Kubovic and E Kohn. Diam. & Relat. Mater., 17, 409 (2008).

9. N. Tumilty, J. Welch, R. Lang, C. Wort, R. Balmer, and R. B. Jackman, J. Appl. Phys. 106, 103707 (2009).

Chapter 8: Synthesis of carbon nanotubes on single crystal diamond

8.1 Introduction

8.2 Experimental methods

8.3 Results

8.4 Discussion

8.5 Conclusions

8.6 References

8.1 Introduction

Nanostructured carbons lie at the heart of the development of a whole host of materials for future nanotechnological applications. Unexpected properties often arise when such materials are a composite of differing carbon forms. Diamond and carbon nanotubes (CNTs), despite having strongly differing C-C bonding structures, are the strongest and toughest of the various forms of carbon, and it is of interest to develop an insight into the properties of materials that involve these allotropes. In this study we demonstrate the novel growth of multi-wall carbon nanotubes (MWCNTs) on diamond substrates, creating an all carbon composite system. Carbon structures we now know as MWCNTs were reported some years ago by Radushkevich and Lukyanovic [1], although technology limitations at this time meant their structure properties were not clearly understood. CNTs did not receive widespread scientific attention until the early 1990s [2]. Since then CNTs have been studied in many laboratories on a wide variety of conducting, semiconducting and insulating materials revealing astonishing electrical and mechanical properties [3]. Diamond has been admired as a gemstone for centuries for its natural beauty, but it is the remarkable electrical and mechanical properties of this material (diamond) [4] that are of interest to researchers worldwide. Diamond deposition using chemical vapour deposition (CVD) has enabled single crystal diamond of high purity to be

commercially available [5]. Diamond can be considered as a wide band gap semiconductor (5.5eV), with boron readily incorporated into diamond CVD layers making them p-type with an ionization energy of 0.37eV at moderate concentrations [6]. In comparison, the carbon nanotube is a relatively new form of crystalline carbon. An extremely important characteristic of the CNT is its helicity that describes how the graphene sheet is rolled up around its axis. This helicity is defined by the chirality vector; C_h = n a1 + m a2, where a1 and a2 are primitive vectors, n and m being integers [7]. Depending on this 'wrapping vector' the single wall carbon nanotube (SWCNT) can have different atomic structures namely zigzag, armchair and chiral (these names are real-life descriptions of the differing atomic structures CNTs can have) all of which can give varying degrees of electrical conductivity (If (n-m) is divisible by 3, the tube is metallic, if not divisible by 3, the tube is semiconducting).
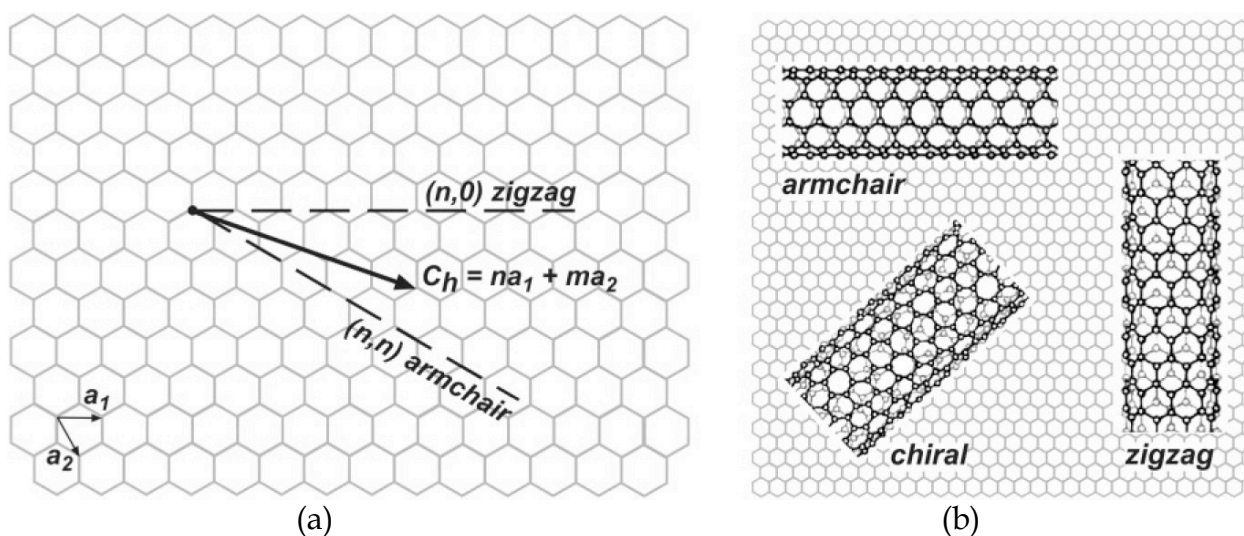

(a) (b)

Figure 8.1(a)&(b): Models of nanotubes with different CNT helicities showing the rolling of a graphene sheet along different chiral vectors (from [7]).

The mechanism involved in producing these different SWCNT geometries, presently not controllable during synthesis, has been linked to the catalytic transition metal used to initiate growth and its interaction with the surface [8]. Growth of CNTs has been developed using a variety of CVD techniques

(microwave, RF, thermal and DC) alongside metal catalysts to promote growth [2,9,10] at temperatures from 500°C to 1200°C. Typically, catalysts include Ni, Co and Fe transition metals. A large number of papers can be found in the literature reporting CNT growth for these transition metals, which have been recently reviewed [11].

During the initial heating stages of CVD the catalyst film coarsens and forms small sphere-like nanoparticles that dictate the diameter of the CNT. A carbon-containing precursor (CO, CH_4, C_2H_2) is then required, and under suitable conditions decomposition of the carbon containing gas occurs as it interacts with the catalyst nanoparticles. At this juncture two different scenarios are possible. If the particle adherence to the surface is strong, then carbon precipitates from the top surface of the particle and the CNT continues to grow with the particle anchored to the substrate. This is called the base growth model. In cases where the particle attachment to the surface is weak, then carbon precipitation occurs at the bottom surface of the particle and the filament lifts the particle as it grows. In this case, the top end of the filament is decorated with the catalyst particle, and this scenario is aptly called the tip growth model. Baker and co-workers [12,13] and also [14] arrived at the above mechanisms for carbon filament growth based on temperature dependent growth rates, activation energy for various steps, and electron microscopy observations.

(c)   (d)
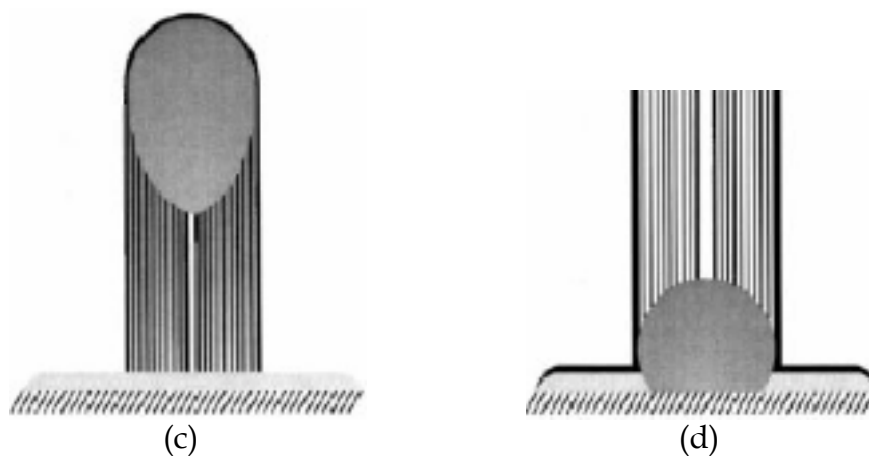
Figures 8.1(c) & (d): Tip and base growth modes respectively.

Recent work by Takagi *et al* [15] from NTT Basic Research Laboratories, Japan; have cleverly demonstrated that nanodiamond particles act as efficient nuclei for CNT formation. Fernandes and co-workers [16] have shown that a composite CNT-diamond material may be made using microwave plasma-assisted CVD. Nanodiamond conglomerates were found to be connected by MWCNTs, resembling a flat 2D neural-network. In this study the formation of a coherent composite with an interface between highly aligned CNTs and single crystal diamond substrates is attempted for the first time.

If this all-carbon system is to be explored for future applications, it is vital that the interface in this novel diamond-CNT heterostructure is chemically stable and fully bonded. Theoretical studies by Shenderova *et al* [17] suggest that particular combinations of nanotubes and diamond surfaces should indeed form chemically and mechanically stable interfaces. These atomistic simulations also suggested that significant lattice mismatch between a diamond surface and a nanotube can be accommodated by nanotubes due to their high radial flexibility. In this paper, a systematic study of CNTs grown on diamond 1b (100) single crystal substrates using a glow-discharge method is presented, demonstrating CNT growth characteristics as a function of both temperature and growth gas mixtures. It is shown that a highly stable interface between CNTs and diamond can be produced.

8.2 Experimental methods

In this study Ni films (~25nm thick) were deposited on diamond 1b (100) HPHT substrates (Element Six Ltd, UK) using a calibrated thermal vacuum evaporator (base pressure ~ 10^{-7}mbar). The film thickness is monitored in situ by a quartz crystal microbalance, and calibrated ex situ by a Dektak8 surface profiler. All diamond substrates were cleaned in highly oxidising solutions prior to use, which is known to leave the surfaces free from contaminants and

oxygen terminated [18]. A dc glow-discharge chamber with a heated resistive plate was utilised throughout (base pressure of $5x10^{-6}$mbar) with mass flow controlled (MFC) gas feeds. The distance between the electrodes was ~15mm. Growth temperature was monitored by a thermocouple directly connected to the underside of the heated stage, beneath the sample position. A mixture of methane, hydrogen and nitrogen were used during CNT synthesis. The pressure during growth was maintained at 5 mbar, discharge current and voltages were 75mA and 390V respectively. Typically, the samples were first annealed within the evacuated chamber for 10mins and then for 7 minutes in a H_2 ambient (0.5mbar, flow rate 30sccm). A DC discharge was then ignited between the heated stage (cathode) and the Molybdenum disc above (anode) by applying a fixed discharge current for 20 minutes. Once growth was terminated the chamber was allowed to cool down to below 200°C before the chamber was vented to prevent any damage occurring to the CNTs. AFM measurements were carried out in tapping mode on a Nanoscope V (7.0) controlled Dimension V Scanning Probe Microscope equipped with an XYZ hybrid scanner (Veeco Instruments Inc, Germany) to analyse the surface profile of an annealed Ni film prior to growth under atmospheric conditions. To investigate the dependence of the CH_4/H_2 ratio on CNT growth scanning electron microscopy was used (JEOL JSM-7401F, JEOL Ltd., Japan). A Renishaw Raman spectroscopic microscope (incident laser, 514nm) was also utilised in this study to extract crystallographic information from the as-grown CNTs on diamond substrate. Energy-dispersive X-ray spectroscopy (15keV electron beam) is used to verify the elemental composition of these CNT structures.
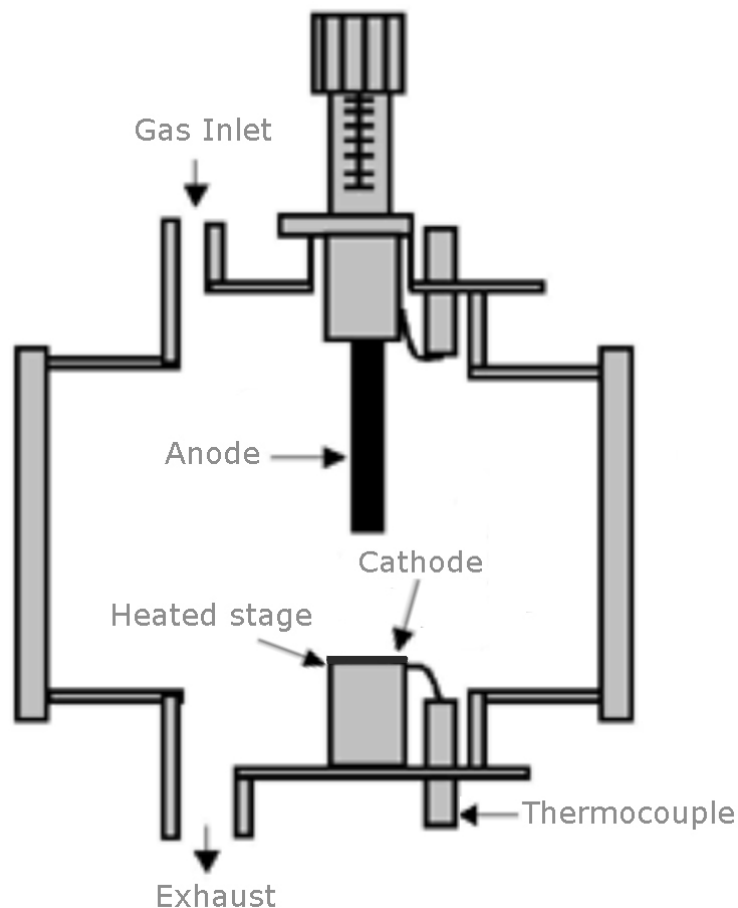
Figure 8.2: Schematic of glow-discharge kit used for CNT growth.

8.3 Results

To characterise the surface morphology of the annealed Ni films on diamond substrate, AFM analysis was performed (see figure 8.3). Fig 8.3 demonstrates that the Ni film has broken up into island formation as a result of surface tension. Individual Ni nanoparticles are visible on the diamond surface; large and small features are present. The largest particles have a diameter of ~80nm whereas the smaller particles have a diameter within the range 20-30nm.
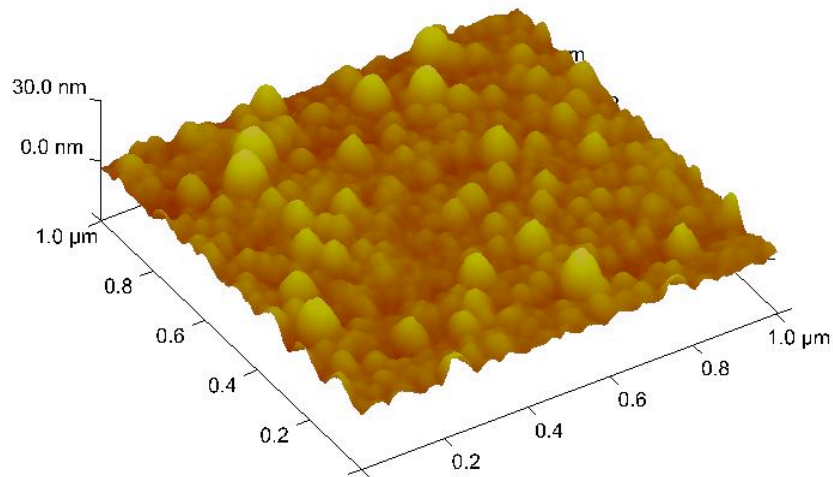
Figure 8.3: Typical AFM surface profile measurement (in tapping mode) of a Ni film after annealing at 700°C (3x10^{-5}mbar) and then in a H$_2$ ambient at 0.5mbar for 7 minutes.

Sample No	CH$_4$ (%)	H$_2$ (%)	N$_2$ (%)	Ni layer (nm)	T$_{growth}$ (^{o}C)
1	15.3	81.7	3	25	700
2	22.2	74.8	3	25	700
3	25.2	71.8	3	25	650
4	25.2	71.8	3	30	700
5	25.2	71.8	3	25	750
6	34.6	62.4	3	25	700
7	42.3	54.7	3	25	700
8	53.8	43.2	3	25	700

Table 8.1: Growth conditions for CNT synthesis on diamond.

Table 8.1 records the main experimental parameters that were explored. The methane concentration in the feedstock gas was varied from 15% to 53% of the total gas volume, with a fixed nitrogen volume of 3% and various hydrogen volumes. CNT growth was performed at temperatures of 650°C, 700°C and 750°C.

8.3.1 Influence of temperature on growth

SEM imaging, shown in figures 8.4(a)-(c) documents the change in CNT growth on diamond substrates at temperatures of 650°C, 700°C and 750°C (sample #3, #4 and #5 respectively). It can be observed that substantial CNT growth occurs at 700°C, with CNT widths of 20-30nm, commensurate with the size of the (smaller) Ni particles (EDX spectrum, figure 8.6(e)). Excellent film uniformity is apparent with Ni nanoparticles observed at the tip of nearly every carbon nanotube (figure 8.5). A substantial reduction in CNT growth density and height is observed at 650°C, and interestingly no growth is observed at 750°C.
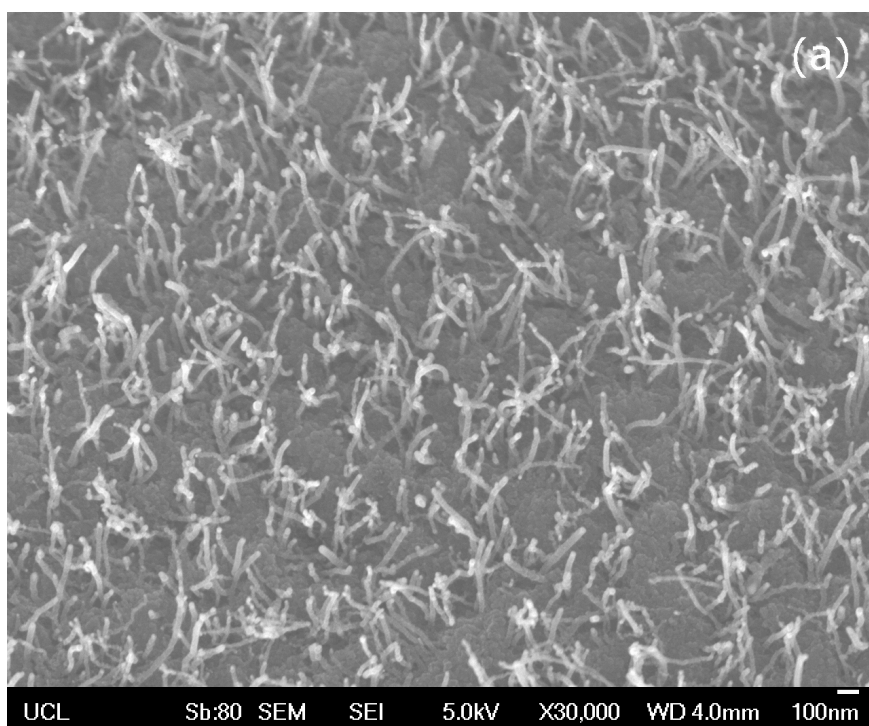

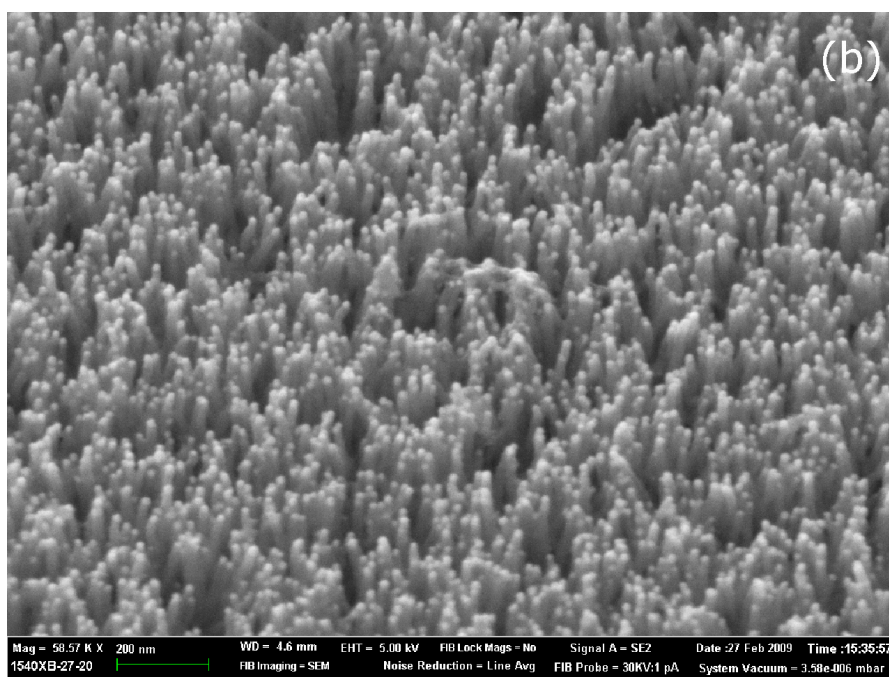Figure 8.4(a): SEM image displaying CNT growth at 650°C (sample #3).

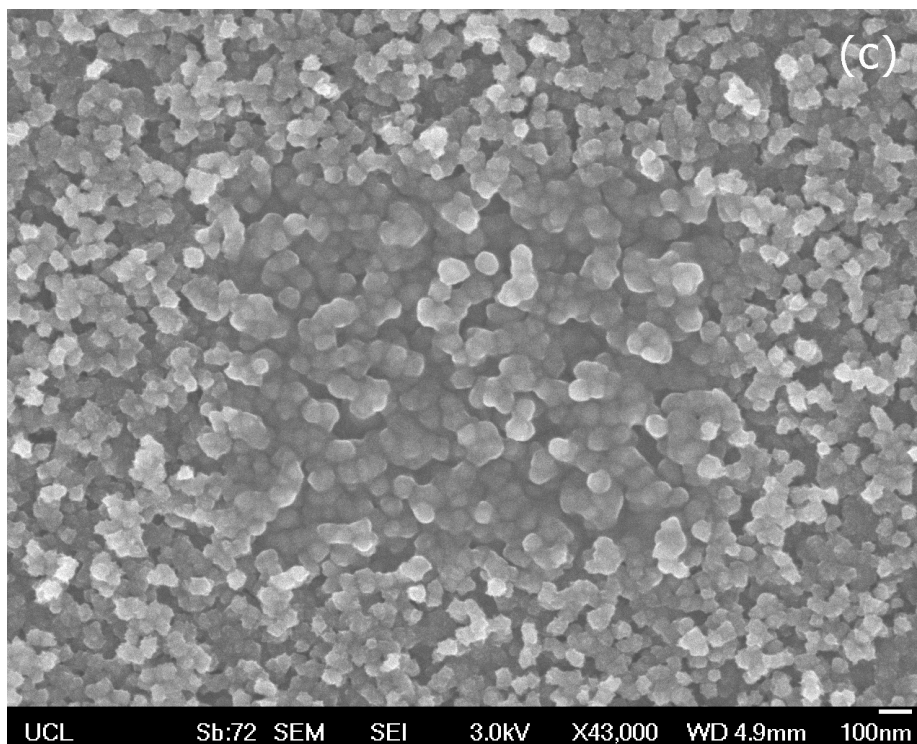Figure 8.4(b): SEM image displaying CNT growth at 700ºC (sample #4).

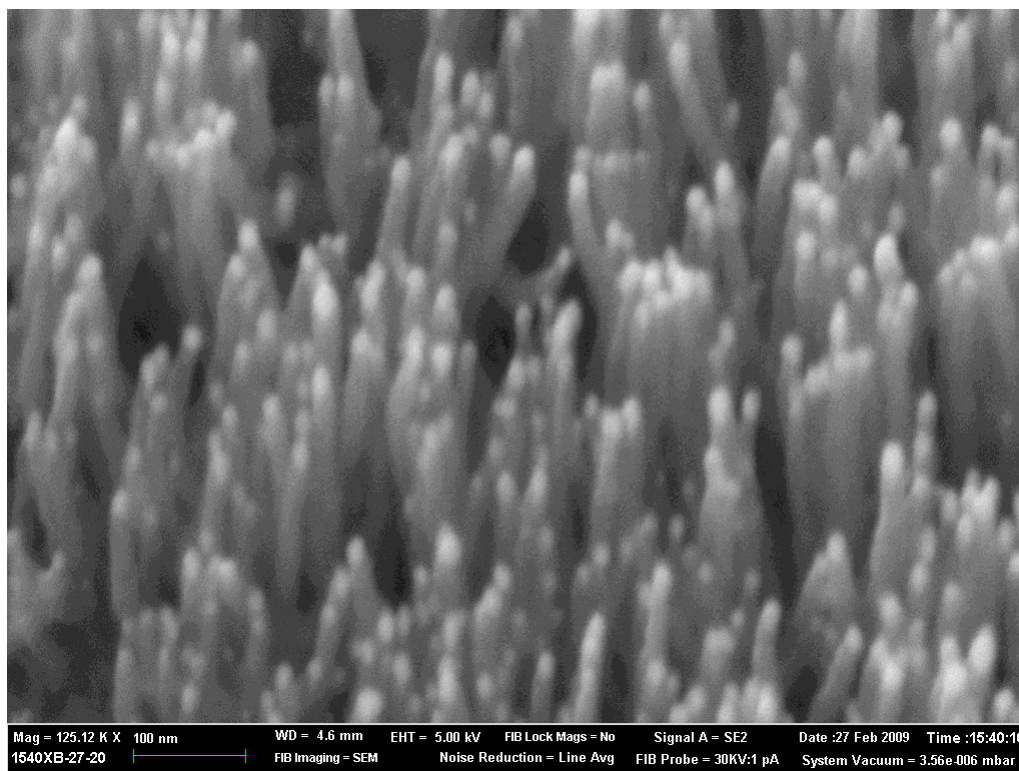Figure 8.4(c): SEM image displaying no CNT growth at 750ºC (sample #5).

Figure 8.5: SEM image displaying the tip growth mode occurring here for these CNTs grown on diamond substrate.

8.3.2 Influence of CH_4/H_2 concentration on growth

Synthesised CNTs were also analysed on diamond substrates at various methane/hydrogen concentrations (table 8.1). Figures 8.6(a)-(d) display SEM images starting with a 15% methane concentration used during CNT synthesis, increasing to 22%, 25% and 35% respectively. For a 15% CH_4 concentration, respectable non-uniform growth is observed, with the CNTs grown under these conditions exhibiting weak vertical alignment. These CNTs have an average height of ~200nm with Ni nanoparticles clearly visible at their tip.

At 22% CH_4, substantial growth of vertically aligned CNTs is observed with these structures having an average height of ~200nm with Ni nanoparticles also visible at their tips; similar characteristics are seen for sample #4 which was grown using a 25% CH_4 concentration (figure 8.6(c)). The diameter and

length of the CNTs seen here exhibit good uniformity. These CNTs also have a diameter between 20nm to 30nm, in good agreement to that expected given the initial deposited Ni layer thickness. Figure 8.6(d) (sample #6) displays the growth observed for a 35% CH_4 concentration. Here a considerable reduction in CNT yield and uniformity is observed. CNT synthesis was also performed using a CH_4 concentration of 42% and 54% (samples #7 and #8 respectively). SEM analysis for sample #7 reveals further reductions in CNT yield and for sample #8 no growth is observed (images for samples #7 and #8 are not shown for brevity). Raman spectra taken from CNTs grown with 15%, 22% and 25% CH_4 concentration are shown in figures 8.7(a) & (b). Figure 8.7(a) displays the Raman spectra of sample #1 grown with 15% CH_4 concentration; here three peaks are easily observed at ~1120cm^{-1}, 1332cm^{-1}, and 1610cm^{-1} (G-band). In addition, for sample #1 a fourth peak at ~1345-1350cm^{-1} is observed on the side of the diamond peak (1332cm^{-1}). Curve fitting (Lorentzian) using a specialist software package (MatLab) failed to pick up this peak due a lack of available data and the significant difference in the intensity of diamond peak relative to the peak occurring ay occurring ~1350cm^{-1}. The position of this peak when extrapolated to the x-axis is in excellent agreement with values observed in the literature for amorphous carbon material [20]. Further evidence of this peak can be seen in the remaining samples analyzed by Raman spectroscopy. Figure 8.7(b) displays the Raman spectra for sample #2 grown with a CH_4 concentration of 22%, here three absorption peaks are visible; 1332cm^{-1}, 1350cm^{-1} (D band) and 1580cm^{-1} (G band). For sample #4 (figure 8.7(b)) no peak is seen at 1332cm^{-1}, the D band peak is now at 1355cm^{-1} with the G band peak remaining at 1580cm^{-1}. The 1332cm^{-1} peaks seen in figures 8.7(a) & (b) originate from the diamond substrate. This diamond peak is not seen for sample #4 because of the very high yield of CNTs observed on the surface of this sample (figures 8.4(b) and 8.6(c)).
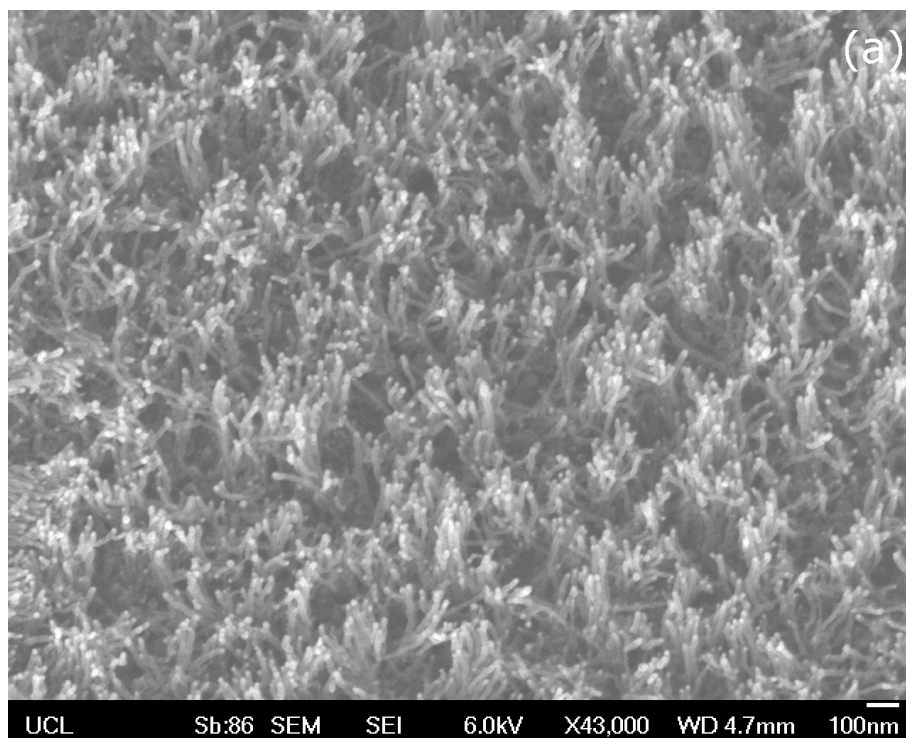
Figure 8.6(a): SEM image displaying CNT growth with a 15% CH$_4$ concentration (sample #1).
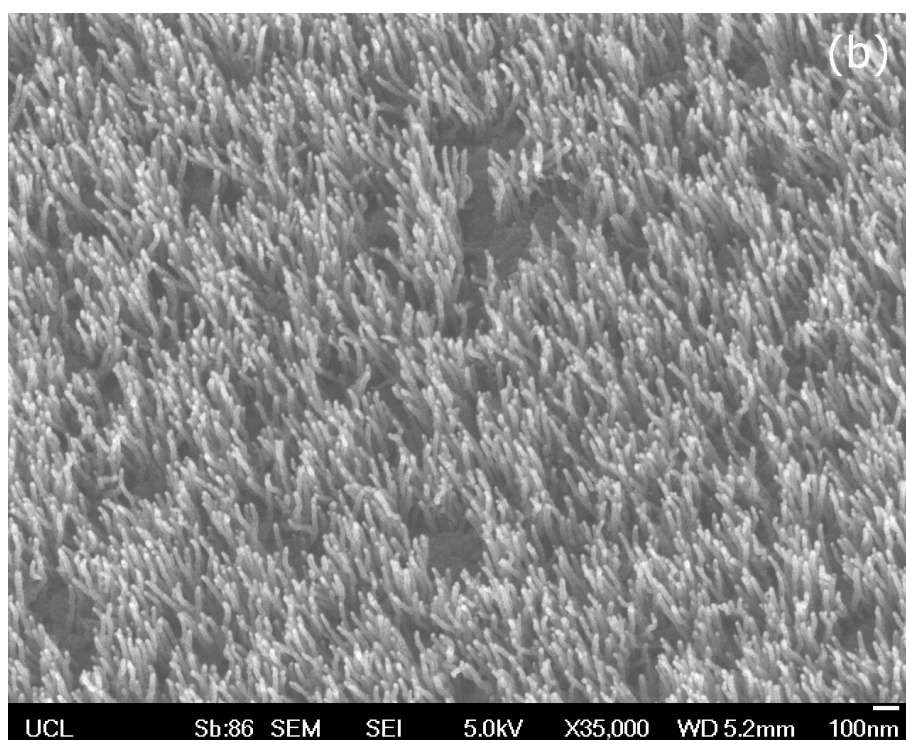

Figure 8.6(b): SEM image displaying CNT growth with a 22% CH$_4$ concentration (sample #2).
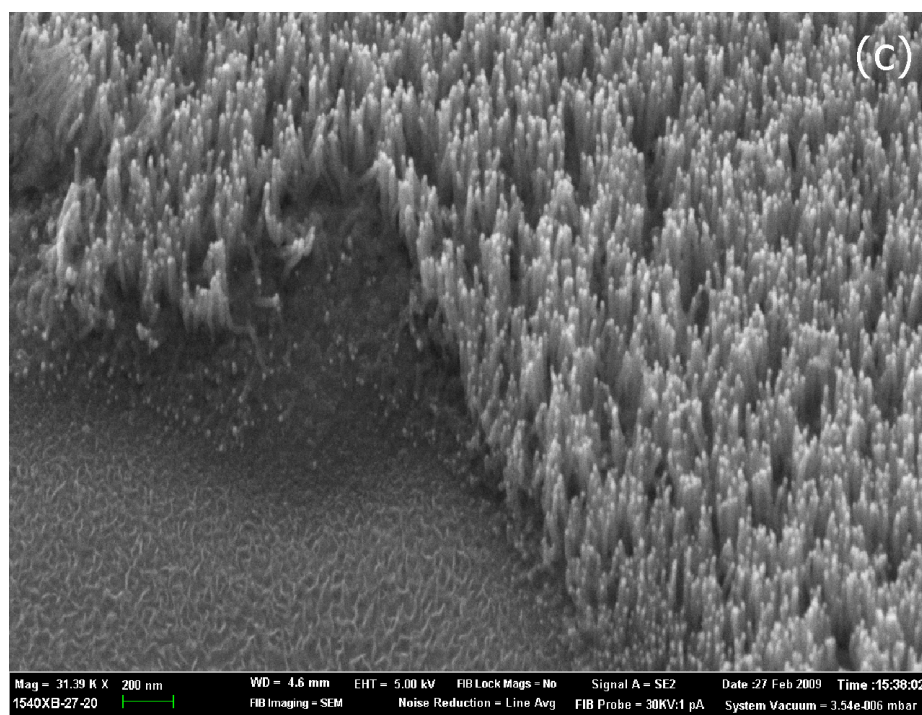
Figure 8.6(c): SEM image displaying CNT growth with a 25% CH$_4$ concentration (sample #4).
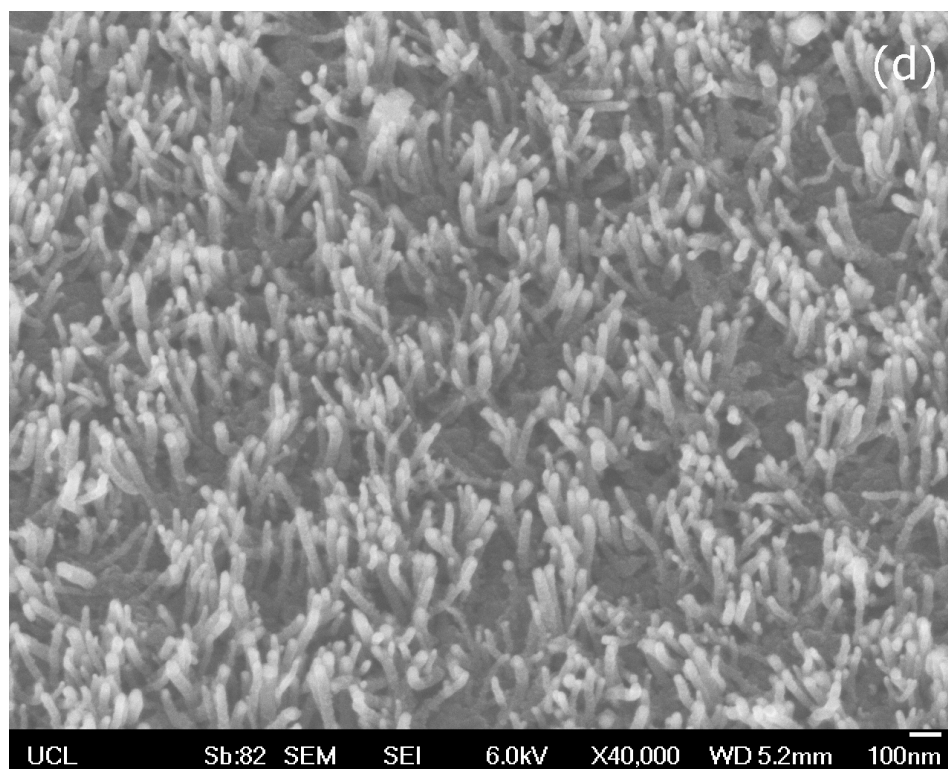

Figure 8.6(d): SEM image displaying CNT growth with a 35% CH$_4$ concentration (sample #6).

The as-grown CNTs were found to strongly adhere to the diamond substrate; sonicating and sticky-tape tests failed to remove the carbon structures that could be observed to have remained adhered to the diamond in subsequent SEM analysis. Furthermore, high temperature annealing at ~700°C at 3x10⁻⁵mbar had little effect on the surface density and crystallographic nature of these CNTs.
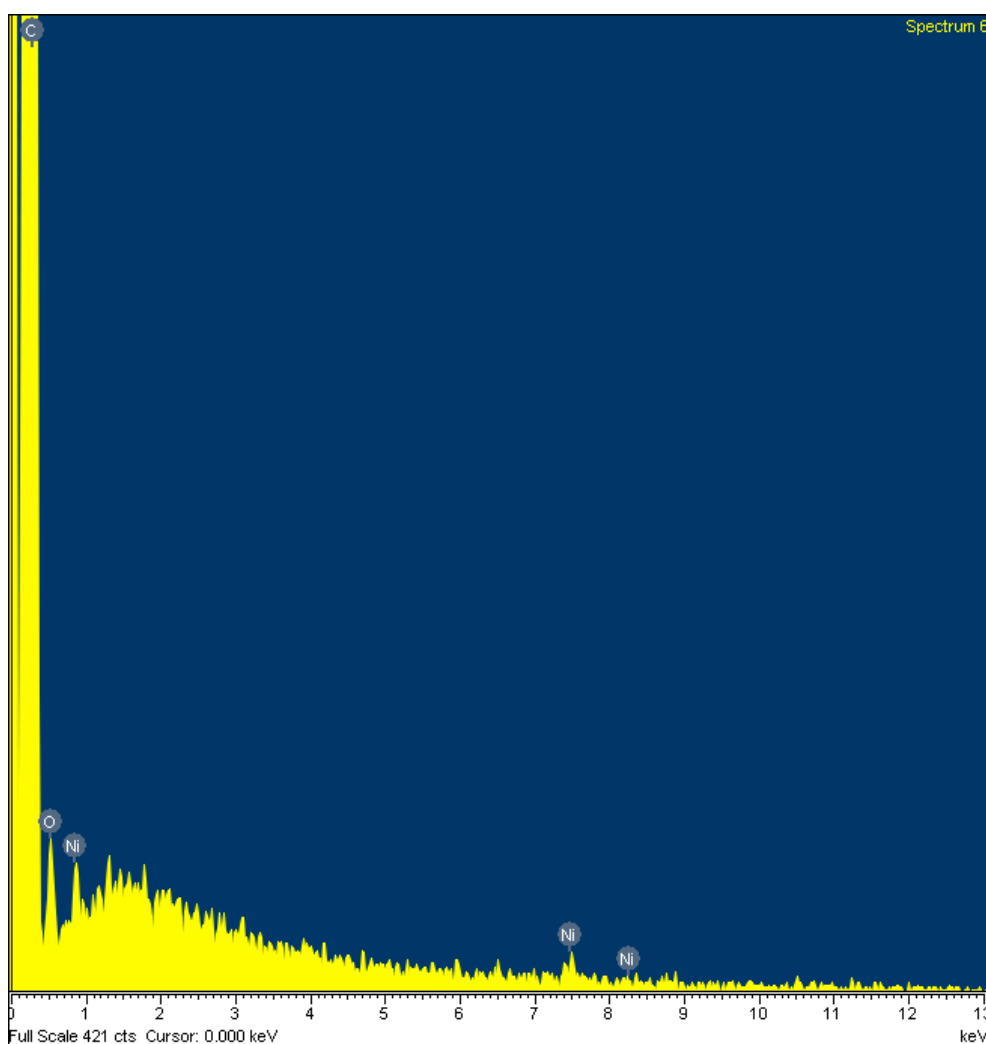

Figure 8.6(e): Energy-dispersive X-ray spectroscopy (EDX) spectrum of a CNT-diamond sample.

Figure 8.6(e) displays the elemental make-up of an annealed CNT sample (in air). A strong carbon peak of 0.28KeV (K_α series) is evident as are weaker Ni peaks at 0.85KeV (L_α series), 7.48KeV (K_α series) and 8.26KeV (K_β series). The

observed Ni peaks indicate that Ni nanoparticles are present at the tips of these CNTs. The intensities of the peaks observed, especially the C and Ni peak are in good agreement with the expected quantities of C and Ni in these samples. The oxygen peak (contamination) is thought to arise as a direct result of annealing this sample in air (400°C for 20minutes).

8.4 Discussion

The influence of the CH_4/H_2 ratio in the growth mixture on CNT growth is in good agreement with published observations [9], with CNT growth in this study peaking between 22-25%. It is well established that at lower CH_4 concentrations (15% in this study) a lower CNT yield is observed as not enough carbon is available for growth and at higher methane concentrations (35% in this study) reduced CNT growth is seen due to the covering of the Ni particles with an amorphous carbon overcoat, i.e. catalyst poisoning [9]. This is expected, given the abundance of active radicals in the plasma system. At 650°C a substantial reduction in growth is observed (figure 8.4(a)). This observation is in good agreement with CNT synthesis experiments, as methane, the most stable of all the hydrocarbons, does not fully dissociate on transition metals at lower temperatures [9]. At 700°C substantial uniform CNT growth is seen (figure 8.4(b)), whilst at 750°C there appears to be conglomerates of amorphous carbon formed on the surface (figure 8.4(c)). This is most likely due to the rearrangement of the catalyst particles into larger aggregates therefore preventing CNT growth.

From SEM analysis (figures 8.5 and 8.6(a)-(d)) it can be seen that Ni nanoparticles are present at the tip of these thick carbon nanotubes, indicating that the tip growth model is occurring here. This form of growth is nominally seen when there is week interaction between the catalyst nanoparticle and the surface, allowing the Ni nanoparticle to be lifted from the surface as carbon precipitates from it. That this is the case with diamond substrates is

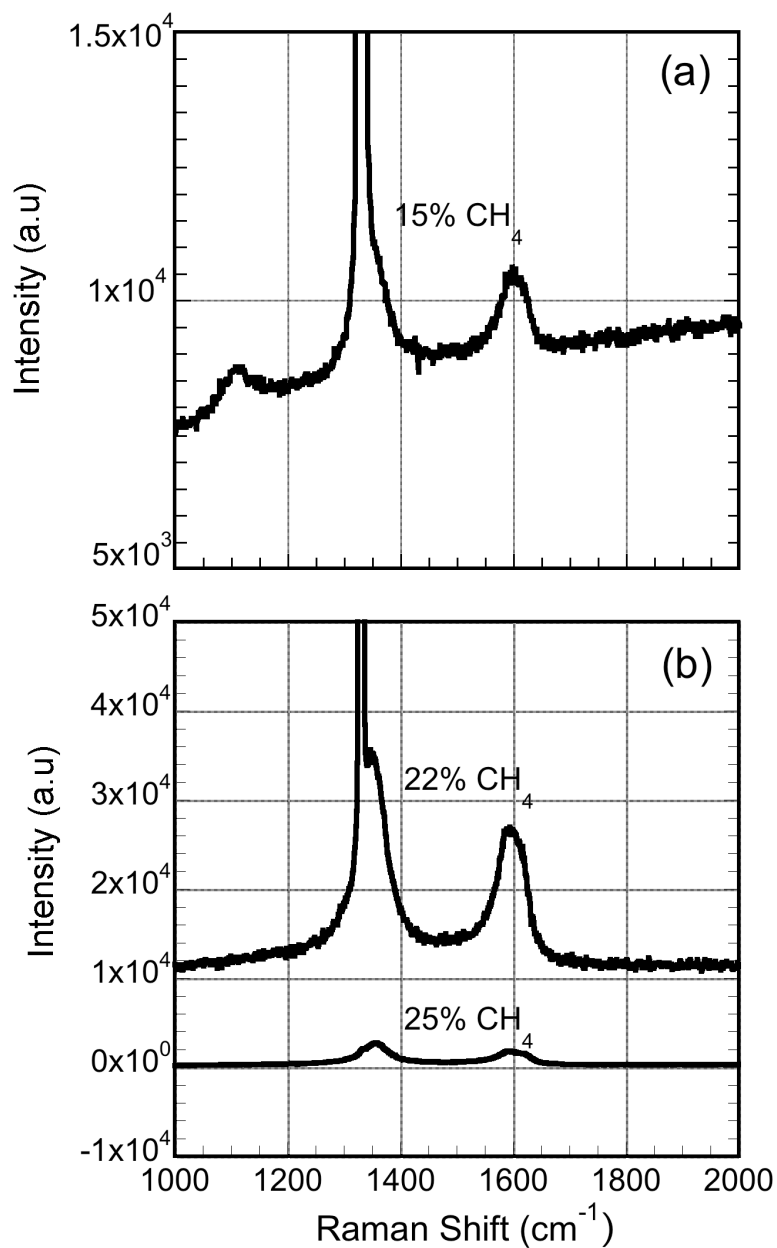encouraging as the interface between the CNT and the diamond is left free of metal.

Figure 8.7: Raman spectrum of as-grown samples (a) 15% CH$_4$ concentration (sample #1) (b) 22% and 25% CH$_4$ concentration (samples #2 and #4 respectively).
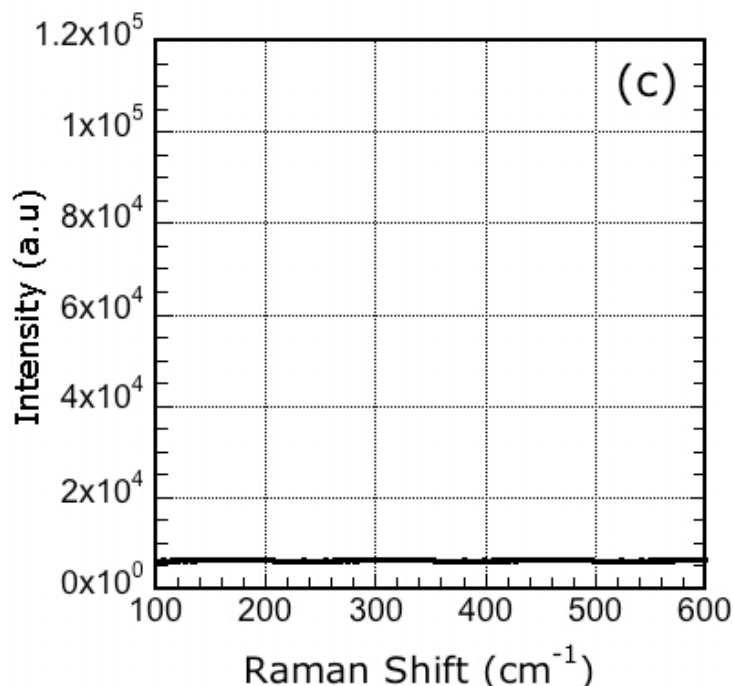
Figure 8.7 (c): Typical Raman spectrum between 100 and 600 cm^{-1} for as-grown CNT samples in this study.

The Raman spectra for samples #1, #2 and #4 are displayed in figures 8.7(a) - (c). Samples #1 and #2 (15% and 22% CH_4 respectively) display a strong peak at 1332 cm^{-1} corresponding to the characteristic Raman shift of the diamond substrate [19]. For the remaining spectra the D-band and G-band peaks as described previously are commonly attributed to presence of amorphous and graphitic carbons, respectively [20]. Also, radial breathing modes (RBM) are bond-stretching out-of-plane phonon modes for which all the carbon atoms move coherently in the radial direction, and whose frequency is between 100 and 500 cm^{-1} [21]. These modes are commonly used to identify the presence and diameter of SWCNTs [21]. Figure 8.7(c) displays this frequency range of the Raman spectrum taken from samples studied here, the fact that RBM features are absent from figure 8.7(c) indicates that these CNT structures are multi-walled CNTs (MWCNTs). In recent years it has become widely accepted that the crystallinity of CNTs can be measured from their peak intensity ratio, I_D/I_G [20]. Typically MWCNTs in their as-grown state are

more amorphous with an I_D/I_G ratio of 1 or greater than 1 being observed [21,22], whilst for as-grown SWCNTs a much lower ratio is usually seen [23]. Post synthesis annealing treatments can lead to very crystalline MWCNTs, with an I_D/I_G ratio as low as 0.22 being obtained [24]. In this study the I_D/I_G ratio is monitored as a function of the CH_4/H_2 gas ratio. Data analysis reveals a gradual reduction in the I_D/I_G ratio from 1.5(sample #4) to 1.3(sample #2) and finally to 1.05 +/- 0.05 (sample #1), indicating that the crystallinity in these MWCNTs increases as the CH_4/H_2 ratio reduces. An error bar for the determination of the I_D/I_G ratio for sample #1 is incorporated here due to a lack of data points for this peak, preventing a more precise mathematical model from being fitted. Trends similar to this have been reported in the literature with authors relating this to the preserving action carried out by H_2 on the catalyst particle surface, enhancing surface diffusion and promoting the development of more ordered and smooth graphene layers [24,25]. The Raman spectrum for sample #1 (figure 8.7(a)) exhibits a third peak at ~1120cm^{-1}. Peaks in the region from 1150cm^{-1} to 1170cm^{-1} have been routinely observed in nanocrystalline diamond films (NCD) [26,27] and have been linked to disordered sp^3 material by M.S. Kang *et al* [29]. In a study by Ferrari and Robertson [28] peaks near 1150 and at 1450cm^{-1} have been assigned to the transpolyacetylene situated at the grain boundaries of diamond nanocrystals. It is now widely accepted that these peaks are related to the presence of strained sp^3 bonds normally seen in poor quality NCD films. Why this absorption peak is only seen for sample #1 is not yet clear, however it may be related to the strained carbon bonds formed between the CNTs and the diamond substrate.

8.5 Conclusions

A synthesis program for the growth of MWCNTs on diamond has been developed. The influence of temperature and the methane/hydrogen ratio on growth has been established, and the tenacious nature of the CNTs bonded to the diamond substrate demonstrated. In this study substantial MWCNT

growth was observed when the methane/hydrogen ratio within a methane-hydrogen-nitrogen gas mixture was between 0.2 - 0.35, whilst the optimal growth temperature was ~700°C. Overall, the growth temperature combined with methane/hydrogen ratio determines the overall CNT yield whilst the crystallinity is seen to increase for a reducing methane concentration. The fact that strongly bonded CNTs can be successfully grown on single crystal diamond substrates is encouraging for future applications based-upon this interesting all carbon composite system.

8.6 References

1. LV Radushkevich, VM Lukyanovich. "O strukture ugleroda, obrazujucegosja pri termiceskom razlozenii okisi ugleroda na zeleznom kontakte". Zurn. Fisic. Chim. 26: 88–95 (1952)

2. S Iijima. Nature 354: 56-58 (1991).

3. M Meyyappan, Carbon Nanotubes: Science and applications".
    CRC Press, Boca Raton, FL, USA (2005).

4. MH Nazare, AJ Neves, , Editors. "Properties, Growth and
    Applications of Diamond". Institution of Engineering and Technology, UK (2001).

5. PW May. Phil. Trans. R. Soc. Lond. ; A358: 473-495 (2000).

6. TH Borst , O Weiss. Physica Status Solidi, A154: 423-444 (1996).

7. ML Terranova , V Sessa, M Rossi. Chem. Vap. Deposition, 12:315–325 (2006).

8. OV Yazyev , A Pasquarello. Phys. Rev. Letts, 100: 156102 (2008).

9. M Meyyappan, L Delzeit, A Cassell, D Hash. Plasma Sources Sci. Technol.; 12: 205– 216 (2003).

10. OA Nerushev , M Sveningsson, LKL Falk , F Rohmund. J. Mater. Chem, 11: 1122–1132 (2001).

11. AC Dupuis. Progress in Materials Science, 50: 929–961 (2005).

12. R T K Baker , M A Barber , P S Harris , F S Feates and R Waite.

J.Catalysis ; 26: 51-62 (1972).

13. RTK Baker , PS Harris , RB Thomas, RJ Waite. J. Catal, 30: 86-95 (1973).

14. JI Sohn, YW Ok, TY Seong , S. J Lee. Appl. Phys, 102: 014301 (2007).

15. D Takagi, Y Kobayashi, Y Homma. J. Am. Chem. Soc. 131: 6922–6923 (2009).

16. AJS Fernandes, M Pinto, MA Neto , FJ Oliveira, RF Silva , FM Costa. Diam. & Rela. Mater. 18: 160-163 (2009).

17. OA Shenderova, D. Areshkin, and DW Brenner, Vol. 29 (4), pp. 259–268 (2003).

18. B Baral, SSM Chan , RB Jackman. J. Vac. Sci. Technol. A14: 2303-2307 (1996).

19. DS Knight, WB White. J. Mater. Res. 4(2): 385-393 (1989).

20. M Endo, YA Kim, Y Fukai , T Hayashi, M Terrones, H Terrones,

21. M.S. Dresselhaus, G. Dresselhaus, R. Saito, A. Jorio, Physics Reports 409 47–99 (2005).

22. MS Dresselhaus. Appl. Phys. Lett, 79(10): 1534-1536 (2001).

23. JS Kim, KS Ahn, CO Kim, JP Hong. Appl. Phys. Lett, 82(10): 1607-1609 (2003).

24. Y Ando, X Zhaoi, S Inoue, T Suzuki, T Kadoya. Diamond & Related Materials, 14(3-7): 729 – 732 (2005).

25. YJ Yoon, JC Bae, HK Baik, SJ Cho, SJ Lee, KM Song, NS Myung. Chem. Phys. Lett. 366(1-2): 109-114 (2002).

26. GS Choi, YS Cho, SY Hong, JB Park, KH Son, DJ Kim. J. Appl. Phys. 91: 3847-3854 (2002).

27. K Okada, K Kanda, S Komatsu, S Matsumoto. J Appl. Phys, 88: 1674–1678 (2001).

28. AC Ferrari, J Robertson. Phys. Rev, B63: 121405–121408 (2001).

29. MS Kang, WS Lee, YJ Balk. Thin Solid Films, 398–399: 175–179 (2001).

Chapter 9: Conclusions

Important topics such as doping and the characterisation of nanometer thick diamond layers have been addressed in this thesis for the realization of high temperature bipolar devices and unipolar high power high frequency devices for room temperature operation. Also addressed in this thesis is the growth of carbon nanotubes on single crystal diamond. In the light of the results that have been obtained, important conclusions can be drawn regarding diamond growth and doping, and possible future work to advance the carbon nanotube-diamond structure towards possible applications.

Chapter 5

Due to the successful report of n-type doping of (111) diamond layers, a study investigating the carrier transport mechanisms in boron-doped (111) diamond layers was carried out. High quality homoepitaxial films have been grown on type 1b (111) single crystal diamonds. Tri-methyl boron (TMB) has been used to introduce boron as a substitutional dopant species during the homoepitaxial growth process, with free carrier (holes) concentrations as high as 2×10^{20} cm^{-3} whilst maintaining (valance) band conduction displaying mobilties of the order of 14 cm^2/Vs. These high values are thought to arise through delaying the onset of hopping conductivity within these films, due to the extremely low compensation levels observed for these films. Only at carrier concentrations measured as high as 9×10^{20} cm^{-3} does the mobility collapse to values of 1.5 cm^2/Vs. Interestingly, the mobility values in these films are not strongly degraded by increasing temperatures, with the maximum values of mobility in some films actually occurring at 700K. These results are very promising for the potential application of highly boron doped (111) homoepitaxial diamond layers for high temperature device applications. It is clear that the ultra-pure gases used for growth in the current instance and the growth parameters used can lead to very high quality doped diamond. The integration of these types of layers with more lightly phosphorus doped diamond (111) epitaxial layers can be seen to be an essential step towards the

realization of bipolar devices from diamond for high temperature device applications.

Chapters 6 and 7

Another problem that exists within the diamond technology sphere is the lack of shallow dopants, ruling out electronic device operation at room temperatures. The discovery of diamond p-type surface conductivity led to great deal of excitement due to its activation at room temperature. Further studies by many scientists worldwide revealed the limitations of this technology, i.e. conductivity of the diamond surface is highly sensitive to temperature and atmospheric conditions, and subsequently interest in this technology has greatly diminished for electronic applications. Another method in which diamond can be utilised for room temperature device operation is by attempting to grow boron δ-doped diamond layers. A comprehensive Hall effect and impedance spectroscopy study on this topic has been performed in this thesis. Impedance spectroscopy has clearly shown itself to be a powerful, non-destructive, method for investigating the electrical properties of complex doped diamond structures. In the case of the δ-doped samples studied here, multiple conduction paths have been identified, which can be attributed to conduction within the heavily boron doped δ-layer and the (nominally) intrinsic regions adjacent to the δ-layer. Samples with an intrinsic capping layer have been shown to support three parallel conduction paths, assigned to the δ-layer, and to two differing layers or interfaces between the δ-layer and the underlying buffer and overlying cap. It has been shown that in some δ-doped structures, that boron acceptor states may exist in the interfaces between the intrinsic material and the δ-layer.

Carrier mobilities reported for high quality δ-doped layers within III-V semiconducting technologies range from 10^3-10^4 cm^2/Vs [reference 7, chapter 7]. El-Hajj and co-workers (reference 8, chapter 7) reported (in 2008) Hall mobilities of boron δ-doped diamond layers between 20 and 30cm^2/Vs. In

this study mobility values are recorded between 1 and 5 cm^2/Vs. The fact that carrier mobilities seen here are comparable to those routinely observed in heavily boron-doped diamond films implies that a limited δ-doping effect is present in these structures, and more so that carrier transport is still mainly confined to the δ-layer itself.

In summary, introduction of a capping layer creates a conduction path that is assigned to a boron interfacial region between the δ-layer and the cap. Carrier mobilities measured here are much lower than those recorded within III-V δ-doping technologies.

Further work is currently under way to improve the quality of the interfacial regions in this structure. Treatments such as annealing samples in hydrogen and methane are to be investigated as are high pressure high temperature treatments. A graded boron-doped δ-layer has also been proposed as viable method for the reduction of interfacial crystal disorder.

Chapter 8

Since the discovery of carbon nanotubes (CNTs) many extensive studies have been performed detailing their excellent physical and mechanical properties. CNTs have been deposited on many materials since their initial discovery, in this thesis the deposition of carbon nanotubes on diamond using the glow-discharge technique is studied using a combination of scanning electron microscopy and Raman spectroscopy for the first time. A synthesis program for the growth of MWCNTs on diamond has been developed. The influence of temperature and the methane/hydrogen ratio on growth has been established, and the tenacious nature of the CNTs bonded to the diamond substrate demonstrated. In this study substantial MWCNT growth was observed when the methane/hydrogen ratio within a methane-hydrogen-nitrogen gas mixture was between 0.2 - 0.35, whilst the optimal growth temperature was ~700°C. Overall, the growth temperature combined with

methane/hydrogen ratio determines the overall CNT yield whilst the crystallinity is seen to increase for a reducing methane concentration. The fact that strongly bonded CNTs can be successfully grown on single crystal diamond substrates is encouraging for future applications based-upon this interesting all carbon composite system. If future applications for this all-carbon system are to be found the crystallinity of these as-grown CNTs will have to be greatly improved. Considering the huge amount of research already performed in this field this target is certainly realistic. It is hoped that future work here will lead to the development of a high temperature diode from this all carbon system by depositing CNTs on boron-doped diamond substrates.

CVD diamond as a potential electronic material still has many challenges to overcome before diamond electronics can become a reality. It should be noted that all wide bandgap materials have problems with doping and growth. Diamond has greater potential for applications in such areas as UV detection, high temperature/harsh environments, optics and thermal management.

Relevant Publications

1. H. Ye., N. Tumilty., D. Garner., R.B. Jackman., (2007). Device Simulation and Design Optimization for Diamond Based Insulated-gate Bipolar Transistors. *Proceedings of the Materials Research Society (Diamond Electronics: Fundamentals to Applications)* Bergonzo P; Gat R; Jackman RB; Nebel CE (ed.) Pittsburgh, USA:MRS, 956, 275-280.

2. H. Ye, N. Tumilty, M. Bevilacqua, S. Curat, M. Nesladek, B. Bazin, P. Bergonzo, and R. B. Jackman, Electronic properties of homoepitaxial (111) highly boron-doped diamond films, J. Appl. Phys. 103, 054503 (2008).

3. N. Tumilty, J. Welch, H Ye, R S. Balmer, C Wort, R Lang, and R B. Jackman, Multiple conduction paths in boron delta-doped diamond structures, Appl. Phys. Lett. 94, 052107 (2009).

4. N. Tumilty, J. Welch, R. Lang, C. Wort, R. Balmer, and R B. Jackman, An impedance spectroscopic investigation of the electrical properties of delta-doped diamond structures, J. Appl. Phys. 106, 103707 (2009).

5. N. Tumilty et al. Synthesis of carbon nanotubes on single crystal diamond. Carbon (2010), doi:10.1016/ j.carbon.2010.04.023.